Title
Laser absorption spectroscopy techniques for determining gas properties in high pressure rocket combustors

Author
Lee, Daniel D

Publication Date
2020

Peer reviewed|Thesis/dissertation

UNIVERSITY OF CALIFORNIA
Los Angeles

Laser absorption spectroscopy techniques for determining gas properties in high pressure rocket combustors

A dissertation submitted in partial satisfaction
of the requirements for the degree
Doctor of Philosophy in Department of Mechanical and Aeorspace Engineering

by

Daniel D. Lee

2020

ABSTRACT OF THE DISSERTATION

Laser absorption spectroscopy techniques for determining gas properties in high pressure rocket combustors

by

Daniel D. Lee
Doctor of Philosophy in Department of Mechanical and Aeorspace Engineering
University of California, Los Angeles, 2020
Professor Raymond M. Spearrin, Chair

This dissertation describes laser absorption spectroscopy methods developed for temperature and carbon oxide (CO and CO_2) sensing in high-pressure, fuel-rich combustion conditions of hydrocarbon-fueled bipropellant rockets. The scope of the work includes fundamental studies of spectroscopic interactions at high gas density, development of unique laser tuning and signal processing methods, and application of prototype sensors to rocket combustion devices under investigation at the Air Force Research Laboratory in Edwards, CA. Infrared vibrational spectra of CO and CO_2 were probed using tunable semi-conductor lasers to infer gas properties. Initial sensor design targeted the absorption spectra of CO near 4.98 μm, selected to minimize spectral interference with other combustion gas species at the extreme temperatures (> 3000 K) and pressures (> 50 atm) of a kerosene-fueled rocket combustion environment. Successful measurements were conducted up to 70 bar utilizing a scanned wavelength modulation spectroscopy technique, creating a new pressure-limit for quantitative in situ species sensing in a combustion device. At higher pressures (which were tested), collisional-broadening effects blended the targeted absorption transitions, causing differential absorption to diminish and reducing the signal-to-noise ratio of the measurements.

To overcome the pressure-constraints, a more advanced laser absorption sensing strategy was developed, targeting the vibrational bandheads of CO near 2.3 μm and CO_2 near 4.2 μm and exploiting the band narrowing effects of collisional line mixing to counter collisional broadening. Spectral line mixing—typically observed at high gas densities in which intermolecular collisions are sufficiently frequent and strong to cause a shift in energy level populations—corresponds to a transfer of absorption intensity from weak to strong absorption regions, inducing a narrowing of spectral features. This non-ideal phenomenon is more prominent in spectrally dense regions, such as bandheads. Targeting infrared bandheads to exploit line mixing, measurements of CO and CO_2 concentration were demonstrated over a range of high pressures up to 105 bar in a single-element-injector RP-2/CH_4-GOx rocket combustor. To make such measurements quantitative, spectroscopic models accounting line mixing effects have been developed utilizing a high-enthalpy shock tube; these models are then employed for interpretation of measured absorption signals for quantitative temperature and species sensing.

The dissertation of Daniel D. Lee is approved.

Ann Karagozian

Artur Davoyan

Richard Wirz

Stephen Schumaker

Raymond M. Spearrin, Committee Chair

University of California, Los Angeles

2020

Contents

List of Figures

Acknowledgments

My work presented here would not have been possible without the great support and guidance from the many individuals I interacted with during my PhD. First of all, I owe my deepest gratitude to my PhD advisor, Professor Mitchell Spearrin, for bringing me into the lab and mentoring me throughout my studies. It was definitely one of my biggest fortunes to be his student and learn and develop under his mentorship. He taught me how to be a passionate and ambitious researcher and provided me ample opportunities to grow as a researcher who understands both the fundamental and applied aspects of science. I would also like to thank Professor Ann Karagozian, Dr. Stepehn Schumaker, Professor Artur Davoyan, and Professor Richard Wirz for their time and effort serving on my committee during such a difficult time.

Next, I would like to thank the many individuals from Air Force Research Laboratory (AFRL) in Edwards, CA. Especially my three mentors, Dr. Stephen Schumaker, who not only served on my committee but also provided me an opportunity to conduct research at the outstanding rocket facility at AFRL, Dr. Stephen Danczyk, who runs the rocket test facility and assisted me in succesfully running multiple test campaigns over several years, and Dr. William Hargus Jr., who provided me mentorship and the opportunity to work on fascinating projects with other talented researchers, including his rotating detonation rocket engine team during the last year of my PhD.

These acknowledgments would not be complete without mentioning my peers and mentors in the Laser Spectroscopy and Gas Dynamics Laboratory at UCLA. I share a lot of precious memories with this incredible group: struggling together through seemingly unsolvable problems, having many group gatherings to celebrate each other's achievements, and spending time together to not only work on

various projects but share personal life. A special thanks goes to Fabio Bendana for being a great partner throughout my PhD with persistent support in conducting research and publishing articles and Anil Nair for his excellent assistance throughout several measurement campaigns at AFRL. I also would like to thank the many other friends outside of UCLA and AFRL who have been a constant source of support and encouragement. Some special individuals include Brian Kim, Hyesoo Lee, Mier Lee, Julia Na, Christopher Choi, Irene Han, and, Eunice Kang. These beloved friends have definitely made my life more enjoyable and endurable during my PhD.

Last and foremost, I am indebted to my family for their support and confidence in me. My father has always supported me unwaveringly and tried to provide me his best, whether I did well or not. My mother filled me with confidence through countless words of encouragement and taught me the value of patience and persistence, which enabled me to finish my PhD. I would also like to thank my brother for being a good-hearted and admirable brother. I am deeply appreciative of my family for everything they have done for me.

Curriculum Vitae

2011 – 2013	B.S. in Mechanical Engineering, University of California, Los Angeles (UCLA).
2015 – 2017	M.S. in Mechanical Engineering, University of California, Los Angeles (UCLA).
2015 – Present	Ph.D. student in Mechanical Engineering, University of California, Los Angeles (UCLA).

Publications

[1] **D. D. Lee**, F. A. Bendana, A. P. Nair, S. A. Danczyk, W. A. Hargus Jr., and R. M. Spearrin, "Exploiting line-mixing effects for laser absorption spectroscopy at extreme combustion pressures," *Proceedings of the Combustion Institute*, (In press, 09/2020).

[2] A. P. Nair, **D. D. Lee**, D. I. Pineda, J. Kriesel, W. A. Hargus Jr., J. W. Bennewitz, S. A. Danczyk, R. M. Spearrin, "MHz laser absorption spectroscopy via diplexed RF modulation for pressure, temperature, and species in rotating detonation rocket flows," *Applied Physics B*, vol. 126, p. 138, 8 2020

[3] **D. D. Lee**, F. A. Bendana, A. P. Nair, D. I. Pineda, and R. M. Spearrin, "Line mixing and broadening of carbon dioxide by argon in the $\nu 3$ bandhead near 4.2 μm at high temperatures and high pressures," *Journal of Quantitative Spectroscopy and Radiative Transfer*, p. 107135, 6 2020.

[4] F. A. Bendana, **D. D. Lee**, C. Wei, D. I. Pineda, and R. M. Spearrin, "Line mixing and broadening in the $\nu(1\rightarrow3)$ first overtone bandhead of carbon monoxide

at high temperatures and high pressures," *Journal of Quantitative Spectroscopy and Radiative Transfer*, vol. 239, p. 106636, 12 2019.

[5] F. A. Bendana, **D. D. Lee**, S. A. Schumaker, S. A. Danczyk, and R. M. Spearrin, "Cross-band infrared laser absorption of carbon monoxide for thermometry and species sensing in high-pressure rocket flows," *Applied Physics B*, vol. 125, p. 204, 11 2019.

[6] Y. J. Lin, S. Cakmakyapan, N. Wang, **D. D. Lee**, R. M. Spearrin, and M. Jarrahi,"Plasmonic heterodyne spectrometry for resolving the spectral signatures ofammonia over a 1-45 THz frequency range," *Optics Express*, vol. 27, p. 36838,12 2019.

[7] **D. D. Lee**, F. A. Bendana, S. A. Schumaker, and R. M. Spearrin, "Wavelength modulation spectroscopy near 5 μm for carbon monoxide sensing in a high-pressure kerosene-fueled liquid rocket combustor," *Applied Physics B: Lasers and Optics*, vol. 124, p. 77, 5 2018.

[8] A. P. Nair, **D. D. Lee**, D. I. Pineda, J. Kriesel, W. A. Hargus Jr., J. W. Bennewitz, S. A. Danczyk, R. M. Spearrin, "MHz mid-infrared laser absorption of CO and CO2 for pressure, temperature, and species in rotating detonation rocket flows," in AIAA Propulsion and Energy 2020 Forum, no. January, (Virtual), American Institute of Aeronautics and Astronautics, 8 2020.

[9] **D. D. Lee**, F. A. Bendana, A. P. Nair, R. M. Spearrin, S. A. Danczyk, and W. A. Hargus Jr., "Laser absorption of carbon dioxide at the vibrational bandhead near 4.2 μm in high-pressure rocket combustion environments," in AIAA Scitech 2020 Forum, no. August, (Orlando, Florida), American Institute of Aeronautics and Astronautics, 1 2020.

[10] **D. D. Lee**, F. A. Bendana, and R. M. Spearrin, "Exploiting line mixing effects for laser absorption spectroscopy at extreme combustion conditions," in 11th U.S. National Combustion Meeting, (Pasadena, California), The Combustion Institute, 2019

[11] F. A. Bendana, **D. D. Lee**, R. M. Spearrin, S. A. Schumaker, and S. A. Danczyk, "Infrared laser absorption thermometry and CO sensing in high-pressure rocket combustion flows from 25 to 105 bar," in AIAA Scitech 2019 Forum, no. January, (San Diego, California), pp. 1–8, American Institute of Aeronautics and Astronautics, 1 2019.

[12] **D. D. Lee**, F. A. Bendana, and R. M. Spearrin, "Laser Absorption Spectroscopy of Carbon Monoxide near 4.97 μm for Temperature and Species Measurements in Hydrocarbon-Fueled Rockets," in 2018 AIAA Aerospace Sciences Meeting, (Kissimmee, Florida), American Institute of Aeronautics and Astronautics, 2018.

CHAPTER 1

Introduction

Many optical diagnostic techniques have been developed to measure gas properties in combustion devices, owing to their non-intrusive and in situ capability as well as the potential for targeting many thermophysical flow-field scalars that can be related to light interactions. Among these techniques, laser absorption spectroscopy (LAS) has proven highly quantitative and relatively robust in harsh environments for the measurement of temperature and species concentrations, attained by targeting individual spectral transitions (*lines*) which can be resolved with tunable narrow-band light sources and interpreted with a few spectroscopic parameters. LAS has demonstrated ample success for measuring gas properties in many practical combustion devices, but few attempts on high-pressure devices have been demonstrated due to intrinsic limitations at high gas densities. The highest pressure condition studied in practical combustion devices utilizing LAS, prior to this work, is approximately 55 bar [1, 2]. At elevated pressures, LAS falters largely due to collisional broadening which blends and convolutes spectral lines and scales linearly with pressure. The aim of this work is to advance the pressure capability of infrared laser absorption spectroscopy for sensing in harsh high-pressure and high-temperature environments, with specific application to rocket combustion devices. In this dissertation, the design, development, and demonstration of novel temperature and carbon oxide (CO and CO_2) sensors are presented in each chapter, which roughly follows the chronological order in which the research was conducted. In this introductory chapter, specific motivation for high-pressure combustion diagnostics is first discussed, followed by a review of

various optical diagnostic techniques to provide context for the novelty of this work. Previous studies regarding the implementation of these techniques in high pressure combustion devices are also reviewed to give the reader a sense of the state-of-the-art. The introduction closes with an overview of the dissertation chapters that follow.

1.1 Motivation for high pressure diagnostics

According to both the Department of Defense (DOD) and Department of Energy (DOE), combustion at high pressures is a strong research priority, since increasing the pressure of all thermodynamic cycles—including rocket combustion—also increases power density and fuel efficiency [3, 4]. The positive correlations for various ideal thermodynamic cycles are illustrated in Fig. 1.1. Thermodynamically,

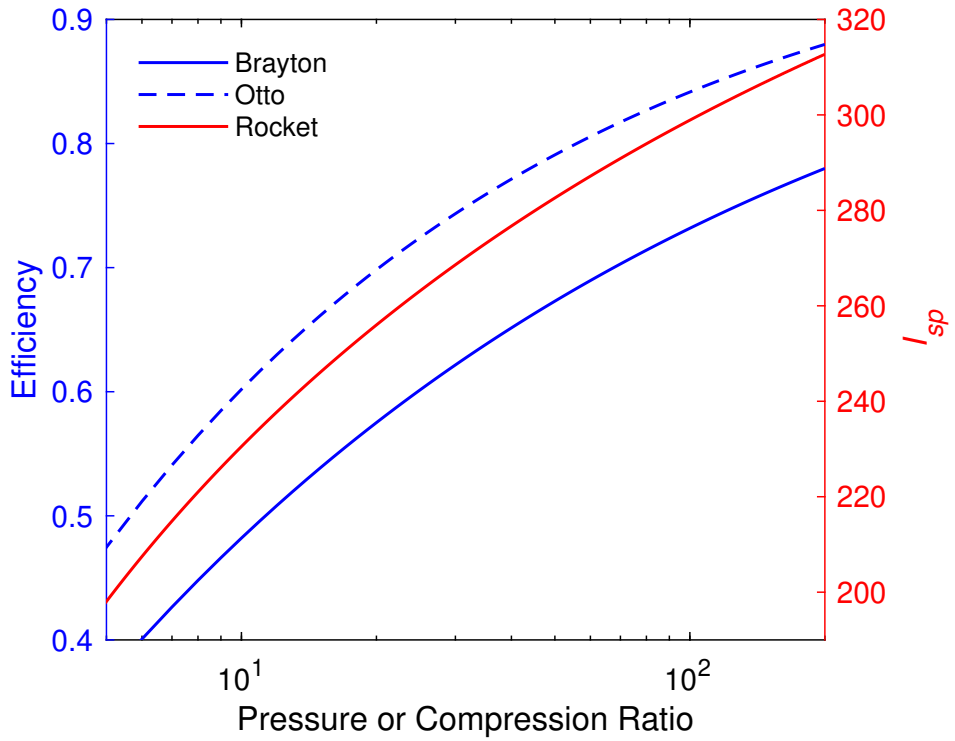

Figure 1.1: Simulated I_{sp} and thermal efficiencies as a function of pressure/compression ratio

higher pressure or compression ratio increases cycle efficiency. Consequently, there has been a persistent effort to increase the operating pressure of various energy and propulsion devices, including internal combustion (IC) engines, gas turbines, and rocket engines. More background on these efforts are presented in the following subsections.

1.1.1 Internal Combustion (IC) Engines

Internal combustion (IC) engines, or reciprocating/piston-cylinder engines, are the most common form of heat engine used for portable power solutions such as transportation. The baseline engine types include the port injection spark ignition engine (PISI), the direct injection spark ignition engine (DISI), and the direct injection compression ignition engine (DICI) [5]. These varying types of IC engines are utilized for a range of purposes including automobile and air transportation and localized power generation (back-up generators). Typical maximum cylinder pressure can reach between 50 bar and 180 bar depending on the engine type.

Increase in energy consumption due to the growth of human population, increased transportation use, and higher standard of living has lead to undesirable outcomes, such as depletion of fossil fuel resources, rising fuel prices, and air pollution [6]. Accordingly, there has been a strong desire to increase the fuel efficiency of IC engines while maintaining nitrogen oxides (NO_x) and particulate matter (PM) emissions below the current stringent emission mandates [6]. IC engines most commonly operate on Otto cycle or Diesel cycle and one of the known methods to improve efficiency is to operate at higher compression ratios as shown in Fig. 1.1. A promising advanced combustion strategy is homogeneous charge compression ignition (HCCI), a hybrid combustion concept which combines elements of both conventional spark ignition engines and compression ignition engines. HCCI operation achieves very high peak pressures in a nearly constant volume combustion process over relatively short combustion durations (~ms), resulting in higher

thermal efficiency [7]. Typical peak pressure for HCCI operation is more than 70 bar and often exceeds 100 bar [8, 9]. In addition to HCCI, some ultra-clean piston-engine concepts have been developed to operate at peak pressures in excess of 100 bar [10]. Other research suggests increasing compression ratios higher than 100:1 using a free-piston device [11] may offer enhanced performance. A common theme of advanced IC engine research is high-pressure operation.

1.1.2 Gas Turbines

Gas turbines are the most widely used means to generate mechanical power and electricity at a large scale. Some of the applications of gas turbines include power plants and jet engines. These gas turbines typically operate on Brayton cycle, where compressed air and injected fuel goes through constant-pressure combustion process inside the chamber to produce the heated combustion products that

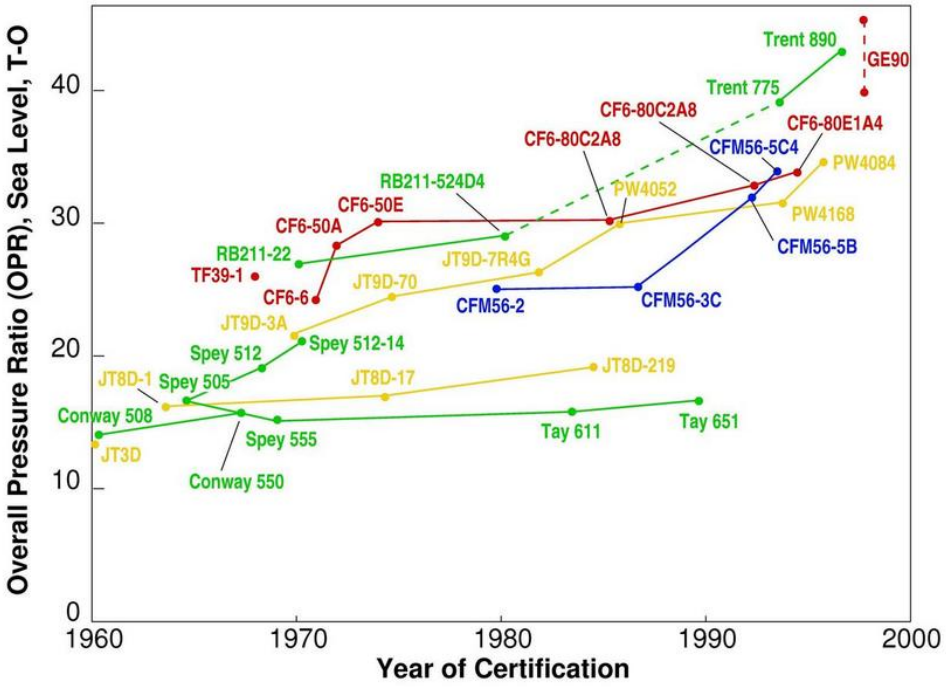

Figure 1.2: Gas turbine engine pressure ratio trends [12].

expands through a gas turbine to produce work. Increasing pressure ratio improves gas turbine performance as shown in Fig. 1.1 and thus, there have been continuous efforts to develop gas turbines capable of operating at higher pressure ratios [13]. Fig. 1.2 illustrates this trend of increasing pressure ratio of various engines developed over the past 50 years. It can be noted that over the past several decades, the pressure ratios of jet engines increased significantly, from around 15 in 1960 to over 40 in the modern era. Parallel efforts in power generation include development of combined cycle gas turbines (CCGT), consisting of a Brayton cycle-based topping cycle and Rankine cycle-based bottoming cycle. There has been similar active research and development to increase compression ratio of the gas turbine as one of the means to improve thermal efficiency [14].

1.1.3 Rockets

Representative performance metrics of various commercial rocket engines are summarized in Table 1.1. These rocket engines were developed for different purposes, resulting distinct characteristic data. For example, the LE-7A and Vulcain 2, demonstrating comparable thrust levels and operating times, are used as core engines in launchers with two large thrust boosters each (the HII and the ARIANE 5, respectively), while the RD-108, Viking 5C, and YF-20B—engines with similar parameters—are all applied as clusters of engines in the first stage of launchers without large boosters [15]. Regardless of the design purpose, we can generally observe increase in performance (specific impulse) with higher operating pressure, though this is also strongly propellant-dependent. One of the higher performing flight engines, the RD-180 engine, designed and developed in Russia, operates at a steady chamber pressure of 257 bar. Current rocket engine research and development is aimed at operating at even higher pressures. The Raptor Engine by Space Exploration Technologies (SpaceX), for example, recently broke the record for highest rocket combustion chamber pressure, reaching approximately 330 bar.

Table 1.1: Characteristic data of core and main stage engines [15]

Rocket Engine	Engine Cycle	Propellant Combination	Thrust [MN]	Specific Impulse [s]	Burn Time [s]	Chamber Pressure [bar]
RD-108	SC	LOX/Kerosene	0.78	252	290	51
Viking 5C	GG	N_2O_4/UH25	0.68	249	142	59
YF-20B	GG	N_2O_4/UDMH	0.73	259	170	74
RS-68	GG	LOX/Hydrogen	2.89	360	249	97
Merlin	GG	LOX/RP-1	0.84	282	345	97
Vulcain 2	GG	LOX/Hydrogen	0.94	320	600	116
LE-7A	SC	LOX/Hydrogen	0.84	338	390	121
BE-4	ORSC	LOX/Methane	2.4	310		135
SSME	SC	LOX/Hydrogen	1.82	364	480	205
RS-25	SC	LOX/Hydrogen	1.86	366	510	206
RD-0120	SC	LOX/Hydrogen	1.51	359	600	218
RD-180	SC	LOX/RP-1	3.83	311	270	257
Raptor	FFSC	LOX/Methane	2.0	330		330

GG: Gas generator cycle, ORSC: Oxygen-rich staged combustion cycle
SC: Stage combustion cycle, FFSC: Full-flow stage combustion cycle

Unfortunately, despite many advanced combustion devices aimed at operating above 50 bar, a gap in optical diagnostic capability persists at these extreme conditions, indicative of the acute need to develop new diagnostic capability to characterize combustion at extreme pressures. Most state-of-the-art combustion diagnostics have been limited to near-atmospheric conditions, with pressure capability rarely exceeding 10 atm. There have been few but some notable successes in measurements of gas properties in high pressure devices, which are reviewed later in this section. Most closely related to the topic of this dissertation, laser absorption spectroscopy has shown promising measurement capability up to approximately 55 bar, probing H_2O and CO, but existing capability at these pressures is still insufficient to fulfill the aforementioned diagnostic needs [1, 2]. This dissertation focuses on the research underlying the development of temperature and carbon oxide (CO_2 and CO) sensing strategies based on infrared laser absorption that can provide a granular method to assess combustion performance

of rocket propulsion devices at extreme pressures.

1.2 Optical diagnostic techniques for combustion devices

Optical measurement techniques are favored over traditional measurement methods (i.e. thermocouples, gas chromatography) for studying flow properties of combustion devices, due to non-intrusiveness which enables survival in harsh environments and does not disrupt the flow-field. The various optical techniques exploit different types of light-matter interactions such as emission, scattering, and absorption for measurement of gas properties in a flow-field of interest. In this section, brief reviews on various optical diagnostic techniques are given, along with previous efforts to apply these techniques in practical combustion devices operating at elevated pressure (>10 bar).

1.2.1 Laser-Induced Fluorescence

Laser-induced fluorescence (LIF) is an optical diagnostic technique that measures spontaneous emission of atoms or molecules to infer thermophysical properties. These properties include temperature, species concentration, velocity, pressure, and number density. LIF has the capability to measure a wide range of species, including radicals or atoms (O, H, C...), stable diatomics (O_2, CO, NO...), and polyatomics (CO_2, NO_2, toluene (C_7H_8)...) [16] The spatial resolution capability of LIF (imaging the emission induced by a laser beam or sheet) is the key feature of the method.

Laser-induced fluorescence includes two steps: (1) absorption of the laser photon, followed by (2) spontaneous emission. Generally, either continuous wave (CW) or pulsed lasers are used to excite an atom or a molecule, and photomultiplier tubes (PMTs) or photodetectors are used to capture spontaneous emission that occurs after some delay. This can be easily extended to two dimensions by expanding

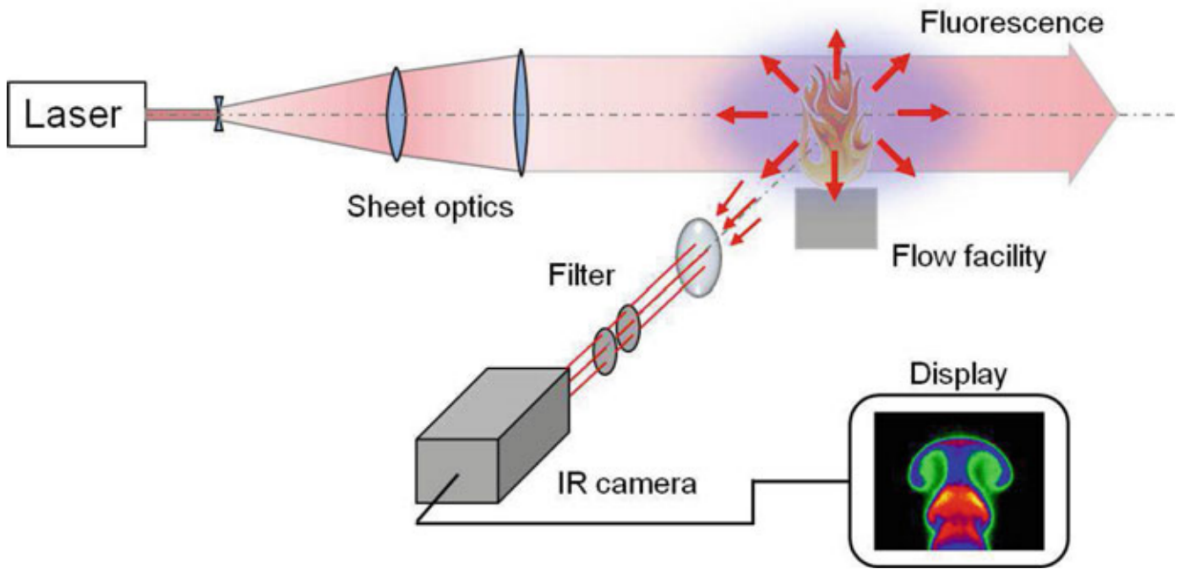

Figure 1.3: Typical experimental setup for PLIF [16].

the laser beam into a sheet of light and replacing the detector with a 2-D detector array (i.e., a digital camera) [17]. The technique utilizing this advantage is known as Planar Laser-Induced Fluorescence (PLIF). The laser beam passes through a system of optics to form a laser sheet, which passes through the flow-field of interest. Part of the light is absorbed and some fraction of the absorbed light is re-emitted as fluorescence. A portion of the fluorescence is captured by a 2-D detector array such as digital camera, placed perpendicular to the laser sheet, as shown in Fig. 1.3. This setup requires an accurate alignment and precise coupling to maximize the optical collection efficiency. In addition, calibration is required for each specific setup to quantitatively interpret the measurement. Despite quantitative measurement complexity, PLIF has been extensively utilized to visual combustion flow fields.

Planar Laser-Induced Fluorescence (PLIF) was first employed to study combustion in 1982 [18, 19] and has been continuously advanced since then. However, most studies have been conducted at lower pressures (<10 bar) and in a controlled laboratory setups due to challenges associated with higher pressures. Namely,

as pressure increases, quenching processes (which scale with pressure) become dominant, leading to low fluorescence yields. This intrinsic element (quenching) of PLIF limits quantitative and accurate optical measurements at high pressure. Consequently, there have been few successful measurements conducted in practical combustion devices operating at pressures above 10 bar. Notably, Schultz et al measured formation of nitric oxide in a transparent spark-ignition (SI) engine at pressure up to 18 bar [20]. Einecke et al measured absolute concentration, temperature, and fuel/air equivalence ratios inside the SI engine at pressure up to 22 bar [21]. Rothamer et al optimized tracer-based planar laser-induced fluorescence (TB-PLIF) imaging diagnostic using 3-pentanone in IC engine up to 15 bar [22].

1.2.2 Coherent Anti-Stokes Raman Spectroscopy (CARS)

Raman scattering is the inelastic scattering of light induced from the interaction between a molecule and a photon. When the molecule gains energy from the photon, the scattered photon loses energy that leads to a increase in its wavelength and this is known as Stokes Raman scattering. By contrast, when the molecule loses energy, the scattered photon gains energy that leads to a decrease in its wavelength, which is called Anti-Stokes Raman scattering. The cross-section for Raman scattering is several orders of magnitude smaller than other optical diagnostic techniques such as absorption and LIF, requiring high power laser light sources (i.e. Nd:YAG lasers) [16].

Coherent Anti-Stokes Raman Spectroscopy (CARS) technique measures Anti-Stokes Raman spectra, utilizing a non-linear four wave parametric process. Two waves at the pump frequency (ν_1) and one wave at the Stokes frequency (ν_2) are focused to a flow-field of interest to produce a new coherent beam at the anti-Stokes frequency ($\nu_4 = 2\nu_1 - \nu_2$) [23]. The general setup comprises multiple laser sources to generate the pump and the Stokes beams, as well as an intricate system of

optics and detection systems, as shown in Fig. 1.4. Similar to PLIF, the measured signal depends on optical collection efficiency, and thus requires a sophisticated alignment and an accurate calibration for quantitative measurement. These factors can make CARS a complex and expensive experiment; however, the high temporal and spatial resolution attained from the technique has positioned CARS as an attractive diagnostic tool in studying combustion [16]. CARS has commonly been used to measure temperature and species in a flow field of interest. Unlike some other optical diagnostic techniques, CARS can measure species without an intrinsic dipole moment, such as IR-inactive molecules (i.e. N_2, H_2, O_2) [16].

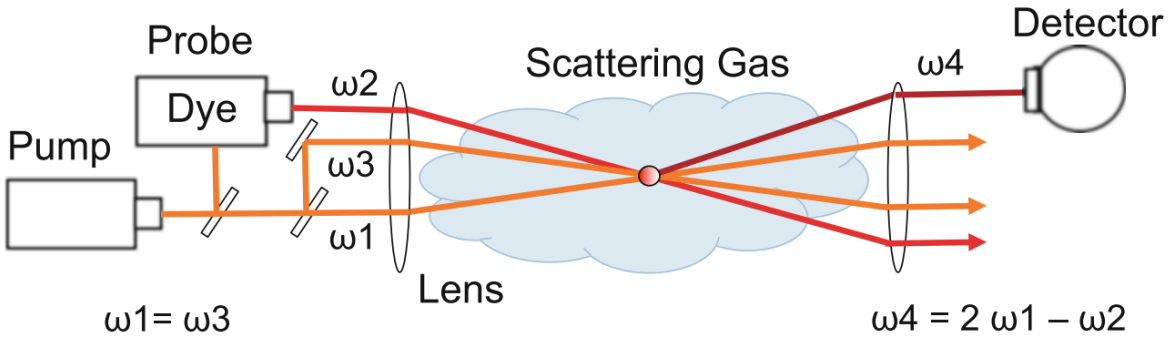

Figure 1.4: Schematic of CARS experiment (4-wave mixing) [16].

Over the past decades, some CARS techniques have been used to study gas properties in practical combustion devices operating at pressure above 10 bar. The first implementation of CARS in an internal combustion (IC) engine, with operating pressures up to 20 bar, was accomplished by Stenhouse et al [24]. Since then, CARS has been developed and employed in other combustion devices operating at even higher pressures. Smith et al conducted CARS measurements targeting hydrogen on a LOX/hydrogen rocket combustor up to 60 bar [25]. The following year, Grisch et al made measurements on a LOX/hydrogen rocket combustor at slightly higher pressures, reaching 65 bar [23], and shortly thereafter, on a LOX/CH_4 rocket combustor up to 56 bar [26]. CARS was also used to measure temperature and species inside a gas turbine combustor facility, operating around

10 bar, by Thariyan et al [27].

1.2.3 Laser Absorption Spectroscopy

Laser absorption spectroscopy (LAS) is an optical diagnostic technique that exploits absorption of the light—resonant to difference in energy levels of a molecule—to infer thermo-physical properties, including temperature, pressure, species, and velocity. Each molecule present in a flow field contains a discrete set of quantum energy levels, which leads to a unique absorbance spectrum. The infrared offers access to fundamental vibrational bands of most combustion species. By probing ro-vibrational transitions in the infrared, LAS has the capability to measure hydrocarbon fuels (CH_4), intermediates (CO), and combustion products (CO_2, H_2O). Atoms or molecules without an intrinsic dipole moment associated with vibration (N_2, O_2) are not accessible in the infrared, but may be probed in the UV.

Similar to other optical diagnostic techniques, the experimental setup for LAS consists of laser sources, alignment optics, and detectors as shown in Fig. 1.5; however, due to high optical cross-sections, lower power sources can be used, often reducing cost. LAS can also be a calibration-free method due to the ratio-metric nature of the measurement, and thus doesn't require any additional calibration measurements, which simplifies the measurement procedure and data processing. As mentioned, due to stronger optical cross-section of absorption interactions, low power semi conductor lasers (i.e. diode lasers, interband cascade lasers (ICL) quantum cascade lasers (QCL)) are sufficient for sensitive absorption measure-

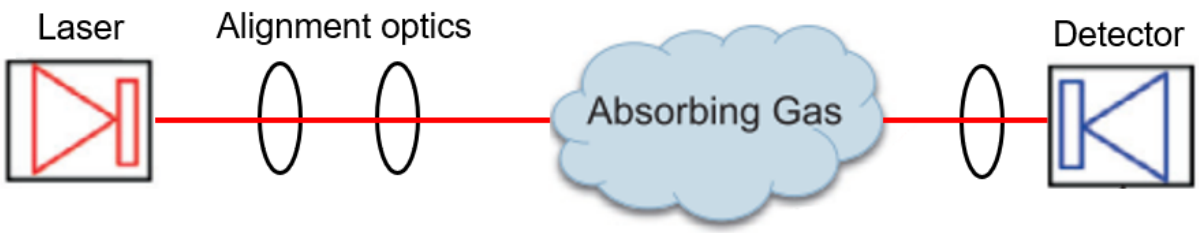

Figure 1.5: Schematic of LAS experiment.

ments. Recent advances in mid-infrared photonics have increased wavelength access in this domain and reduced the size and cost of these lasers to be more compact and portable. Other mid-IR optical components (i.e. fibers, lens, filters) have advanced as well, easing the deployment of complete sensor systems to practical combustion devices.

Laser absorption spectroscpy (LAS) has been used more extensively on practical combustion devices operating at elevated pressure (>10 bar) compared to other optical diagnostic techniques, and has shown capability for quantitative sensing. One of the earlier works by Schlosser et al [28] includes an experiment on a pulverized-coal-fired (PCF) plant, operating at 16 bar. Sun et al and Sur et al performed near-infrared absorption measurements of CO, CO_2, and H_2O in an entrained flow coal gasifier, which operated around 18 bar [29, 30]. There have been several works documenting near-infrared water vapor detection by Reieker et al, Witzel et al, and Burkle et al in an internal combustion (IC) engine, with pressures ranging from 13 to 20 bar [31, 32, 33]. Near-infrared water vapor measurement has been conducted in a homogeneous-charge-compression-ignition (HCCI) engine by Kranendonk et al and Mattison et al [34, 2]. A pulse detonation engine (PDE) has also been studied through LAS by Sanders et al, Mattison et al, Spearrin et al, and Goldenstein et al [35, 36, 37, 1]. Out of all the studies listed above, the measurements conducted in a PDE presented in the work by Goldenstein et al [1] and in an HCCI engine demonstrated in the work by Mattison et al [2] were done at the highest operating pressures of 55 bar.

A visual summary of all the previous high-pressure (>10 bar) combustion diagnostics efforts (to the author's knowledge), categorized by techniques and applications, are shown in Fig 1.6. This is based on an extensive literature review, though admittedly some works may be inadvertently omitted. Most studies have been conducted after the year 2000, corresponding to simultaneous technical advancements in lasers and other optical hardware. LAS has been utilized the most to study gas properties in various types of combustion devices. Out of these devices,

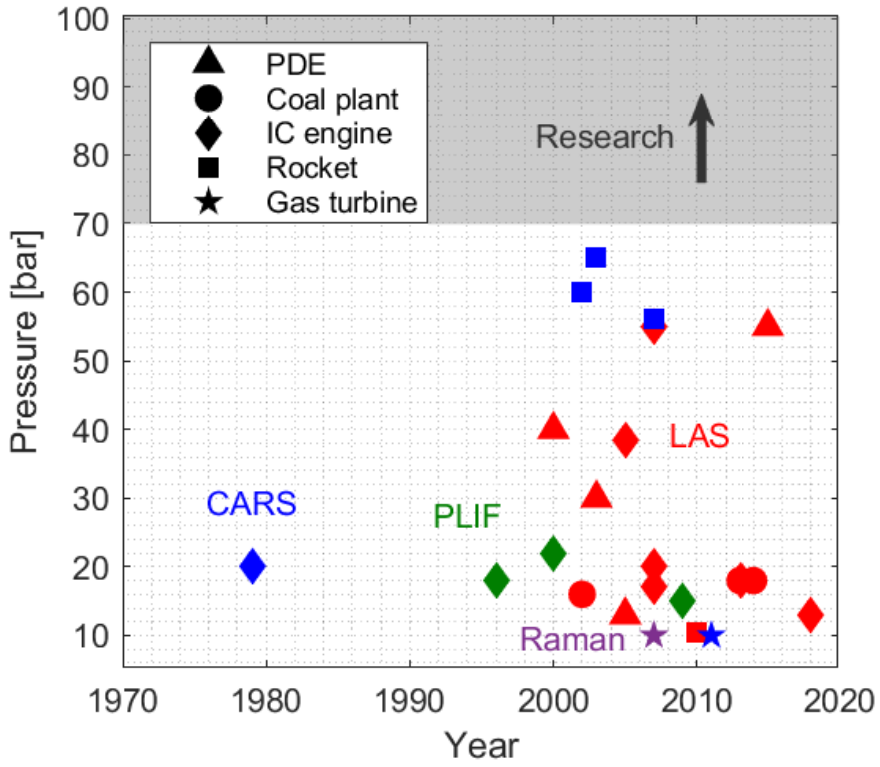

Figure 1.6: Previous studies of various optical diagnostic techniques in a practical combustion devices operating at elevate pressure (>10 bar).

only few attempts were made on rocket combustors, while most studies were conducted in different types of internal combustion engines. Despite many efforts to advance optical diagnostic techniques, there has been no successful optical measurements on practical combustion devices operating above 65 bar. This contrasts the strong need to have diagnostic capability to characterize combustion at higher pressure, which is focus of this dissertation. More details on the previous studies found in the literature review can be noted in Table 1.2.

1.3 Overview of the dissertation

This dissertation describes recent advancements in mid-infrared laser absorption spectroscopy for sensing in harsh high-pressure and high-temperature en-

Table 1.2: Details on previous studies of various optical diagnostic techniques in a practical combustion devices operating at elevate pressure (> 10 bar).

Method	Authors	Year	Species	T_{max} [K]	P_{max} [bar]	Application
LAS	S.T. Sanders et al [35]	2000	H_2O (1343, 1392, 1799 nm), soot (1290, 1643 nm)	~2900	~40	PDE
	E. Schlosser et al [28]	2002	K (769.9 nm, 767.5 nm), O_2	~1650	~16	Coal plant
	S.T. Sanders et al [38]	2003	Cs (852 nm)	~4000	~30	PDE
	D.W. Mattison et al [36]	2005	CO_2 (266, 306 nm), OH (306.3 nm)	~3800	~13	PDE
	L.A. Kranendonk et al [34]	2005	H_2O (1374 - 1472 nm)	~1350	~38.5	HCCI engine
	L.A. Kranendonk et al [39]	2007	H_2O (1335 - 1373 nm)	~770	~17	Piston engine
	G.B. Rieker et al [31]	2007	H_2O (1345, 1388 nm)	~1050	~20	IC engine
	D.W. Mattison et al [2]	2007	H_2O (1348, 1385 nm)	~1700	~55	HCCI engine
	A.W. Caswell et al [40]	2010	H_2O and CH_4 (1329 - 1667 nm)	~2000	~10.5	Combustor
	K. Sun et al [29]	2013	CO (2.3 μm), CO_2 (2 μm), H_2O (1.4 μm)	~1800	~18	Coal gasifier
	O. Witzel et al [32]	2013	H_2O (1369 nm)	~600	~18	IC engine
	R. Sur et al [30]	2014	CO (2.33 μm), CO_2 (2.02 μm), CH_4 (2.29 μm), H_2O (1.35 μm)	~400	~18	Coal gasifier
	C.S. Goldenstein et al [1]	2015	CO_2 (2.7 μm), H_2O (1.4 μm, 2.5 μm), CO (4.8μm)	~3500	~55	PDE
	S. Bürkle et al [33]	2018	H_2O (1391, 1392 nm)	~770	~13	IC Engine
CARS	I.A. Stenhouse et al [24]	1979	Propane (528 nm), N_2 (607 nm)	~500	~20	IC engine
	J. Smith et al [25]	2002	H_2	~2000	~60	H_2/LOX combustor
	F. Grisch et al [23]	2003	H_2 (3983 - 4173 cm^{-1}), H_2O (3500 - 3800 cm^{-1})	~3000	~65	H_2/LOX combustor
	F. Grisch et al [26]	2007	CH_4 (2917 cm^{-1})	~960	~56	CH_4/LOX combustor
	M.P. Thariyan et al [27]	2011	N_2 (1355 cm^{-1}), CO_2 (1390 cm^{-1})	~2000	~10	Gas turbine
PLIF	C. Schulz et al [20]	1996	NO (224, 247.9nm)	~2300	~18	SI engine
	S. Einecke et al [21]	2000	3-pentanone (248, 308nm)	~650	~22	SI engine
	D.A. Rothamer et al [22]	2009	3-pentanone	~600	~15	IC engine
Raman Scattering	L. Wehr et al [41]	2007	550 - 700 nm (CO_2,O2, CO, N_2, CH_4, H_2O, H_2)	~2700	~10	Gas turbine

vironments, with specific applications to rocket combustion. The dissertation is structured in six chapters. After the introduction, the second chapter reviews the important background on mid-infrared laser absorption spectroscopy and challenges of laser absorption spectroscopy at extreme combustion conditions. Chapter 3 demonstrates the design, development, and deployment of carbon monoxide sensing strategies, with applications to liquid rocket engines operating at up to 70 bar. Chapter 4 exhibits the advancement of the sensing techniques discussed in chapter 3, employing line mixing effects to extend measurement capability up to 105 bar in pressure. In addition to carbon monoxide, quantitative temperature and carbon dioxide measurements are presented. Chapter 5 includes a detailed study of line mixing and broadening of CO_2 at high temperatures and high pressures, a spectral model from which was utilized in measurements demonstrated in chapter 4. A brief summary of line mixing and broadening of CO at high temperatures and high pressures is also briefly discussed. Each chapter is intended to be able to largely stand alone with modest referencing across chapters to avoid redundancy.

CHAPTER 2

Background on Mid-infrared Laser Absorption Spectroscopy

2.1 Introduction

Laser absorption spectroscopy (LAS) has been developed and employed over the past several decades to characterize combustion via measurements of temperature, pressure, species, and velocity. Many advantages such as non-intrusiveness, high temporal resolution, and a calibration-free nature promoted LAS as one of the most established sensing techniques for practical combustion devices. The infrared wavelength domain enables access to most combustion species with an intrinsic vibrational dipole and transition strengths of select species are shown in Fig. 2.1.

Historically, most available lasers and optical hardware were developed to operate in the near infrared (760–2500 nm). The primary motivation for advancement of hardware was telecommunication development in 1990s; not for optical gas sensing. Consequently, initial LAS sensing strategies exploited the commercially developed hardware to probe species available in the near-infrared at their overtone and combination bands. This limited sensing capability of LAS for combustion applications, since the fundamental vibrational bands of most combustion species—where transitions are order of magnitude stronger than overtone and combination bands—were only accessible in the mid-wave infrared (2.5–12 μm). Over time, effort has been devoted to the advancement of lasers and optical hardware in the mid-infrared, leading to emergence of more robust and compact semi-conductor lasers such as quantum cascade lasers (QCLs), which

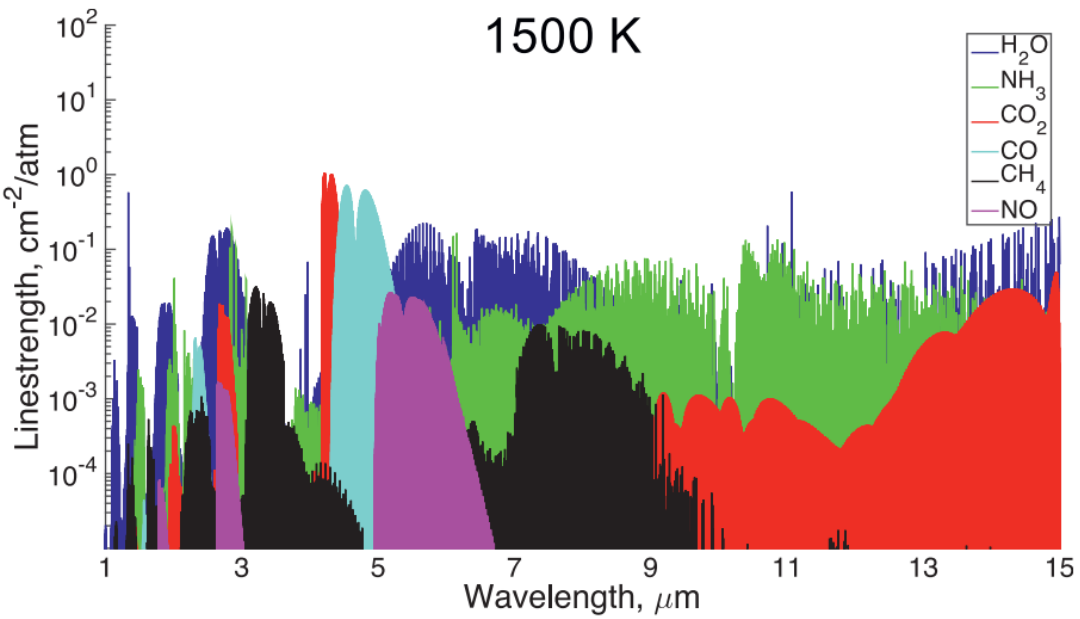

Figure 2.1: Linestrength of combustion relevant species [42]

operate in the mid- to far-infrared(~3.5–100 μm) and interband cascade lasers (ICLs), which bridge the wavelength gap between QCLs and diode lasers.

In this chapter, LAS will first be covered followed by two LAS techniques used in this work for temperature and species measurement. Toward the end of the chapter, the challenges of LAS at extreme combustion conditions will be addressed. The strategy to overcome these challenges will conclude the chapter. More thorough reviews of laser absorption spectroscopy can be found in the literature [16, 42].

2.2 Fundamentals of Laser Absoprtion Spectroscopy

Molecules with an intrinsic dipole moment can absorb radiation when the frequency of the light is resonant with the difference between two discrete energy states of the molecule. The relationship between the frequency of the absorbed

photon and the spacing between the two energy states is given by Plank's Law:

$$\Delta E = E_{upper} - E_{lower} = h\nu \tag{2.1}$$

E represents the energy level associated with a species' quantum state, h is the Plank constant, and ν is the frequency of the corresponding light. The ro-vibrational transition refers to concurrent change in vibrational and rotational state, leading an individual rotational transition to occur within the associated vibrational band (a group of transitions with equivalent change in vibrational energy). Each of these unique transitions is broadened by several mechanisms, which are important factors in understanding challenges of LAS associated with extreme combustion conditions. More details are discussed later in this chapter.

The Beer-Lambert law shown in eq. 2.2 is the governing equation for absorption spectroscopy. This equation relates the ratio of the incident and transmitted intensities to the amount of absorption.

$$T_\nu = \left(\frac{I_t}{I_0}\right)_\nu = exp(-k_\nu L) \tag{2.2}$$

Here, T_ν is the transmission at the frequency ν, I_t and I_0 refer to transmitted and incident intensity, respectively, k_ν is the spectral absorption coefficient at frequency ν, and L is the absorption path length. The combined quantity $k_\nu L$ is the spectral absorbance, α_ν. The absorbance is a function of thermophysical properties listed in Eq. 2.3

$$\alpha_\nu = \sum_i x_{abs} S_i(T) \varphi(\nu, T, P, x_{abs}) L \tag{2.3}$$

x_{abs}, the mole fraction, $S_i(T)$ is the temperature-dependent linestrength (transition strength of quantum transition i at temperature T), and $\varphi(\nu, T, P, x_{abs})$ is a lineshape function, which captures the spectral line shape with a Voigt profile, accounting several broadening mechanisms.

As mentioned previously, discrete transitions are broadened by several mechanisms and these features are captured in the lineshape function. The two main mechanisms include the Doppler and the collisional broadening, which are often characterized by the full-width at half-maximum (FWHM). Doppler broadening occurs when the Doppler-shifted frequency—generated due to velocity components of molecules and photon propagating at same (or opposite) direction—is resonant with the absorption transition. The full-width at half-maximum (FWHM) induced from Doppler broadening, ν_D, is expressed in Eq. 2.4

$$\Delta\nu_D = 7.1623 \times 10^{-7} \nu_o \sqrt{T/M} \tag{2.4}$$

where ν_o is the transition linecenter frequency, M is molecular weight and T is temperature [K]. The relationship shown in Eq. 2.4 suggests that the Doppler broadening increases with higher frequency, temperature, and lighter absorbers.

Collisional (pressure) broadening occurs when inelastic collisions reduce a molecule's lifetime in the absorbing energy state. According to Heisenberg Uncertainty Principle, shortening a molecule's lifetime induces greater uncertainty in the energy difference or line position, and thus a broader absorption lineshape. An increase in pressure leads to an increase in the number of collisions and eventually, to broader absorption lineshape. The full-width at half-maximum (FWHM) due to collisional effects, ν_C, is given by Eq. 2.5

$$\Delta\nu_C = P \sum_B x_B 2\gamma_{abs-B}(T) \tag{2.5}$$

where γ_{abs-B} is the temperature dependent collisional broadening coefficient between the absorbing species and perturbing species B, and is specific to each line i. The temperature dependence of the collision broadening coefficient can be captured by a power law:

$$\gamma_i(T) = \gamma_i(T_0)\left(\frac{T_0}{T}\right)^n \tag{2.6}$$

Here, T_0 is reference temperature, usually room temperature, and n is the collisional-broadening temperature exponent. The molecular dependence of the collisional broadening coefficient can be written as: $\gamma \sim {\sigma_{abs-B}}^2/\sqrt{\mu_{abs-B}}$, where σ_{abs-B} is the optical collision diameter and μ_{abs-B} the reduced mass. According to this relationship and Eq. 2.5, species with a small size and large mass are desired to minimize pressure broadening.

Accurate LAS measurement of gas properties require an accurate spectroscopic model and parameters discussed above. Line-by-line simulations, often considered the most comprehensive method, have been extensively utilized for modeling absorption spectra. To support this modeling framework, the dependence of the line positions, strengths, and shapes on gas properties are studied in a precisely controlled experiment, where thermophysical conditions are known, to build an accurate spectroscopic model. Then, this model is used for quantitative inference of gas properties of unknown flow conditions, as shown in Fig. 2.2. Spectroscopic databases such as HITRAN/HITEMP, GEISA, and CDSD possess well-catalogued line-by-line spectroscopic parameters in the infrared for relatively small combustion species. Uncatalogued spectroscopic parameters can be measured in a controlled experimental setup.

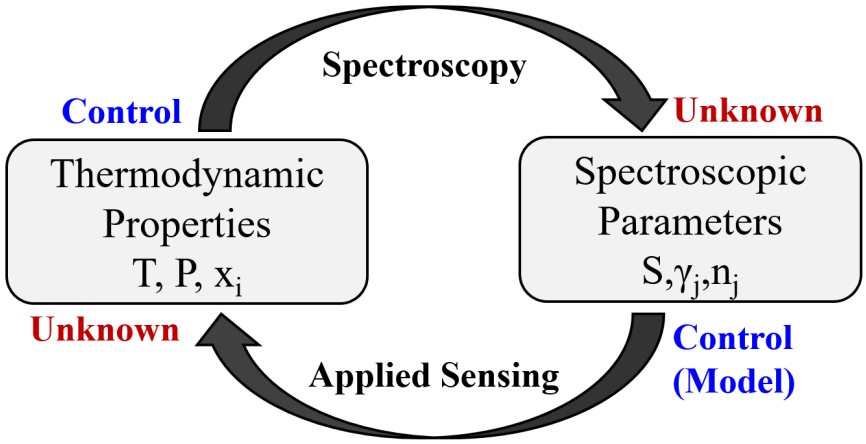

Figure 2.2: Flow diagram demonstrating relationship between thermodynamic properties and spectroscopic parameters and the role of modeling in quantitative sensing

2.3 Techniques of Laser Absorption Spectroscopy

2.3.1 Scanned Wavelength Direct Absorption Spectroscopy

Scanned-wavelength direct absorption spectroscopy (Scanned-DA) is one of the most widely utilized LAS techniques due to its ease of operation and simple data processing. Modern scanned-DA typically employs tunable diode, interband-, and quantum-cascade lasers to spectrally-resolve the target absorption transitions. Selected lasers are tuned to scan across one or a few absorption transitions in the target frequency domain; the light radiation is directed through absorbing gas and onto a photodetector. The brief schematic of scanned-DA is shown in Fig. 2.3. Transmitted and incident signals are used to calculate absorbance, using Eq. 2.3. Integrated absorbance area A_i, given in Eq. 2.7, is often used to simplify the data interpretation process by eliminating the dependence on line shape, $\varphi(\nu, T, P, x_{abs})$.

$$A_i = \int_{-\infty}^{+\infty} \alpha_\nu = S_i(T) P x_{abs} L \tag{2.7}$$

Two transitions with substantial difference in lower-state energy are desired for sensitive thermometry. The ratio of the two measured integrated absorbances can eliminate the pressure, concentration, and pathlength dependence, and

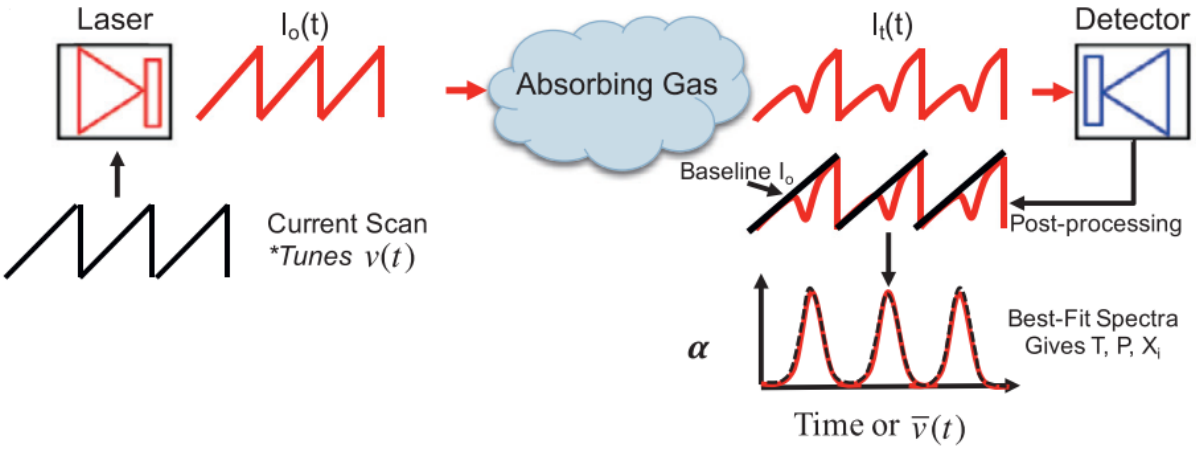

Figure 2.3: Schematics for scanned-wavelength direct absorption spectroscopy [42]

thus enable temperature inference. Once the temperature is known, species concentration can be calculated using Eq. 2.7. The work presented in chapter 5 utilizes scanned-DA to measure collisional broadening coefficients of CO_2 with Ar and study CO_2 line mixing at high temperatures and high pressures.

2.3.2 Scanned Wavelength Modulation Spectroscopy

In harsh environments, extensive mechanical noise, emission, beam steering, and scattering induce intensity distortion, attenuation, and oscillation, therefore complicating scanned-DA post-processing. To account for these challenges, a more sophisticated technique called scanned wavelength modulation spectroscopy (scanned-WMS) has been developed and employed for gas sensing applications. In scanned-WMS, an injection-current tunes the laser in a low frequency waveform to modulate wavelength across the target absorption transitions. Additionally, a high frequency (10 kHz–1 MHz) sinusoidal waveform is superimposed onto the lower frequency waveform. The measured signal is post-processed through a lock-in amplifier and frequency filtered to extract the second harmonic ($2f$) of the high modulation frequency, which is sensitive to the absorption line shape curvatures (differential absorption), and can be de-sensitized to other attenuation noise

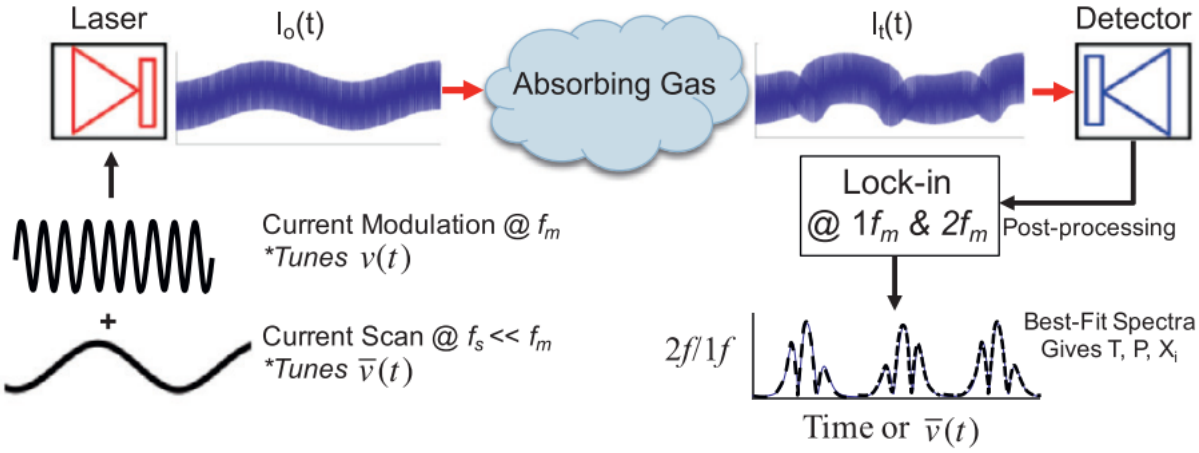

Figure 2.4: Schematics for scanned wavelength modulation spectroscopy [42]

sources that occur at other frequencies. Absorption features with high differential absorption are required for sensitive thermophysical measurements. The second harmonic ($2f$) is typically normalized by first harmonic ($1f$) to eliminate the dependency on intensity variation associated with the harsh environment and compared to a spectral model to infer gas properties. The overall process is demonstrated in Fig. 2.4. The work presented in chapters 3 and 4 demonstrates implementation of scanned-WMS for quantitative species and temperature measurements in a high-pressure rocket combustor.

2.4 Challenges of Laser Absorption Spectroscopy at extreme combustion conditions

Aside from optical challenges associated with harsh environments in rocket combustors, there are some fundamental challenges of laser absorption spectroscopy (LAS) inherent to extreme combustion conditions. Inside the rocket combustion chamber, temperatures are typically above 3000 K and pressure can reach up to hundreds of bar. Most absorption spectra are relatively well-isolated at low temperatures and pressures (around ambient condition); however, increases in temperature and pressure can lead to more complex spectra that are difficult to interpret. As temperatures increase, molecules absorb energy and start propagating to higher energy states, which activates more absorption lines. This temperature-dependence induces a crowding of the spectral domain and changes well-isolated lines to clusters of lines, complicating the quantitative interpretation of the measurement.

As aformentioned in section 2.2, the spectral line width of an absorption transition is a convolution of multiple broadening mechanisms. At elevated pressures, collisional broadening becomes a predominant factor over other broadening mechanisms contributing to spectral broadening, and leads to (1) lower differential absorption, (2) blending of all adjacent lines, and (3) higher chance of interference

with other species. An increase in absorption with pressure can also eventually reach the optically thick limit. More often, it is the blending of discrete spectral features that reduces differential absorption and limits measurement capability due to low SNR. Figure 2.5 demonstrates an absorbance plot of CO at various thermodynamic conditions, illustrating the impact of increases in temperature and pressure discussed above.

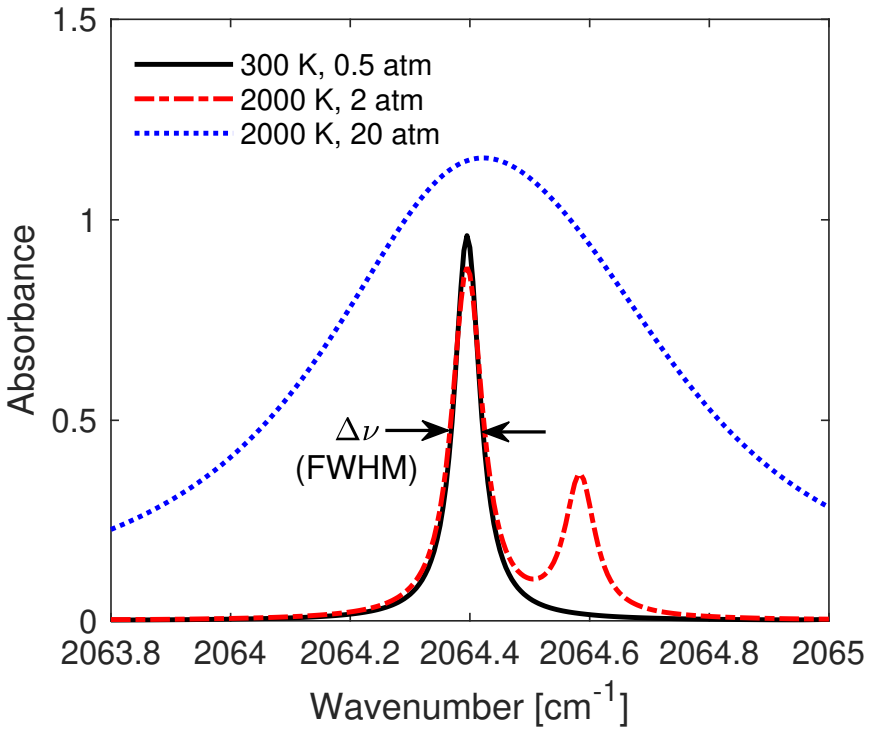

Figure 2.5: Absorbance simulations of CO near 2064 cm^{-1} at various thermodynamic conditions

At high gas densities where intermolecular collisions are sufficiently frequent and strong to cause a shift in energy level populations, a non-ideal phenomenon known as spectral line mixing is observed. This phenomenon becomes more prominent in spectrally dense regions such as bandheads. Line mixing transfers absorption intensity from weak to strong absorption regions, inducing a narrowing of spectral features, which is shown in Fig. 2.6. The absorption spectrum can no longer be expressed as the sum of individual transitions as shown in Eq. 2.3 and

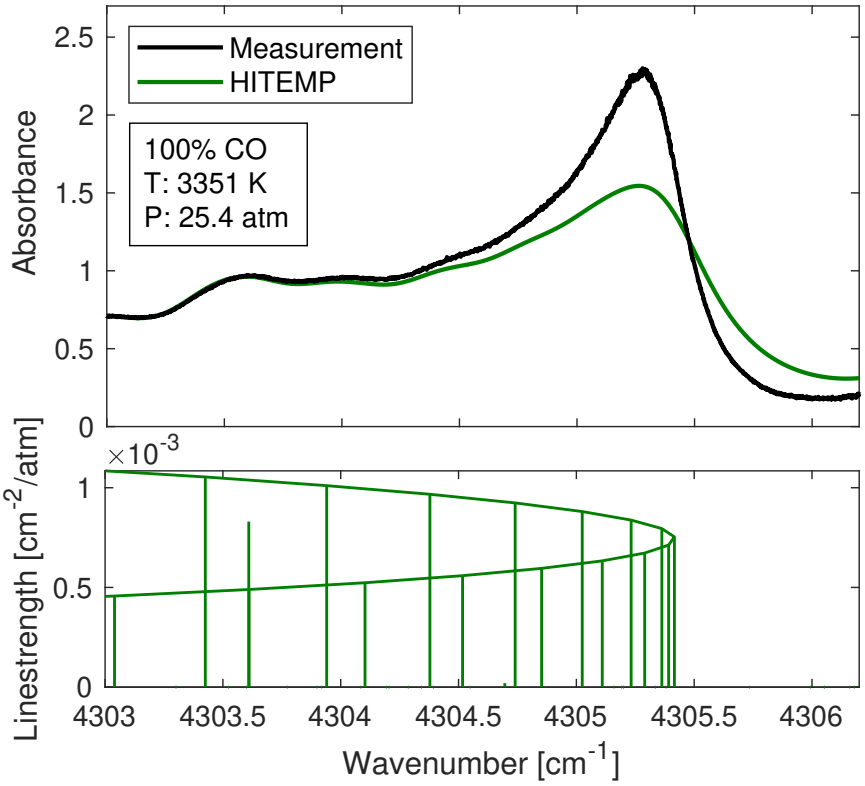

Figure 2.6: Absorbance measurement of the $\upsilon(1 \rightarrow 3)$ first overtone bandhead of CO at 3351 K and 25.4 atm with simulated CO absorbance and linestrength using the HITEMP spectral database [43, 44]

thus, requires a new model which accounts the population transfers induced by line mixing. The spectral modeling process becomes more complicated, however; the spectral narrowing effects of line mixing is strategically valuable to counteract the pressure limit induced by the collisional broadening. To extend the pressure capability of LAS, the novel sensing strategy of exploiting spectral narrowing effects of line mixing is developed and deployed for temperature and species measurement in a high pressure rocket combustor. The advancement of the sensing techniques to extend pressure capability has been demonstrated in chronological order. More details on the fundamental theory and spectral modeling process of line mixing are presented in chapter 5.

CHAPTER 3

Mid-infrared CO sensing in a high-pressure kerosene-fueled liquid rocket combustor

The contents of this chapter have been published in the journal ***Applied Physics B*** *under the full title 'Wavelength modulation spectroscopy near 5 μm for CO sensing in a high-pressure kerosene-fueled liquid rocket combustor' [45]. Portions of the chapter's content have also been presented at the* ***2018 AIAA Aerospace Sciences Meeting*** *[46].*

3.1 Introduction

Hydrocarbon-fueled liquid rocket engines (LREs) are used in many modern launch systems. The high propellant mass fractions and high payload costs of such systems drive an acute need to maximize the mass-specific thrust of the engine. Combustion performance is a principal factor in determining mass-specific thrust, or specific impulse, and is usually quantified by a characteristic velocity ($c^* = p_0 A^* / \dot{m}$) attained by measurements of the chamber pressure and total mass flow rate [47]. Such measurements provide a convenient way to globally quantify the aggregate of multiple processes that occur in the combustion chamber (e.g. vaporization, mixing, reaction), but these measures lack the granularity to quantify combustion progress in the spatial domain (i.e. pressure is nearly constant throughout the chamber). By contrast, knowledge of combustion gas species along the axis of flow in a rocket combustion device provides a means to assess combustion progress relative to equilibrium or a fluid dynamic model. Unfortu-

nately, the harsh conditions internal to hydrocarbon-fueled rocket combustion devices present a uniquely difficult challenge for species measurements. In this paper, we describe a novel approach for in situ detection of carbon monoxide in high-pressure liquid rocket combustors based on mid-infrared laser absorption spectroscopy.

Despite recent advancements in laser absorption spectroscopy (LAS) for studies of air-breathing propulsion systems, there have been very few attempts in developing and applying LAS measurement schemes to rocket propulsion devices. Previous efforts include exhaust plume tomography of water vapor by Caswell et al on a CH_4-GOx rocket motor using a near-infrared (IR) external cavity diode laser [48], near-IR measurements of ammonia and water vapor by Makowiecki et al in a simulated hydrazine thruster plume [49], near-IR water vapor detection by Locke et al in a GH_2-GOx rocket combustor up to 8 atm [50], and infrared measurements of multiple species (N_2O, NO, and CO) by Zeng et al in an ammonium-dinitramide based thrust chamber near 7 atm [51]. Only the latter two works involved LAS measurements of species internal to a rocket combustion chamber and at pressures above ambient. Significantly more effort has been committed to LAS applications in air-breathing propulsion, including higher pressure environments (> 10 atm). Notable previous works include H_2O measurements in the near-infrared in a gas turbine combustor at pressures up to 30 atm by Caswell et al [40] and mid-infrared detection of H_2O and CO above 40 atm in a pulse detonation engine by Goldenstein et al [1] and Spearrin et al [37]. This latter mid-infrared work has informed the design and advancement of the current CO sensor for rocket applications.

Notable differences exist between air-breathing systems and rocket propulsion systems that use similar hydrocarbon fuels, and these differences impact sensor design and operability. Table 3.1 provides a comparison of representative conditions in a typical kerosene-fueled rocket and gas turbine combustor, respectively. While both systems are designed to minimize the onboard mass of propellants

Table 3.1: Example conditions of RP-1-LOx (rocket) and JP-4-Air (gas turbine) combustion gases with representative broadening coefficients of gas components perturbed by nitrogen

	RP-1-LOx	JP-4-Air	$2\gamma_{i-N_2}(300K)$ [cm^{-1}/atm]
ϕ	1.35	0.8	
T_{max}	3600 K	2000 K	
P_{max}	> 50 atm	25 atm	
N_2	--	74%	--
CO	35%	< 1%	0.13
CO_2	12%	11%	0.15
H_2O	32%	10%	0.23
OH	4%	< 1%	0.15
O_2	<1%	4%	--
H_2	11%	$\ll$ 1%	--

per unit thrust, rockets carry both fuel and oxidizer whereas air-breathing systems carry only the fuel. Air-breathing combustors thus typically burn fuel-lean, whereas rockets usually burn fuel-rich to maximize specific impulse. This results in extensive soot formation in the fuel-rich combustion of conventional hydrocarbon rocket fuels (i.e. kerosene) [52]. Without the added heat capacity of nitrogen, rockets also reach much higher combustion temperatures (T > 3000 K), and the acute need for high thrust demands higher chamber pressures (P > 50 atm). The extreme thermodynamic conditions typical of hydrocarbon-fueled rocket combustion generally increase spectral interference through band and line broadening [16]. Sooting associated with fuel-rich combustion leads to beam scattering and window fouling. Differences in oxidizer-to-fuel ratio, combined with the lack of nitrogen, also yields a unique rocket gas composition and associated spectra from which to probe. With these factors in mind, a unique sensing strategy is required for species measurements in hydrocarbon-fueled rockets. In the following sections, we detail the CO sensor design and development, from theoretical approach to demonstration on a kerosene-fueled rocket combustor.

3.2 Theory

3.2.1 Absorption Spectroscopy

The theory of absorption spectroscopy has been thoroughly discussed in previous works [53] [54] and will only be briefly outlined to describe the analytical approach and introduce notation. The fundamental relationship governing LAS measurements is the Beer-Lambert law given by equation 3.1, which relates thermodynamic gas properties and mole fraction, x_{abs}, to incident light intensity (I_0) and transmitted light intensity (I_t) over the optical path length, L.

$$\alpha_\nu = -\ln\left(\frac{I_t}{I_0}\right)_\nu = \sum_i x_{abs} S_i(T) \varphi(\nu, T, P, x_{abs}) L \tag{3.1}$$

In projecting monochromatic light across a gas medium (i.e. rocket combustor), the ratio of light intensities can be measured to determine the spectral absorbance, α_ν, of molecules with quantum energy transitions resonant at the optical frequency, ν. The spectral absorbance can then be directly related to the thermodynamic gas properties and mole fraction of the absorbing molecule through the spectral line-strength, $S_i(T)$, and line-shape function, $\varphi(\nu, T, P, x_{abs})$. Developing an LAS sensor for species measurements in high-pressure and high-temperature environments requires an accurate accounting of these spectroscopic parameters for each line i that contributes to the local spectra.

The spectral line-shape can generally be well represented by accounting for Doppler and collisional broadening, which capture temperature and pressure dependencies, respectively, with an appropriate line-shape function (e.g. Voigt). Collisional broadening has a pronounced effect at the high pressures associated with rocket combustion, leading to undesirable blending of neighboring lines, or spectral interference, as well as reduced differential absorption that limits range. This broadening effect is represented by a collisional line-width, $\Delta\nu_c$, defined in equation 3.2. Here, $2\gamma_{abs-j}$ is the collisional broadening coefficient between

perturbing species j and the absorbing species, and is specific to each line i. Its temperature dependence is typically captured by a power law (equation 3.3).

$$\nu_c = P \sum_j x_j 2\gamma_{abs-j} \tag{3.2}$$

$$\gamma_i(T) = \gamma_i(T_0)\left(\frac{T_0}{T}\right)^n \tag{3.3}$$

To minimize the detrimental effects of line broadening, and maximize pressure range, a molecule with a low collisional broadening coefficient is advantageous. The molecular dependence of collisional broadening can be distilled to the optical collision diameter and reduced mass, $\gamma \sim \frac{d_{ij}^2}{\sqrt{\mu_{ij}}}$, such that a combination of small size and large mass is desired [16].

Table 3.1 compares representative collisional broadening coefficients for the various components of hydrocarbon combustion gases. First we note that the homonuclear diatomics are not infrared active. Fortunately, in contrast to lean air-breathing systems, the high-temperature fuel-rich conditions of hydrocarbon fueled rockets provide for a large fraction of infrared active diatomic species in the equilibrium combustion product mixture. The most abundant of these species is CO, which also exhibits a comparatively low collisional broadening coefficient relative to the other infrared active species (CO_2, H_2O, OH), resulting from a smaller optical diameter than the larger polyatomic species, and a larger molecular mass than OH. Consequently, CO can have substantially less collisional broadening at high pressures typical of modern rocket propulsion systems, which lessens the interference of neighboring lines, preserves differential absorption, and provides a theoretical basis for LAS measurements in rocket combustion flows above the pressure limits of previous works discussed in section 1.3.

3.2.2 Scanned Wavelength Modulation Spectroscopy

A scanned-wavelength modulation spectroscopy (WMS) technique, with normalized second harmonic ($2f$) detection, was employed in this work to measure the absorption of carbon monoxide. Scanned-WMS has proven advantageous in harsh environments where entrained particles lead to substantial raw signal noise (scattering and beam steering) and at high pressures (> 50 atm) where the signal absolute baseline is unavailable [53] [29]. Measurements are conducted by rapidly injection-current tuning the laser with a high-frequency sinusoidal waveform superimposed on a lower frequency waveform to modulate wavelength over the target absorption feature. The raw detector signal is post-processed through a lock-in amplifier and frequency filtered to isolate the second harmonic ($2f$) of the modulation frequency, which is sensitive to spectral line-shape curvature and can be compared to a spectral model to infer gas properties. The slower scan is used to attain spectral resolution of the harmonic signals. The method is convenient for eliminating noise at frequencies outside a prescribed passband, set by the selection of the modulation frequency and frequency filter. Additionally, $1f$-normalization of the $2f$ signal eliminates the dependency on laser intensity variation due to emission and non-absorbing transmission losses [55], important for a high-temperature sooting environment.

In scanned-WMS, the optical output frequency of the laser, ν(t), can be modeled with equation 3.4, where $\bar{\nu}_L$ represents the center frequency/wavenumber of the modulation, a_S and a_M are the amplitudes or depths of the slow scan and modulation waveform, f_S and f_M are the scan and modulation frequencies, and ψ_s and ψ_M are the corresponding phase shifts.

$$\nu(t) = \bar{\nu}_L + \nu_S(t) + \nu_M(t) = a_S \sin\left(f_S t + \psi_S\right) + a_M \sin\left(f_M + \psi_M\right) \tag{3.4}$$

The user has some control in prescribing these parameters, subject to laser tuning characteristics, which directly affect the harmonic signal strength and

signal-to-noise ratio (SNR) of the species measurement. Section 3.4 discusses the approach used to determine modulation settings for the rocket combustor application and the spectral model from which species concentration is inferred by comparison to the WMS measurement. First, section 3.3 describes the wavelength selection that prescribes $\bar{\nu}_L$.

3.3 Wavelength Selection

For the target measurement, there are three primary criteria for wavelength selection: (1) strong differential absorption within the laser tuning range, which translates to a large WMS-2f signal, (2) minimal interference with other combustion species, namely carbon dioxide and water, and (3) temperature insensitivity. The strongest CO absorption in the infrared occurs near the fundamental vibrational frequency (2140 cm^{-1}), and this mid-infrared domain has recently become accessible with room-temperature quantum cascade lasers that can implement rapid tuning techniques (e.g. scanned-WMS). Figure 3.1 shows the fundamental CO absorption band centered near 4.7 μm with the neighboring CO_2 and H_2O

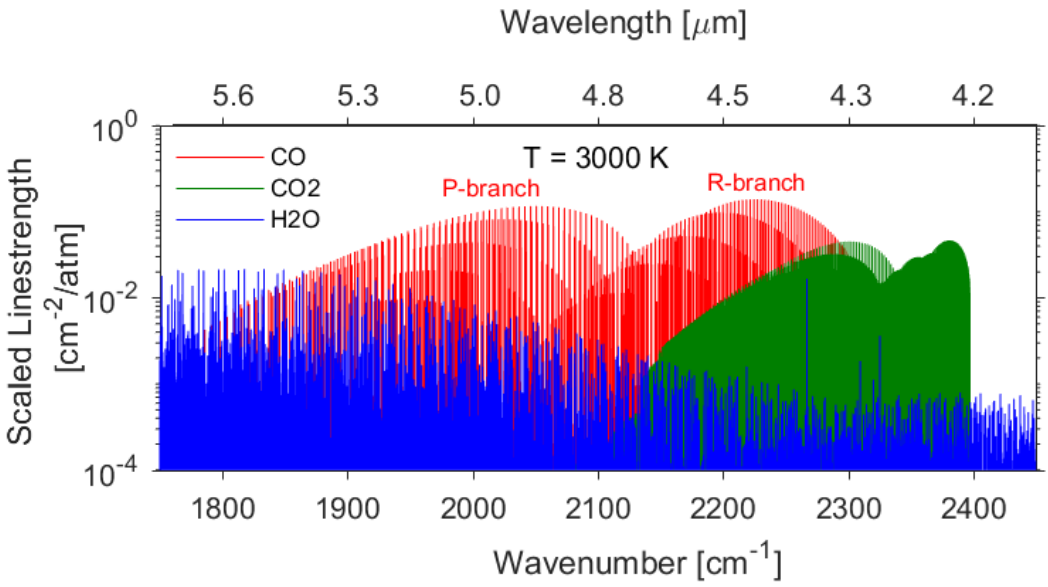

Figure 3.1: Absorption line-strengths of CO, CO_2, and H_2O at 3000 K (HITEMP [44])

absorption bands within the surrounding domain of 4.1 to 5.7 μm. This relatively broad spectral line-strength survey at 3000 K indicates regions of the CO band that may be favorable for low interference measurements in a high-temperature rocket environment. The dense CO_2 spectra, comprised of many lines and small line spacing, interferes substantially with the R-branch of CO at frequencies above 2100 cm^{-1}. The H_2O spectrum similarly overlaps with CO throughout the domain of interest but is less crowded compared to the CO_2 band. The larger spacing between water lines allows for some potentially low-interference spectral windows, and indicates the lower-frequency P-branch of CO as a favorable domain.

Within the P-branch of the fundamental CO band, the spectral lines near 2060 cm^{-1} have been utilized previously for LAS sensing in air-breathing propulsion flows [56] [1], and this wavelength was initially considered for the current work. However, detailed absorption simulations suggest that the much higher temperatures and pressures expected in the rocket environment introduce substantial CO_2 interference at this wavelength associated with a combination of Boltzmann broadening of the neighboring CO_2 $\bar{\nu}_3$ band with increased temperature and individual line broadening with increased pressure. To avoid this CO_2 interference, we look to lower frequencies in the P-branch. Figure 3.2 shows an absorption simulation, using the HITEMP spectroscopic database [44], of a representative condition for kerosene-oxygen rocket combustion at 60 atm at select spectral domains near 4.9 μm. This figure highlights the CO_2 interference near 2060 cm^{-1}. Note that thermochemical properties, as assigned in the absorption simulation, have been estimated using the NASA Chemical Equilibrium with Applications (CEA) tool.

A survey of the remainder of the simulated spectrum in the domain of 1950 to 2100 cm^{-1} revealed the CO absorption feature near 2008 cm^{-1} as an attractive target (also shown in figure 3.2) [53]. The local absorption is primarily comprised of two rovibrational transitions which blend into one spectral feature at elevated pressure. The P(31) line in the $\nu(0\rightarrow1)$ fundamental band makes the dominant contribution but the P(20) line in the $\nu(2\rightarrow3)$ hot band also contributes at most ex-

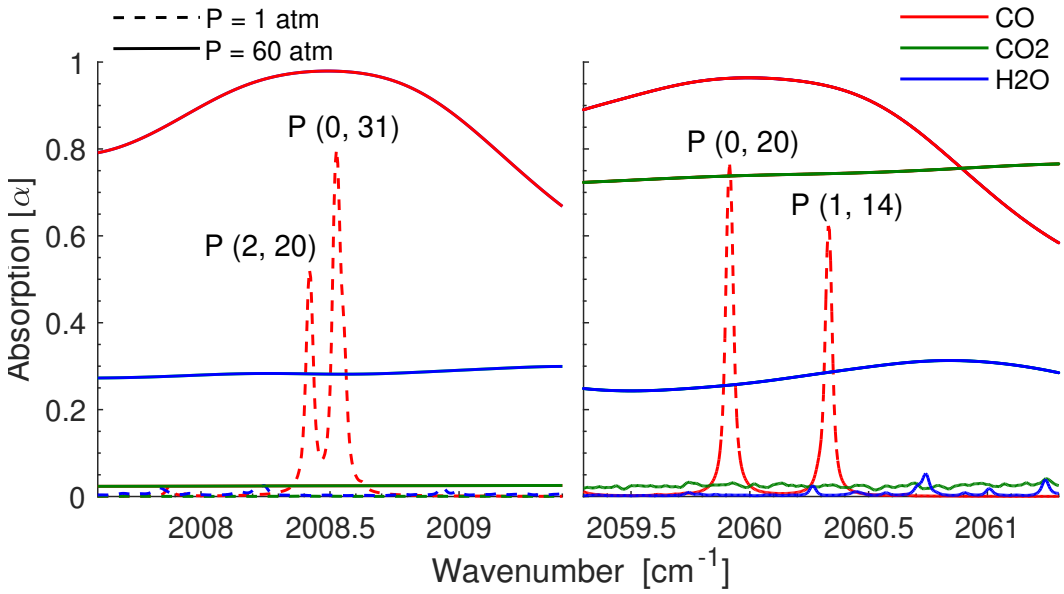

Figure 3.2: Absorption simulations near 2008 cm^{-1} and 2060 cm^{-1} at expected equilibrium condition; T = 3500 K, X_{CO} = 0.3, X_{CO_2} = 0.15, X_{H_2O} = 0.35, L = 2.54 cm

pected conditions. To a lesser degree, the neighboring P(26) line near 2006.8 cm^{-1} in the $v(1\rightarrow2)$ band makes a contribution above 50 atm. Most notably, the domain near 2008 cm^{-1} has significantly less CO_2 interference than 2060 cm^{-1}, and H_2O interference is similar with negligible differential H_2O absorption. In addition to less interference, differential CO absorption is also slightly stronger at 2008 cm^{-1} at the target high-pressure condition, as broadening coefficients for these higher rotational quanta (J) lines are smaller. Due to these advantages, the CO absorption feature near 2008 cm^{-1} was selected for this sensing application. Table 3.2 specifies the relevant spectroscopic line parameters in this domain, taken from the HITEMP database and from the experimental and modeling work of Hartmann et al [57]. In modeling the spectra, a Voigt line-shape function is used, which has been shown to be suitable at similar gas densities for other CO lines within the fundamental band [37]. In calculating line broadening, the gas composition is approximated from thermochemical calculations. As table 3.2 indicates, broadening coefficients are available for most collision partners. For the 10 to 15% of species

Table 3.2: Spectroscopic line assignments and collisional-broadening for the CO lines of interest [57] [58]. Note: γ (300 K) in units of $10^{-3}*$ (cm^{-1}/atm) and S at 296 K

P (v'', J'')		P (0,31)	P(2,20)	P(1,26)
v_0 (cm^{-1})		2008.53	2008.42	2006.78
E''(cm^{-1})		1901.1	5051.7	3477.6
S (cm^{-2}/atm)		6.48 x 10^{-3}	2.78 x 10^{-9}	5.09 x 10^{-6}
CO–H_2O	γ	94.9	119	106
	n	0.61	0.71	0.66
CO–CO_2	γ	40.2	51.8	44
	n	0.47	0.5	0.48
CO–N_2	γ	40.9	52.2	46.3
	n	0.47	0.57	0.52
CO–CO	γ	43	55	48
	n	0.5	0.5	0.5
CO–O_2	γ	43.2	46.9	45
	n	0.56	0.56	0.56

for which broadening data is not available (e.g. OH, H_2, radicals), the broadening per unit pressure is assumed to equal that of the balance gas.

As for the final wavelength selection criteria, low temperature sensitivity is desired to minimize influence of temperature uncertainty. It is found that the high lower state energies of the lines near 2008 cm^{-1} lend to low temperature sensitivity. This is discussed in the context of measurable WMS signals in section 3.4.

3.4 Sensor Development

This section describes key elements of sensor development required for successful application of the spectroscopic sensor design. These elements include the refinement of laser control and tuning parameters, spectral modeling and interpretation of the WMS harmonic signals, optical engineering, and facility interface and setup.

3.4.1 Optimizing laser tuning parameters

Within the framework of scanned-WMS, the tuning depths (a_S and a_M) and frequencies (f_S and f_M) can be adjusted to optimize signal quality (i.e. signal-to-noise ratio) for a given gas condition or application environment. A basic analytical model based on laser tuning characteristics, measured in the laboratory, can be used to simulate WMS harmonic signals and inform parameter optimization[13]. Two guiding principles in the selection of these parameters should be noted: (1) Maximizing the WMS-2f generally maximizes signal-to-noise ratio, and this signal increases with the level of differential absorption spanned during wavelength modulation. At high-pressures where laser tuning range is often limited to a fraction of the absorption line-width, the WMS-2f tends to increase monotonically with modulation depth [58]. (2) Modulating at higher frequencies enables higher time

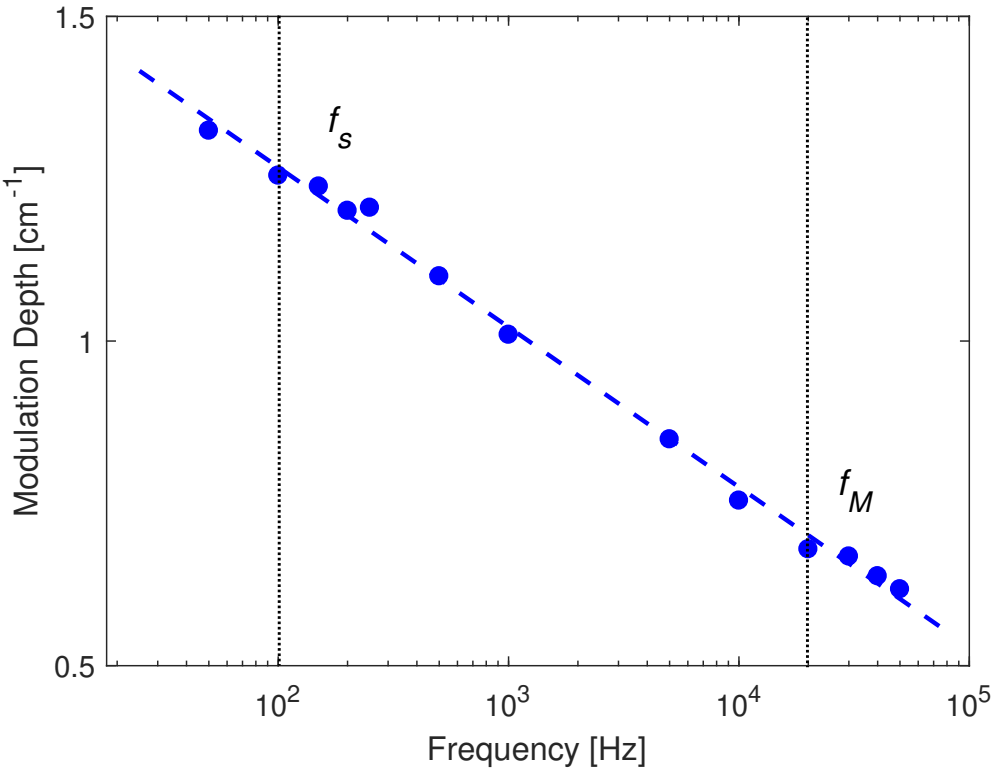

Figure 3.3: Measured modulation depth at maximum injection current amplitude (±45 mA) as a function of laser modulation frequency

resolution measurements and tends to improve noise rejection. Time resolution or sensor bandwidth is determined by the passband frequency which is a prescribed fraction of the modulation frequency. Additionally, mechanical noise in the system (vibrations, beam steering, etc.) tends to be more intense at relatively low frequencies (< 10 kHz) and can be avoided by shifting the absorption information to higher frequencies, thus improving SNR. Unfortunately, laser tuning depth has an inverse relationship with frequency, and thus a compromise is required between the competing demands of signal quality and time-resolution.

Figure 3.3 shows the maximum modulation depth versus frequency for the quantum cascade laser used in this work. The maximum modulation depth is determined at each frequency by inputting the maximum injection current range permitted, and measuring the relative wavenumber achieved calibrated against the free-spectral range of a germanium etalon, through which the light is projected. Maximum modulation depth is shown to decrease logarithmically with frequency. Additionally, the benefit of using a large modulation depth for this high-pressure application is illustrated in figure 3.4 by simulations of the relative WMS-2f signal (at 2008.52 cm^{-1}) versus pressure at different modulation depths achievable with the laser. Modulating at a depth greater than 0.4 cm^{-1} is shown to enable significantly expanded pressure range for the sensor. It should be noted that mid-infrared quantum cascade lasers have improved considerably in current tuning range in recent years, underlying this advancement in capability. Nevertheless, a trade-off between tuning frequency and signal strength is evident

Adding a low frequency waveform to the high frequency modulation in order to spectrally resolve the harmonic signals reduces the available injection current for modulation, and therefore should be minimized in scan depth. The main purpose of the slow scan in this application is to ensure that a local peak is measured, allowing for some uncertainty in pressure shifting of the target transitions. In this case, fully resolving the harmonic spectra is not required, and a low-amplitude dithering of the slow scan (i.e. small a_S) over the local peak is acceptable. For the

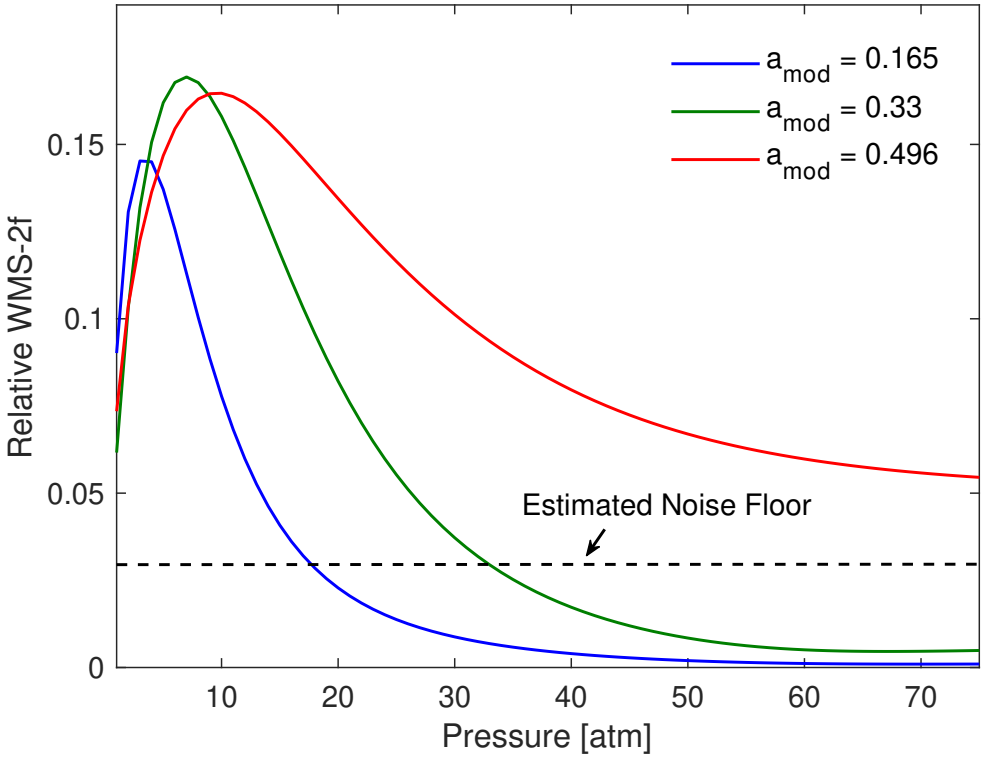

Figure 3.4: Simulated WMS-2f (background subtracted) near 2008 cm^{-1} as a function of pressure for various modulation depths at expected equilibrium; T = 3500 K, X_{CO} = 0.32, L = 2.54 cm

present work, a scan depth and frequency of 0.141 cm^{-1} and 100 Hz were selected, respectively, to capture the local 2f peak signal associated with the absorption feature. With the remaining injection current budget, a modulation depth and frequency of 0.496 cm^{-1} and 20 kHz were chosen to yield adequate WMS-2f signal strength at the highest possible frequency.

3.4.2 Simulation of scanned WMS harmonic signals

To infer species concentration, a model is required to compare simulated signals (in which species concentration is an input), to measured signals. Here, we follow the approach of Sun et al [59], in which a measured background laser intensity (I_0), at the scanned-WMS settings, is combined with a simulated absorbance

versus time function, using $\nu(t)$ per equation 3.4, to generate a simulated laser transmission signal (${}^{S}I_t$). The simulated absorbance spectrum is created using the spectroscopic parameters detailed in section 3.3, and the optical frequency response $\nu(t)$ is characterized in the laboratory, and contains the selected laser tuning parameters (f_S = 100 Hz and a_S = 0.141 cm^{-1}, f_M = 20 kHz and a_M = 0.496 cm^{-1}). The simulated transmitted intensity (${}^{S}I_t$), can then be processed through a digital lock-in amplifier and low-pass filter in the same manner as the measured transmitted intensity (${}^{M}I_t$). The lock-in analysis extracts the WMS harmonic signals which can be compared between the simulation and measurement, after background subtraction and normalization.

The simulation process at the scanned-WMS settings used in this work is illustrated in figure 3.5. The measured background laser intensity (I_0) is shown in blue with a 20 kHz modulation frequency. Simulated transmission signals at a representative condition (30 atm) for the kerosene-oxygen rocket combustor are also shown at two different input values of CO mole fraction (red and green) and reflect the molecular absorption. The corresponding background-subtracted WMS-$2f/1f$ harmonic signals, extracted from lock-in analysis of these transmission signals, are shown in the lower sub-figure. This sub-figure also shows the variation of the harmonic signals at 100 Hz where the slower scan crosses over the local WMS-$2f/1f$ peaks. This simulation method is used to infer species abundance by iterating mole fraction to converge the simulated signal with measurement, as will be shown in section 3.5.

With a complete spectral model, we now revisit the temperature sensitivity of the measurement technique. At the selected laser settings, we iterate the simulation process over a range of possible temperatures and pressures in the rocket combustor, generating a matrix of WMS harmonic signals, from which a numerical derivative of the WMS-$2f$ can be taken with respect to temperature at any given condition. Normalizing this derivative with respect to the signal magnitude and temperature (i.e. (dS/S)/(dT/T)), we can determine the uncertainty of the

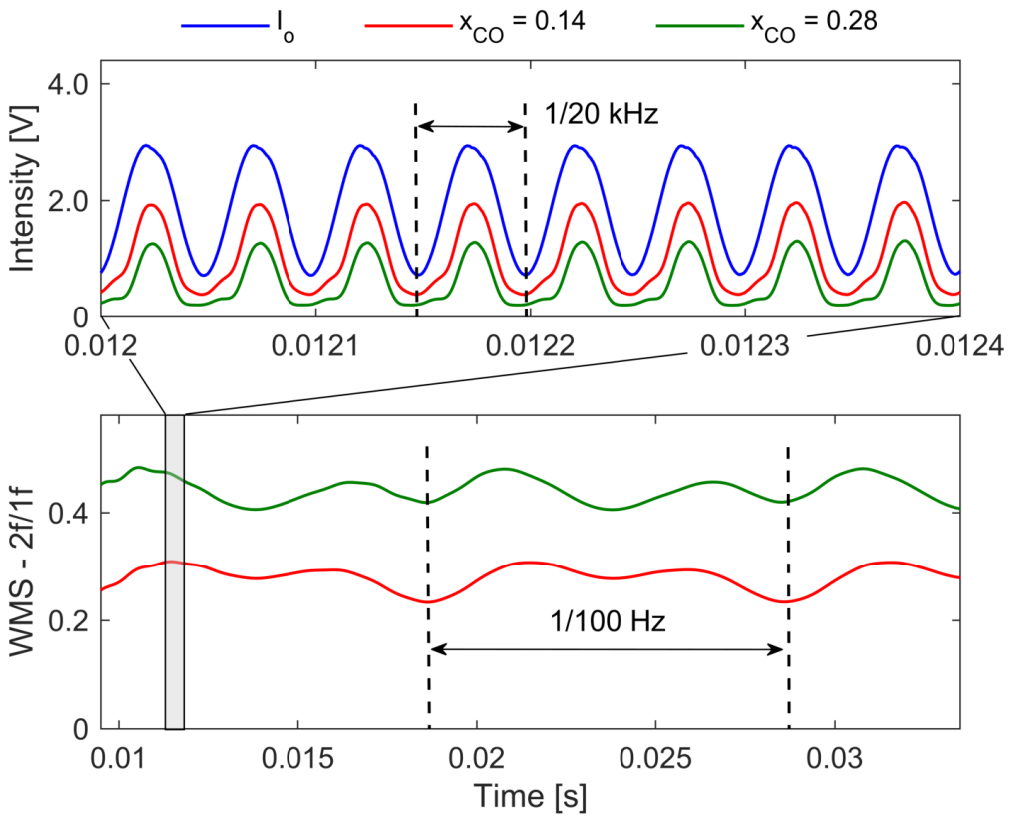

Figure 3.5: Scanned-WMS intensity signals with simulated absorbance at different X_{CO} (top), and corresponding WMS-$2f/1f$ harmonic signals after lock-in extraction (bottom); P = 440 psi (30 atm), T = 3570 K, L = 2.54 cm

measured WMS-$2f$ resulting from an uncertainty in temperature on a percentage basis. It can be shown that CO mole fraction is approximately linearly proportional to the WMS-$2f$ signal such that the derivative can approximate the sensitivity of the inferred CO concentration measurement to temperature.

This numerical calculation, conducted as a function of temperature from 800 to 3700 K at distinct pressures, is shown in the lower sub-plot of figure 3.6. The respective line-strengths of the three most dominant transitions that comprise the absorption feature are also shown as a function of temperature (in the upper sub-plot) to assist in interpretation of the temperature sensitivity. For all pressure conditions, temperature sensitivity decreases significantly until it reaches zero where the local WMS-$2f$ reaches a maximum. This generally correlates to the

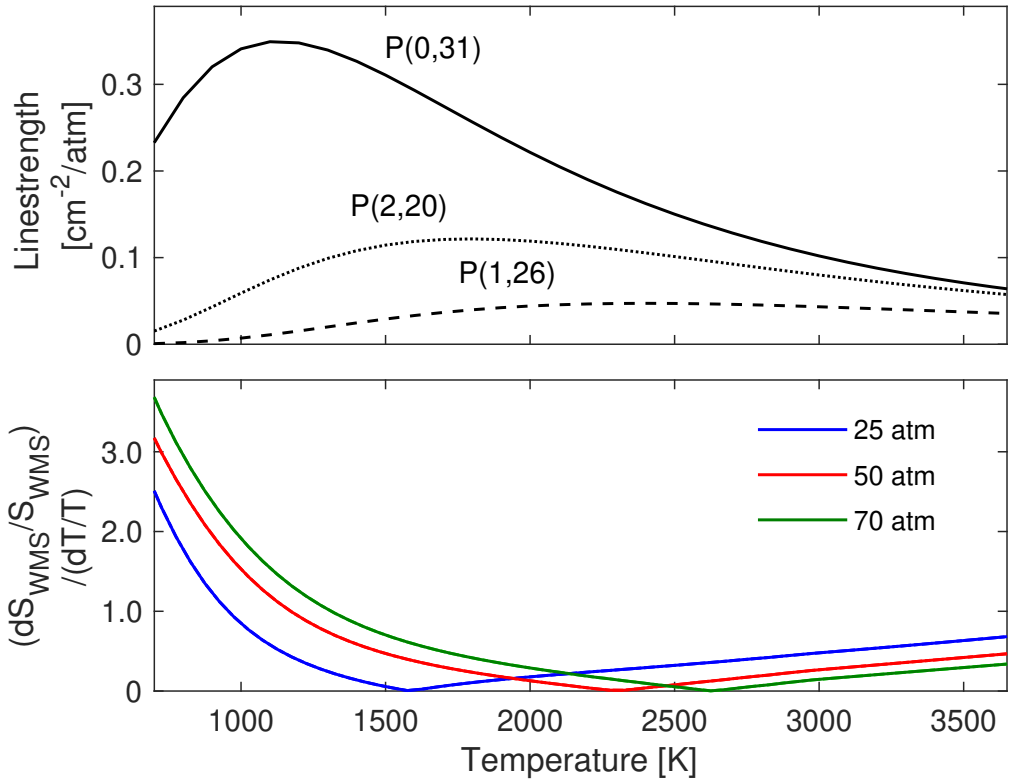

Figure 3.6: Line-strength and temperature sensitivity of WMS-2f signal (background subtracted) near 2008 cm^{-1} as a function of temperature for various pressures; a_{mod} = 0.496 cm^{-1}

maximum of differential absorption related to the summation of contributing line-strengths. The zero point shifts to higher temperatures as pressure increases mainly due to a change in relative contribution from the three transitions. At 25 atm, the P(0, 31) makes the dominant contribution to the signal strength, while at 50 and 70 atm, the P(1, 26) and P(2, 20) lines contribute more substantially. At temperatures above the inflection point, the temperature sensitivities remain low as line-strengths decrease gradually. At the primary conditions of interest (2000 to 3700 K) the temperature sensitivity is mostly less than 0.5 at all pressures. This may be interpreted as estimating that a ~ 10% uncertainty in temperature would yield a ~ 5% uncertainty in species.

3.5 Experimental Setup

In this section we detail the sensor hardware and interface with the liquid rocket test article. Figure 3.7 provides a schematic representation of the integration. The total length of the combustion chamber is approximately 35 cm with a square cross-section of 6.45 cm^2 area. Measurements are taken across a 2.5 cm transverse optical path-length located 32 cm downstream of the single-element injector.

A distributed-feedback quantum cascade laser with ~50 mW output power is used as the single-mode light source to probe the target CO absorption feature near 2008.5 cm^{-1}. The beam is free-space coupled into a hollow-core fiber (2 m length) for remote light delivery using a calcium fluoride coupling lens with a focal length of 100 mm and a multi-axis stage for optical alignment [60]. The fiber output is then re-collimated using another calcium fluoride lens and pitched across the combustion chamber (4 mm aperture) through two wedged sapphire windows (3/8 in. diameter with 1° wedge), which were recessed ~50 cm from the combustion flow path. The beam diameter was estimated to be ~2 mm upon re-collimation. The transmitted light is spectrally filtered to reduce thermal emission and is collected on a thermo-electrically cooled photovoltaic (PV) detector. Both the pitch and catch optics were mounted on kinematic mounts to optimize alignment and maximize the transmitted light intensity during the experiment.

The DFB laser was injection-current tuned to be centered near 2008.52 cm^{-1} and was driven by a scanning sinusoid at 100 Hz and modulation sinusoid at 20 kHz. The respective modulation depths used were 0.141 cm^{-1} and 0.496 cm^{-1}, allowing a maximum wavelength scan range of 0.637 cm^{-1} to partially resolve the pressure-broadened transitions illustrated in Figure 3.2. Raw detector voltage data was typically collected at a sample rate of 5 MS/s in 5 second intervals. Test article hot-fire tests usually spanned 2 to 3 seconds in duration.

In order to mitigate issues associated with the harsh thermo-mechanical environment, a number of practical methods were required to ensure successful

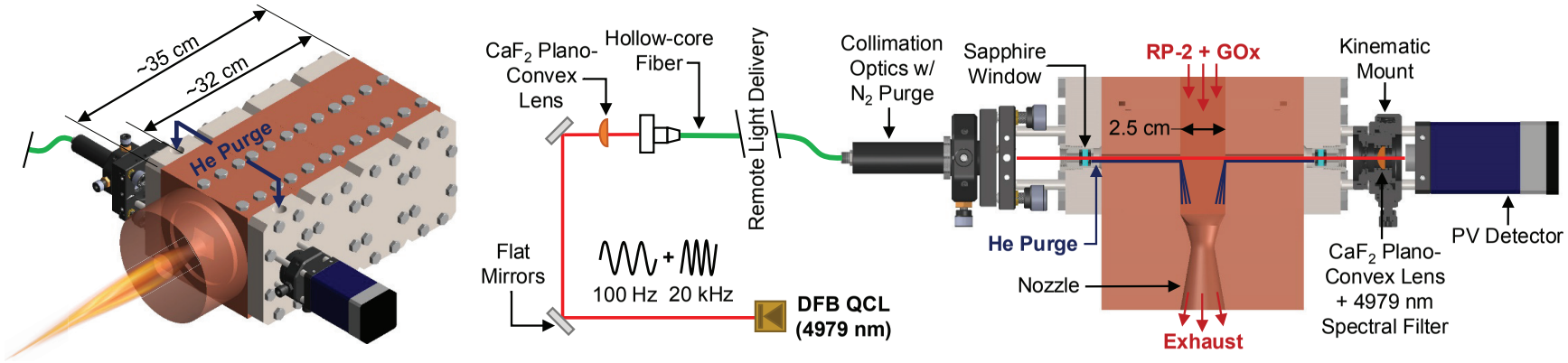

Figure 3.7: Optical interface with RP-2-GOx rocket combustor for high-pressure CO sensing measurements. Graphical depiction of remote-light delivery and collection optics along with implemented He/N_2 purge systems

sensor deployment on the rocket combustor. To displace excessive water vapor in the optical path that could spectrally interfere with CO measurements, nitrogen was fed into the fiber-optic and pitch assembly to purge the hollow-core fiber. Another practical issue was soot deposition on the sapphire windows. A helium purge system was employed in front of the wedged sapphire windows to keep the windows and recess volume clear. The helium purge pressure was iteratively adjusted to be just high enough such that soot formation was not observed (per window inspection between tests), minimizing the penetration depth of the helium into the combustion chamber [52]. Additionally, to counter mechanical vibrations and acoustic perturbations, the laser was mounted to a honeycomb vibration-dampening breadboard and the hollow-core fiber was mechanically supported by a structural shroud. Lastly, due to thermal radiation from the combustor and ambient environment, the photovoltaic detector was mounted to a water-cooler plate to prevent saturation or overheating damage.

3.6 Sensor Demonstration

Initial sensor application occurred at a bipropellant rocket test facility at the Air Force Research Laboratory in Edwards, CA. The facility is used, amongst other purposes, for assessment of the combustion characteristics of hydrocarbon rocket propellants and various injector designs. For the demonstration testing discussed here, kerosene (RP-2) and oxygen were used as the propellants. In situ CO species measurements were conducted in the combustion chamber over a pressure range of 25–70 atm and at oxidizer-to-fuel ratios ranging from 2.5–4.5. The combustion chamber is a stackable modular design, and the optical section was located at the furthest downstream location where chemical equilibrium is most likely achieved, providing a reference point for the measurements. Here we discuss a subset of the data collected to highlight species measurement capability.

Figure 3.8 shows an example test where chamber pressure and O/F ratio

reached 58 atm and 2.59, respectively. The sub-figures show the time-resolved measurements of the WMS-2f/1f signal and pressure along with the inferred species measurement. To infer CO mole fraction, temperature was estimated by thermochemical calculation while chamber pressure was accurately measured via a pressure transducer. From the figure, we can observe the abrupt increase in WMS signal around 1.6 s, corresponding to the introduction of propellants

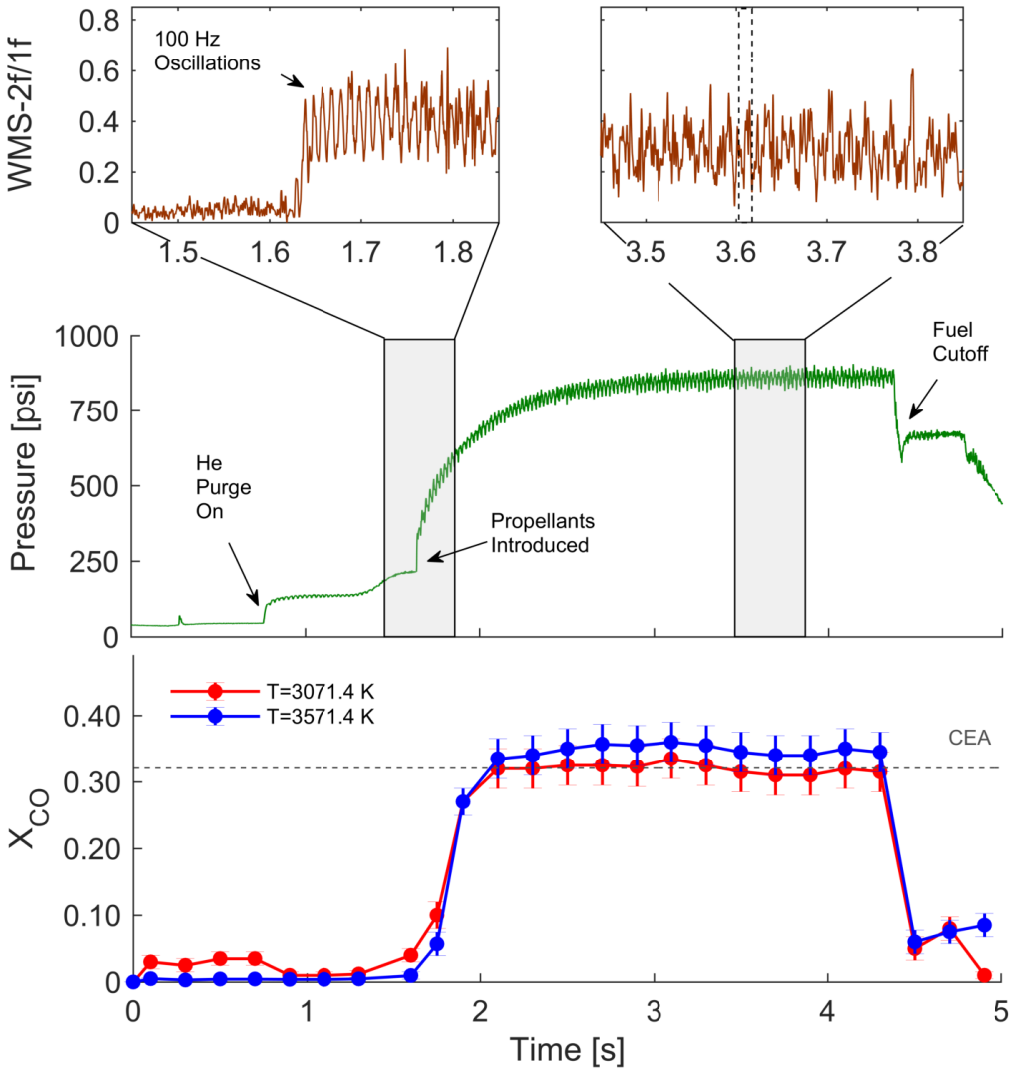

Figure 3.8: Time evolution of chamber pressure, WMS-2f/1f signal (background subtracted), and measured X_{CO} in RP-2-GOx combustor; O/F = 2.59

and ignition. The WMS signal then decreases as pressure increases. Prior to ignition there is an increase in chamber pressure associated with the helium purge gas which is decreased thereafter. Maximum CO concentration occurs at around 3.1 s and decreases slightly as the combustor reaches steady state. The concentration measurement at steady state shows good agreement (< 10%) with equilibrium, calculated to yield X_{CO} = 0.32 at the measured chamber pressure and equivalence ratio (NASA CEA). Precision error is estimated to be ~ 9% in this case, an inverse of the signal-to-noise ratio. In order to estimate uncertainty introduced by the lack of a temperature measurement, CO concentration was calculated under two assumed temperature profiles (T_{eq} = 3570 K and 3070 K). Concentration uncertainty from this estimated temperature uncertainty is < 10% from ignition to the end of combustion given the low temperature sensitivity of the measurement.

In figure 3.9, an averaged WMS-$2f/1f$ measurement in the steady state region at two distinct pressures is compared to simulated signals using the WMS model discussed in section 3.4, assuming equilibrium temperature and floating mole fraction. A passband filter of 2 kHz was implemented with lock-in analysis of the harmonics (gray), whereafter 19 scans of the measurements during the steady state condition were also averaged (blue) to improve SNR. There are a few notable differences between the two measurements. SNR was ~ 7 and ~ 22 for the measurements at 1016 psi and 550 psi, as signal magnitude generally decreases with pressure as expected. Accordingly, the precision error is estimated to be ~ 15% and ~ 5%, respectively. Another apparent difference is shape. The WMS-$2f/1f$ signal at 550 psi shows a local maximum in both the up scan and down scan. By contrast, the WMS signal at 1016 psi does not reveal this feature primarily due to the extreme pressure broadening of the absorbance spectrum that diminishes this local peak. In either case, the model and measurement are consistent with the evolution of the signal shape and gives confidence in the broadening model.

The post-processing method described above was applied to data from different

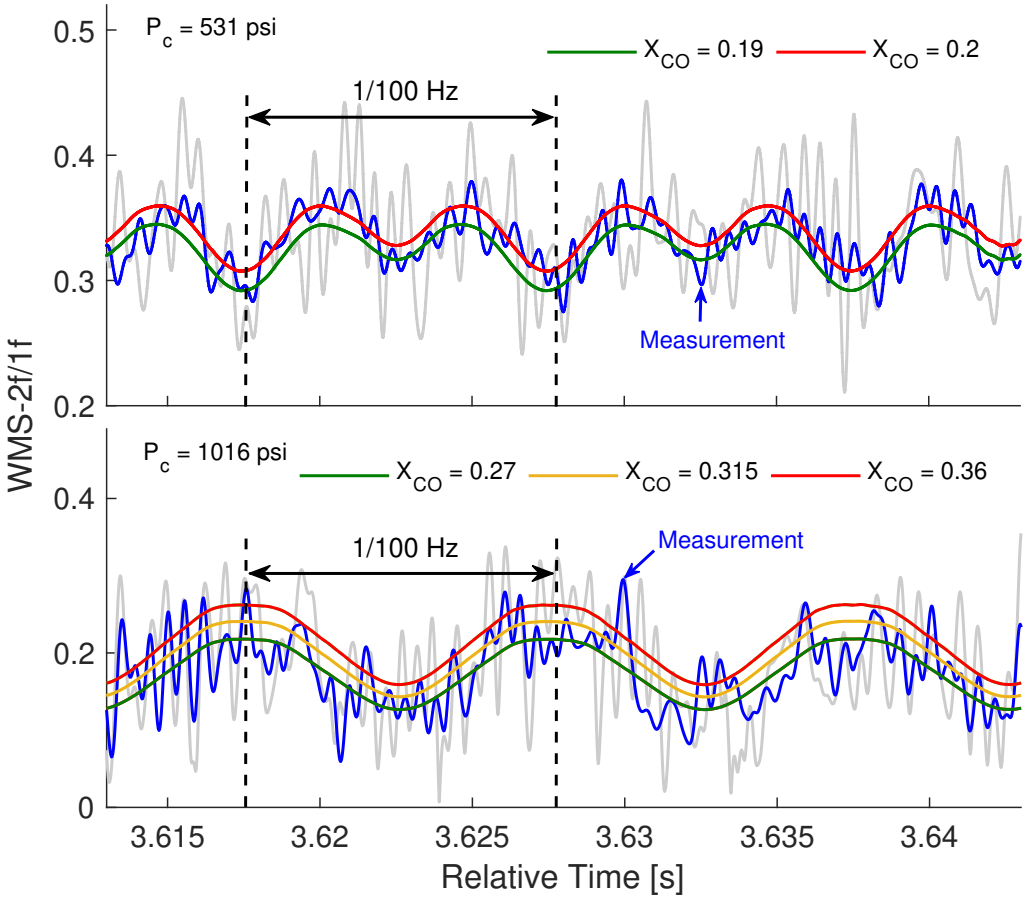

Figure 3.9: Measured WMS signal shown with simulated WMS signals at P = 531 psi, T = 3602 K and L = 2.54 cm (top) and measured WMS signal shown with simulated WMS signals at P = 1016 psi, T = 3674 K, and L = 2.54 cm (bottom)

test conditions to assess the level of agreement between the measurements in the steady state region and equilibrium conditions calculated via thermochemical analysis [NASA CEA]. Error bars are applied that combine the measurement noise with uncertainty related to temperature and spectroscopic model inputs via a simple sum of square errors. Typical uncertainties were ~10 to 15%. Figure 3.10 shows that the X_{CO} measurement agrees well with chemical equilibrium at most conditions, especially over 700 psi. There is greater disagreement, beyond the estimated measurement uncertainty, at lower pressures (< 550 psi) and this is suspected to be a consequence of the helium purge penetrating further into the

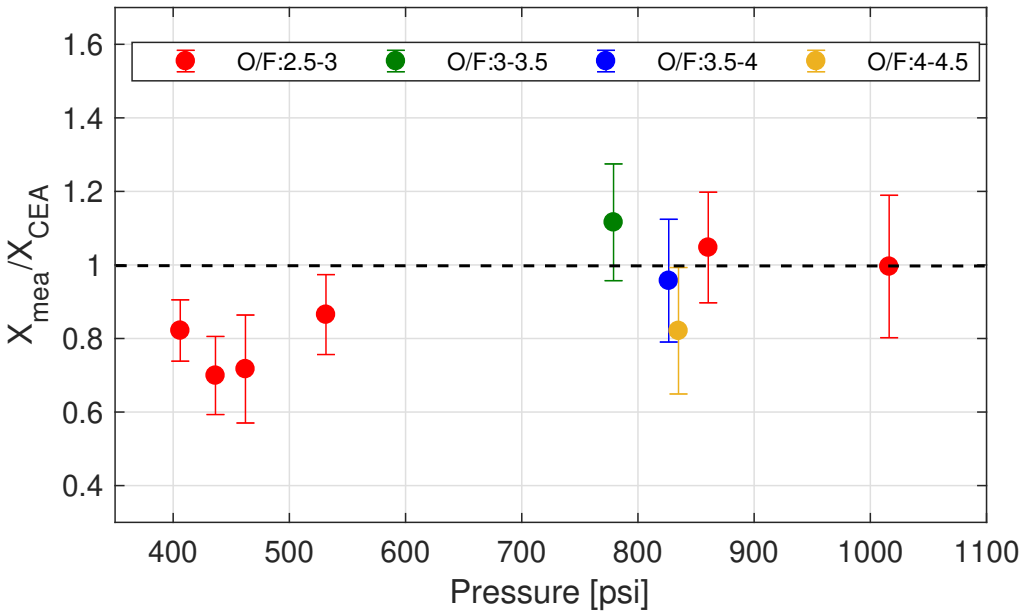

Figure 3.10: Measured CO mole fraction compared to equilibrium CO mole fraction over range of pressures and O/F ratios

chamber than intended and effectively decreasing the optical path-length along the line of sight. Future work in optimizing the purge system geometry may help minimize this effect.

3.7 Summary

A mid-infrared laser absorption sensor was developed for in situ measurements of nascent carbon monoxide at practical chamber conditions of hydrocarbon-fueled rockets. The sensor is enabled by novel wavelength selection in the CO fundamental band near 4.98 μm with strong differential absorption, low temperature sensitivity, and minimal interference. A scanned wavelength modulation spectroscopy technique, leveraging recent enhancements in tuning response of quantum cascade lasers, provided for quantitative signal recovery and interpretation despite large non-absorption raw signal losses, unavailable baseline signal caused by high collisional broadening, and noise associated with vibrations and

emission during facility operation. Time-resolved field measurements of CO mole fraction were successfully conducted at relevant pressures and oxidizer-to-fuel ratios on a kerosene-oxygen rocket combustor at the Air Force Research Laboratory in Edwards, CA. To the authors' knowledge, these data represent the first quantitative species measurements in a hydrocarbon-fueled rocket combustion chamber at realistic operating conditions (> 40 atm), and an extension in pressure range (up to 70 atm) for laser absorption combustion diagnostics more generally. The advantageous features of the CO sensing strategy provide for broad utility in high-pressure, fuel-rich combustion studies.

3.8 CO measurements at the bandhead near 2.3 μm

To infer temperature using a two-wavelength absorption technique, additional absorption region of CO at the bandhead near 2.3 μm have been selected by considering the following criteria: (1) strong differential absorption, (2) minimal interference with other combustion species, and (3) high temperature sensitivity. Figure 3.11 demonstrates an absorption simulation of the first overtone band of CO with other combustion species over a range of pressures. The features shows minimal interference and strong differential absorption, which is favorable for sensitive measurements.

Similar to lthe spectroscopic model designed for the fundamental band near 4.9 μm, the initial spectroscopic model for the first overtone band near 2.3 μm was developed assuming that the total spectral absorbance is equivalent to sum of all individual transitions (Voigt lineshape summation). A DFB diode laser with ~5 mW output power was utilized to probe the CO bandhead near 2.3 μm and characterized to implement a WMS technique, which mitigates environmental noise and improves the SNR of the measurement. The new sensor has been deployed on a single-element-injector rocket combustor along with the sensor developed for the absorption region near 4.9 μm. Consequently, the sensor was

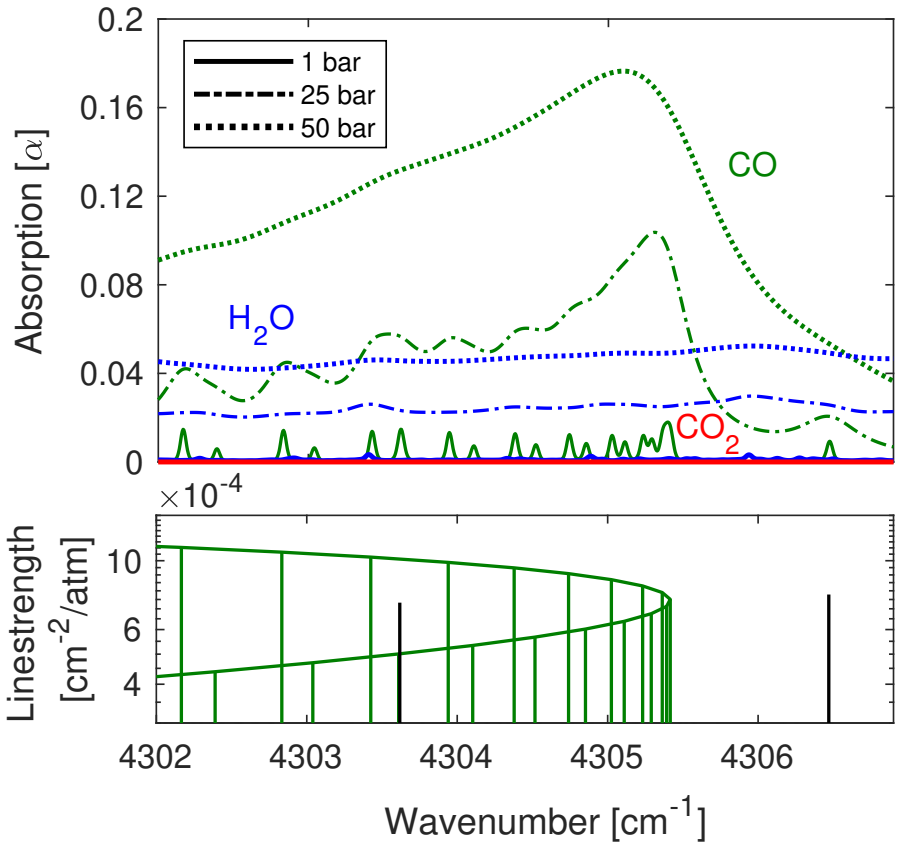

Figure 3.11: Target CO absorption spectra with pressure dependence and absorption line-strength (HITEMP: T = 3500 K, X_{CO} = 0.30, X_{CO_2} = 0.10, X_{H_2O} = 0.30)

tested in the combustion chamber over the same conditions presented in section 3.6, which include a pressure range of 25–70 atm and at oxidizer-to-fuel ratios ranging from 2.5–4.5. To collect data from both the fundamental and overtone bands simultaneously, additional optics including beam splitters, spectral filters (Spectrogon, 2320±20 nm), and InGaAs photodetectors have been integrated into the existing experimental setup shown in Fig. 3.7.

Measured raw optical signals at vibrational bandhead of CO near 2.3 μm were averaged over the steady state region and post-processed through a digital lock-in amplifier and 2 kHz passband filter to extract the WMS harmonic signals. Figure 3.12 compares an averaged WMS-$2f/1f$ measurement at the first overtone bandhead to simulated signals using the developed WMS model, assuming

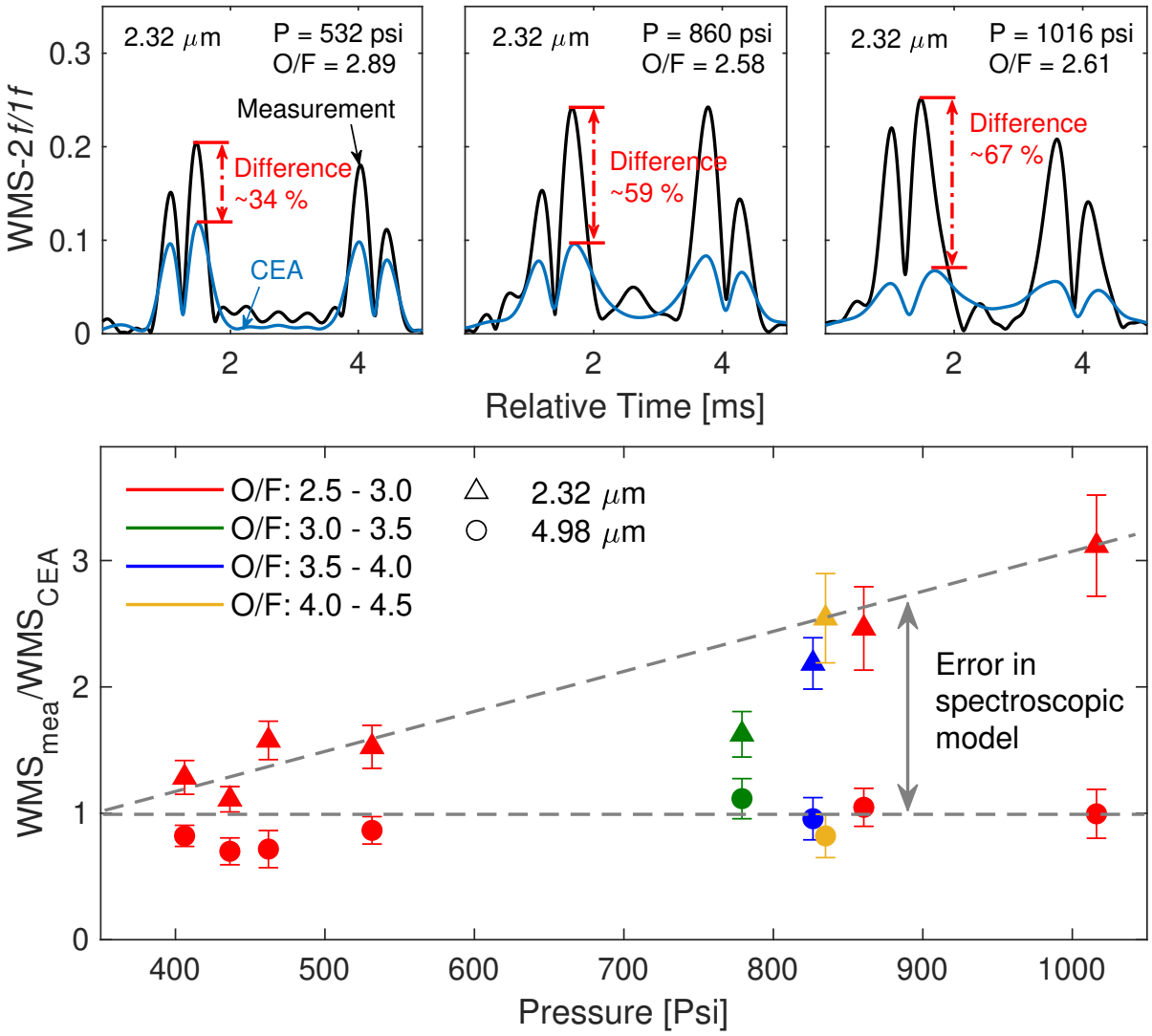

Figure 3.12: Measured WMS-$2f/1f$ signals with SNR compared to chemical equilibrium simulations for both 4.98 μm and 2.32 μm over relevant mixture ratios and pressures.

chemical equilibrium for mixture composition and temperature and the HITEMP database for spectral parameters. The measured WMS signal at 2.32 μm exhibited adequate signal quality over a range of pressures (up to 1016 psi). However, the measured and simulated WMS-$2f/1f$ signals demonstrated substantial disagreement in both magnitude and spectral, which amplified with increase in pressure. Such trend is shown in Fig. 3.12, using the ratio of the measured and simulated WMS-$2f/1f$ signals. The disagreement between the measured and simulated WMS-$2f/1f$ signals was deemed to be well beyond the typical uncertainties in

the simulation, indicating a fundamental error in the spectroscopic model assumptions. This was discovered to be a consequence of line-mixing effects (first introduced in section 2.4), which occur in spectrally-dense regions [61], such as the bandhead. A deeper investigation of line-mixing effects and novel sensing strategies exploiting these line-mixing effects to extend the pressure capability of LAS are presented in the following two chapters.

CHAPTER 4

Exploiting line-mixing effects for laser absorption spectroscopy at extreme combustion pressures

The contents of this chapter have been published in the journal ***Proceedings of the Combustion Institute*** *under the full title 'Exploiting line mixing effects for laser absorption spectroscopy at extreme combustion pressures' [45]. Portions of the chapter's content have also been presented at the* ***11th US National Combustion Meeting*** *[62] and* ***2020 AIAA Aerospace Sciences Meeting*** *[63].*

4.1 Introduction

Combustion at extreme pressures (> 50 atm) is of increasing significance as engine developers push the limits of power density, efficiency, and emissions suppression. Several ultra-clean piston-engine concepts are designed to operate at peak pressures in excess of 100 atm [10], while modern liquid-propellant rockets may have steady-state combustion chamber pressures above 200 atm. At these very high pressures, many of the underlying assumptions present in combustion modeling become less reliable and predictive capability for engineering design requires new understanding. To elucidate combustion physics at high-pressure conditions, controlled experiments coupled with comprehensive diagnostics are needed. Unfortunately, most state-of-the-art combustion diagnostics have been limited to much lower pressures (< 20 atm), prompting the need to develop new high-pressure diagnostic techniques suitable for interrogating the next generation of combustion systems.

Laser absorption spectroscopy (LAS) has been extensively utilized for non-intrusive in situ measurements of temperature and species in harsh combustion environments [42]. For small molecules ($n < 5$ atoms) at moderate pressures (< 10 atm), LAS techniques commonly target individual spectral lines or transitions, which can be resolved with narrow-band lasers and interpreted with a few spectroscopic parameters. However, at higher pressures, this line-specific analytical approach falters, largely due to collisional line broadening, which scales linearly with pressure. Collisional broadening leads to a blending of adjacent spectral lines that: (1) decreases differential absorption (i.e. difference in peak-to-valley absorption in a local spectral domain), (2) causes cross-species interference, and (3) complicates spectral modeling and interpretation. For LAS methods with limited spectral bandwidth, the reduction in differential absorption leads to an effective pressure limit in harsh environments, where non-absorption losses are typical and difficult to distinguish from molecular absorption without spectral structure.

While few quantitative species diagnostics have been demonstrated above 20 atm in practical combustion environments, some successes can be noted. Caswell et al. developed near-infrared sources with a wide spectral range to measure methane, water vapor, and temperature up to 30 atm in a gas turbine combustor [40]. Mattison et al. similarly probed the near-infrared water spectrum to achieve in-cylinder measurements up to 54 atm in a HCCI piston-engine [2]. In the mid-wave infrared, Goldenstein [1] and Spearrin et al. [37] performed LAS of H_2O and CO in a pulse detonation combustor (PDC) at pressures up to 50 atm, targeting the fundamental vibrational bands. More recently, we extended CO sensing to 70 atm in a rocket combustor using a similar mid-infrared approach [45]. For CO_2, LAS near 20 atm was performed in an entrained-flow coal gasifier, targeting the CO_2 spectra near 2.0 μm [29]. Themes of these prior works include leveraging advancements in more broadly tunable sources and carefully selecting molecules and spectral lines that have intrinsically low broadening.

This paper describes a new approach to high-pressure laser absorption sensing

that exploits the vibrational band narrowing effects of line mixing to significantly extend pressure capability. Line mixing relates to collision-induced changes in rotational energy that result in transfers of absorption intensity from weak to strong regions within a vibrational band. Line-mixing effects are pronounced in spectrally dense regions, where line spacing is small, such as bandheads. For CO and CO_2, the R-branch bandheads near 2.3 μm and 4.2 μm, respectively, become active at combustion temperatures, as shown in Fig. 4.1 and Fig. 4.2. While collisional line broadening diminishes the differential absorption of specific rovibrational transitions, line mixing counters this effect by narrowing and amplifying bandheads, which are comprised of many closely spaced lines. Here, we target the aforementioned bandheads for laser absorption sensing, investigate and characterize line-mixing effects on the local spectra over a range of high-pressure

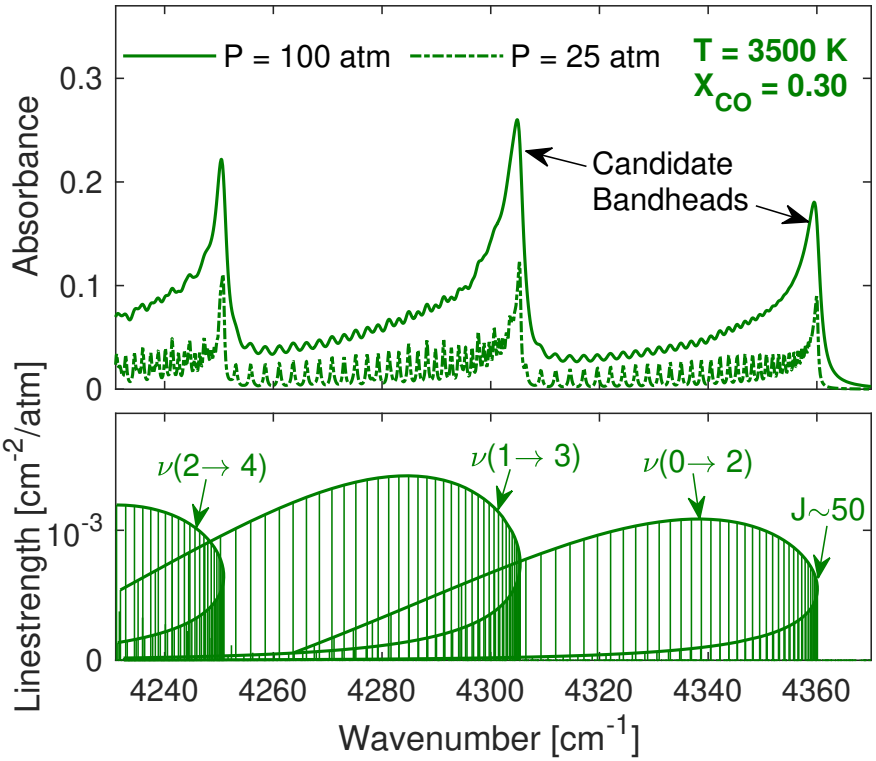

Figure 4.1: Simulated CO absorbance and linestrengths near 2.3 μm (excluding line-mixing effects) at representative high-temperature combustion conditions using the HITEMP spectral database [44]

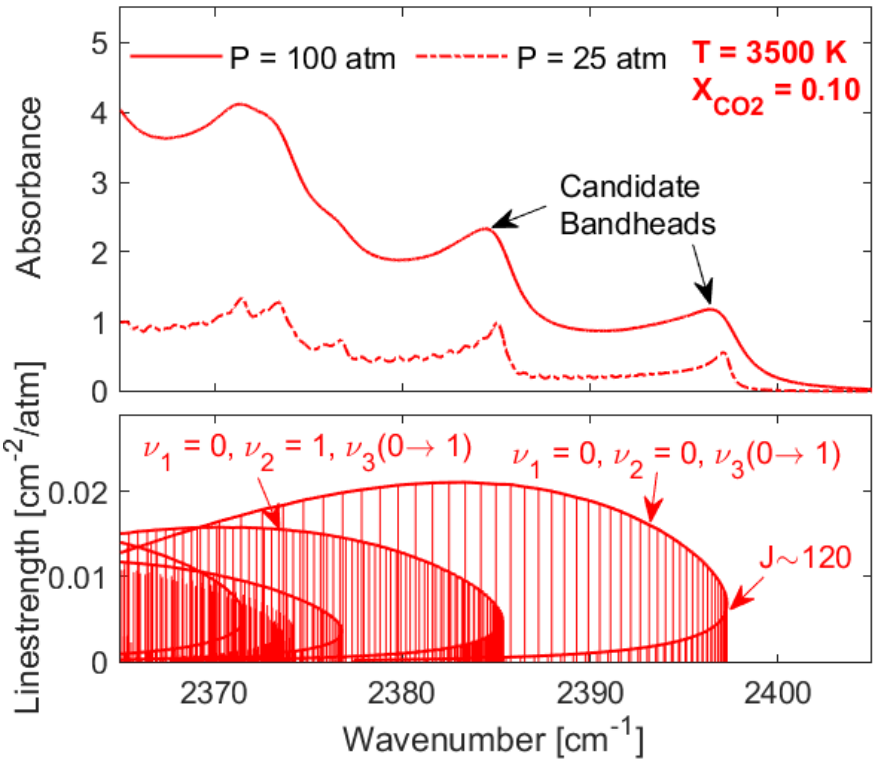

Figure 4.2: Simulated CO_2 absorbance and linestrengths near 4.2 μm (excluding line-mixing effects) at representative high-temperature combustion conditions using the HITEMP spectral database [44]

and high-temperature conditions, and demonstrate the pressure-capability of the method via quantitative species measurements in a sub-scale rocket combustor at pressures up to 104 atm.

4.2 Spectroscopic approach

4.2.1 Line-mixing theory

Spectral line mixing is often observed at high gas densities, where collision-induced changes in rotational energy distort the molecular spectra within a vibrational band. Generally, these collisional effects favor intensity exchanges from weak to strong absorption regions, resulting in a vibrational band narrowing effect and promoting larger differential absorption. This phenomenon is more prominent in

spectrally dense regions where line spacing is small, such as bandheads, which are shown in the linestrength plots of Fig. 4.1 and Fig. 4.2. A spectral bandhead is the result of vibrational and rotational energy coupling that yields decreasing line spacing in the R-branches of CO and CO_2 stretch bands. For these particular bands, the convergence and wrap-around of spectral lines is only observed at high temperatures, where high rotational energy states are populated. Fig. 4.1 and Fig. 4.2 illustrate the set of transitions that make up several CO and CO_2 bandheads near 2.3 μm and 4.2 μm, respectively. As discussed, line mixing is expected to amplify the bandhead peak intensity and enhance differential absorption at elevated pressures, rendering these features strategic candidates for LAS sensing in extreme combustion environments.

To model absorption and account for line-mixing effects, we implement a relaxation matrix formalism [64] to represent the state-to-state population transfer rates. A more rigorous theoretical discussion with modeling process details can be found in other papers from our research group [43, 65]; the steps are truncated here for brevity. For a monochromatic light source at frequency ν [cm^{-1}], the spectral absorbance, α_ν, through a gas medium can be described by the transmitted and incident light intensities, I_t and I_0, respectively, via the Beer-Lambert law. Absorbance can then be related to thermophysical flow properties using the following relationship:

$$\alpha_\nu = -\ln\left(\frac{I_t}{I_0}\right)_\nu = \frac{nL}{\pi}\,\mathrm{Im}(\mathbf{d}\cdot\mathbf{G}^{-1}\cdot\boldsymbol{\rho}\cdot\mathbf{d}) \tag{4.1}$$

where n [molec $\cdot$ cm^{-3}] is the total number density of the absorbing species, L [cm] is the optical path length, $\boldsymbol{\rho}$ is a diagonal matrix containing the lower state Boltzmann population fractions, and $\mathbf{d}$ $[cm^{-1}/(\text{molec}\cdot cm^{-2})]^{\frac{1}{2}}$ is a vector of transition amplitudes [66]. $\mathbf{G}$ is a complex matrix given as:

$$G = \nu\mathbf{I} - \boldsymbol{\nu}^0 - iP\mathbf{W} \tag{4.2}$$

I represents the identity matrix, $\boldsymbol{\nu}^0$ [cm^{-1}] is a diagonal matrix containing transition frequencies, P [atm] is pressure, and **W** [cm^{-1}/atm] is the relaxation matrix.

The relaxation matrix, **W**, contains all collisional influences on the spectral shape [67]. The real diagonal terms of **W** consist of the broadening coefficients, γ_J [cm^{-1}/atm], and the imaginary diagonal terms are the pressure shift coefficients, $\Delta\nu_J^0$ [cm^{-1}/atm]. The real off-diagonal terms are proportional to the state-to-state population transfer rates, $R_{J\to K}$ [cm^{-1}/atm], from initial rotational energy level J to the final rotational energy level K and the imaginary off-diagonal components of **W** describe contributions from rovibrational dephasing [68]. It is important to note that broadening coefficients can be expressed in terms of the state-to-state population transfer rates (R) that describe line-mixing effects [61]:

$$\gamma_J = \frac{1}{2}\left[\sum_{J''\neq K''} R_{J''\to K''} + \sum_{J'\neq K'} R_{J'\to K'}\right] \tag{4.3}$$

Here, prime ($'$) and double prime ($''$) refer to the upper and lower states.

In this work, the real off-diagonal elements of **W** were modeled using the following modified-exponential-gap (MEG) law [69, 70]:

$$W_{JK} = a_1(T)\left[\frac{1+a_4\left(\frac{E_J''}{a_2 k_B T}\right)}{1+a_4\left(\frac{E_J''}{k_B T}\right)}\right]^2 \times \exp\left[\frac{-a_3\left(E_K''-E_J''\right)}{k_B T}\right] \tag{4.4}$$

Here, E'' [cm^{-1}] is the lower state energy of the transition and a_i are empirical MEG law coefficients. Methods for obtaining these coefficients are briefly discussed in Sec. 4.2.2, with more detailed discussions in [43, 65]. It is important to note that the temperature dependence of the real off-diagonal components is captured through $a_1(T)$, which follows the power law, analogous to broadening coefficient. To fully complete the relaxation matrix, the upward and downward population

transfer rates are related through the detailed-balance principle [71]:

$$\rho_J R_{J\to K} = \rho_K R_{K\to J} \tag{4.5}$$

This indicates that line mixing induces a vibrational band narrowing effect by favoring population transfers from weak transitions to strong transitions, supporting physical observations of the spectral structure.

Notably, when multiple collision partners are present, the full relaxation matrix can be expressed as a mixture-weighted summation of the individual perturber contributions:

$$\mathbf{W} = \sum_B X_B \mathbf{W}_{A-B} \tag{4.6}$$

With $\mathbf{W}$ fully defined, the simulated spectra, incorporating line-mixing effects, can now be scaled over a range of temperatures and pressures.

4.2.2 Spectral modeling

To characterize line-mixing effects in the CO and CO_2 bandheads, high-temperature and high-pressure experiments were conducted utilizing a high-enthalpy shock tube facility at UCLA. Scanned-wavelength direct absorption measurements of CO near 2.3 μm were obtained at pressures and temperatures ranging from 5–25 atm and 2000–4000 K, respectively, using pure CO gas. CO_2 measurements near 4.2 μm were conducted at pressures ranging from 20–60 atm and a slightly lower temperature range of 2000–3000 K, to minimize dissociation. Shock tube experiments for CO_2 were carried out in an argon (Ar) bath gas to minimize non-ideal gas dynamics (e.g. boundary layers) and provide greater experimental control over thermodynamic conditions.

In order to describe collision-induced population transfer rates, the modified-exponential gap law given in Eq. 4.4 was incorporated into the absorbance modeling framework. Species-specific MEG law coefficients, a_i, were obtained by

least-squares fitting the high-pressure absorbance data from the shock tube facility with the absorbance model, given by Eq. 4.1. This procedure was carried out for both CO and CO_2 over the range of thermodynamic conditions aforementioned to capture the temperature and pressure dependence of the relaxation matrix. The measured species-specific MEG law coefficients can be found in Table 4.1, while the collisional broadening coefficients can be found in separate works [65, 43]. It should be noted that collisional broadening and line mixing contributions are separated in the relaxation matrix formalism. To obtain collisional broadening coefficients and their respective temperature dependencies, shock tube experiments were conducted at low pressures (< 2.5 atm), where individual spectral transitions are distinct and contributions due to line mixing are negligible. These broadening coefficients are then implemented in the absorbance modeling framework to study line-mixing at higher-pressures, wherein the off-diagonal elements of the relaxation matrix, related to mixing rates, can be determined. Figure 4.3 highlights the pressure scalability of the updated absorbance model accounting for line-mixing effects. Notably, the line-mixing model exhibits excellent agreement with the measured CO and CO_2 spectra over a range of pressures. Additionally, Fig. 4.3 illustrates that without line mixing, the simulated spectra poorly represents the measured absorbance near the bandhead, where most of the population transfers occur. The simulated spectra with no line-mixing effects was modeled as a sum of Voigt profiles using the HITEMP spectral database [44] with updated self-broadening coefficients for CO [43] and Ar-broadening coefficients for CO_2

Table 4.1: MEG law parameters used in this work

	a_1 [10^{-3} $cm^{-1}atm^{-1}$]	a_2	a_3	a_4
CO-CO	1.52 ± 0.16[a]	0.51 ± 0.05	5.21 ± 0.10	2
CO_2-Ar	53.94 ± 2.49[b]	4.98 ± 0.25	3.19 ± 0.13	2

[a] T_{ref} = 1500 K with power-law exponent of 1.28 ± 0.06 [43]
[b] T_{ref} = 1200 K with power-law exponent of 2.06 ± 0.07 [65]

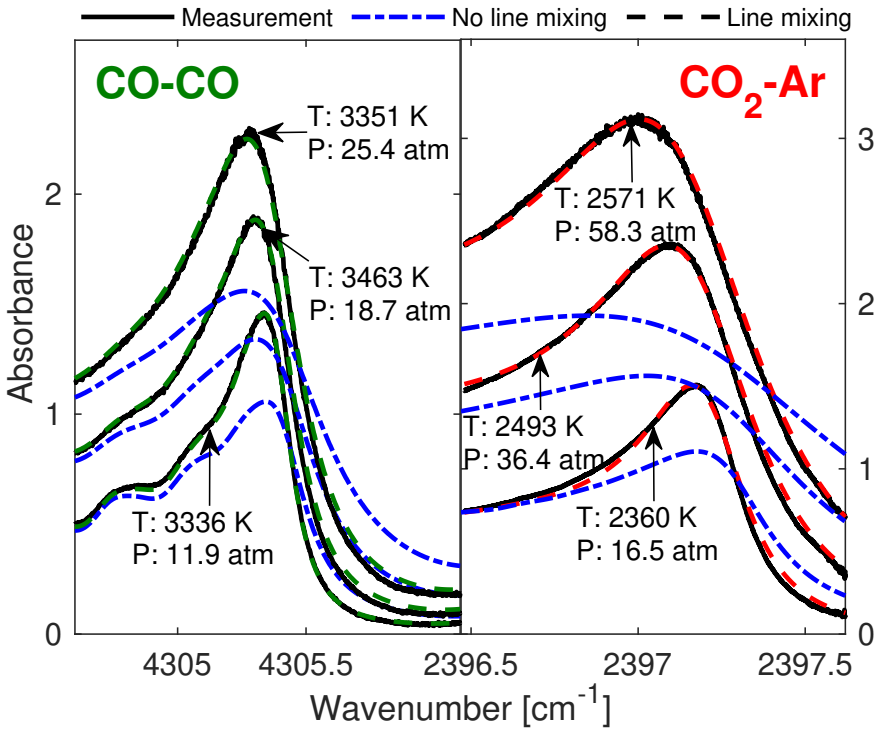

Figure 4.3: Measured spectral absorbance for (*left*) CO-CO and (*right*) CO_2-Ar compared to the developed MEG model used to capture line-mixing effects over a range of pressures

[65].

In order to extend the spectral line mixing models for CO and CO_2 developed in the shock tube to rocket combustion environments, additional assumptions are required to account for the dependence of the relaxation matrix on mixture composition. Namely, this involves scaling arguments that relate collisional line broadening coefficients and the population transfer rates for various perturbing species. Species-specific broadening coefficients, which are assigned to the real diagonal components of the relaxation matrices, are found in the literature for H_2O, CO_2, CO, and O_2 perturbers [57, 72]. This accounts for > 80% of a typical rocket combustion gas mixture, the remainder of which is assumed to be N_2. The population transfer rates, related to the real off-diagonal elements of the species-specific relaxation matrices, are obtained by scaling the measured rates (CO-CO and CO_2-Ar) by the ratio of broadening coefficients for each perturber (H_2O, CO_2,

CO, O_2), as shown in Eq. 4.7 and Eq. 4.8. The basis for this assumption is the sum rule (Eq. 4.3) that indicates that broadening coefficients scale similarly to the population transfer rates.

$$\mathbf{W}_{\mathrm{CO}-mix} = \sum_{B} X_B \mathbf{W}_{\mathrm{CO}-\mathrm{CO}} \left(\frac{\gamma_{\mathrm{CO}-B}}{\gamma_{\mathrm{CO}-\mathrm{CO}}} \right) \tag{4.7}$$

$$\mathbf{W}_{\mathrm{CO_2}-mix} = \sum_{B} X_B \mathbf{W}_{\mathrm{CO_2}-\mathrm{Ar}} \left(\frac{\gamma_{\mathrm{CO_2}-B}}{\gamma_{\mathrm{CO_2}-\mathrm{Ar}}} \right) \tag{4.8}$$

Recall the collisional broadening coefficients and population transfer rates that comprise $\mathbf{W}_{\mathrm{CO}-\mathrm{CO}}$ and $\mathbf{W}_{\mathrm{CO_2}-\mathrm{Ar}}$ have been measured experimentally [65, 43]. For the sensing application discussed herein, chemical equilibrium is assumed to dictate mixture composition at a given operating condition for the purposes of weighting broadening coefficients and mixing parameters in Eq. 4.7 and Eq. 4.8. These modeling adjustments provide a basis for high-pressure spectral interpretation of LAS measurements in various combustion environments.

4.3 Sensor design

4.3.1 Optical interface

Figure 4.4 illustrates a simplified optomechanical configuration representing the hardware interface for LAS on the target sub-scale liquid-propellant rocket combustor. For brevity, a thorough description of the experimental setup can be found in additional works by the authors [45, 73]; however, details pertaining to the line-mixing sensing strategy are discussed herein. To target the CO and CO_2 bandheads, a distributed-feedback (DFB) diode laser with ~10 mW output power was centered near 2322 nm and an interband cascade laser (ICL) with ~5 mW output power was centered near 4173 nm, respectively. For two-color thermometry measurements, an additional DFB quantum cascade laser (QCL)

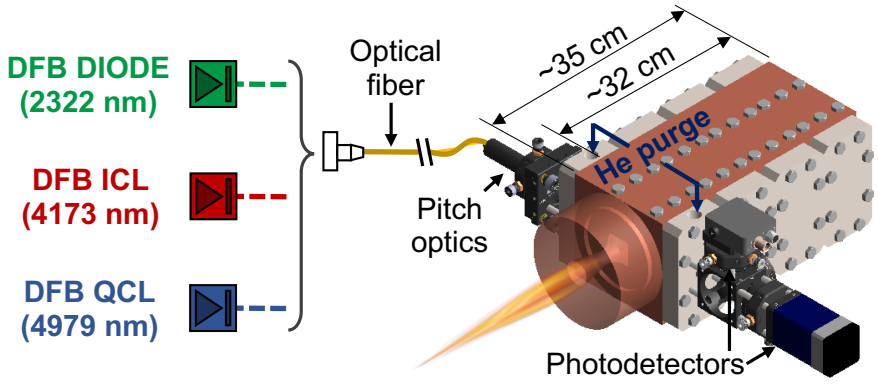

Figure 4.4: Optical interface with rocket combustor, including a graphical depiction of remote-light delivery and collection optics, for high-pressure CO and CO_2 measurements

with ~50 mW output power is employed to probe the fundamental CO absorption band near 4979 nm [45, 73].

An inherent challenge presented by this approach is the wavelength-specific nature of many optical components (e.g. detectors, fibers) that potentially increases sensor complexity to pitch and collect multiplexed light at very different wavelengths. To reconcile this, the incident light is combined and focused into a hollow-core fiber with broad transmissivity for remote light delivery [60, 74]. The fiber output is then re-collimated and transmitted across the combustion chamber through two wedged sapphire windows over a 2.5 cm transverse optical path length. A beam splitter is installed to separate the transmitted light so that each beam can be spectrally filtered for its respective wavelength before being collected on separate thermoelectrically-cooled photodetectors. An InGaAs photodetector (Thorlabs PDA10D) with a 15 MHz bandwidth is utilized for 2.3 μm light and a MCT photovoltaic detector (Vigo PVI-4TE-5-1) with a 10 MHz bandwidth is utilized for 4.2 μm and 5.0 μm light.

Measurements were conducted ~32 cm downstream of the single-element-injector, where complete combustion/mixing is most likely to occur. Raw detector data were collected at a sample rate of 10 MHz for 5-s intervals with hot-fires spanning 2–3 s in duration. Due to hardware limitations, experiments were

limited to two light sources per test. Therefore, hot-fires were conducted twice for each condition, alternating between the ICL targeting the CO_2 bandhead and the QCL targeting the CO fundamental band. The steady-state pressure trace and laser absorption signals for subsequent hot-fire tests targeting the same condition typically agreed within 2%, or within measurement uncertainty, suggesting reasonable repeatability of experiments.

4.3.2 Laser tuning parameters

Scanned-wavelength modulation spectroscopy with second harmonic ($2f$) normalized detection was implemented for all rocket combustor measurements in order to minimize dynamic non-absorption-related light intensity distortion. The $1f$ normalized-WMS-$2f$, with background subtraction, provides a well-established technique to extract signals strongly related to differential absorption while rejecting noise associated with beam steering, scattering, and thermal emission [55]. Measurements are conducted by superimposing a fast sine-wave modulation on a slow sine-wave scan from which the harmonic components are extracted using digital lock-in amplification and frequency filtering. Within the framework of scanned-WMS, the scan depth, a_s, modulation depth, a_m, and associated frequencies, f_s and f_m, can be adjusted to optimize signal quality. Additionally, the center wavelength of each laser was slightly adjusted (< 0.07 nm) across different combustor conditions to account for pressure shift in the spectra and maximize the WMS signal. The parameters for each laser are listed in Table 4.2 and were selected as a compromise between WMS-$2f$ signal quality (SNR) and effective measurement rate. Further details on the parametric optimization strategy can be found in [45, 73].

In probing high-pressure spectra, rapidly tunable distributed feedback lasers are often unable to resolve differential absorption within achievable modulation depths due to collisional broadening and blending of adjacent features. Con-

Table 4.2: Laser scan and modulation parameters

ν [nm]	a_s [cm^{-1}]	f_s [Hz]	a_m [cm^{-1}]	f_m [kHz]
2322	2.55	100	0.48	50
4173	0.63	100	0.36	20
4979	0.13	100	0.50	20

sequently, a common desire is to increase spectral bandwidth with broadband sources. In this work, the band narrowing effects of line mixing are shown, via spectral simulation, to increase differential absorption by up to a factor of ten within the narrow tuning range of the selected sources, suggesting persistently strong harmonic signals with increasing pressure at the somewhat modest scan and modulation depths shown in Table 4.2. To prove capability, experiments were performed in a high-pressure combustor.

4.4 Experimental results

4.4.1 Thermochemistry measurements

A series of field measurements were conducted over a range of pressures and propellant mixture ratios (MR) from 25–104 atm and 2.2–4.6, respectively, on a single-element-injector rocket combustor with CH_4/GOx and RP-2/GOx propellant combinations. The test facility is located at the Air Force Research Laboratory on Edwards Air Force Base, CA USA. Fig. 4.5 shows a representative hot-fire test including time-resolved measurements of pressure and the corresponding WMS-$2f/1f$ signals at 4.2 μm, 2.3 μm, and 5.0 μm for a steady-state chamber condition of 27.4 atm and MR of 2.33. An abrupt increase in all WMS-$2f/1f$ signals was observed around 1.3 s, corresponding to the introduction of propellants and ignition.

For all three wavelengths, the raw optical signal was averaged over the steady-state region to improve signal-to-noise ratio (SNR) and was processed through a

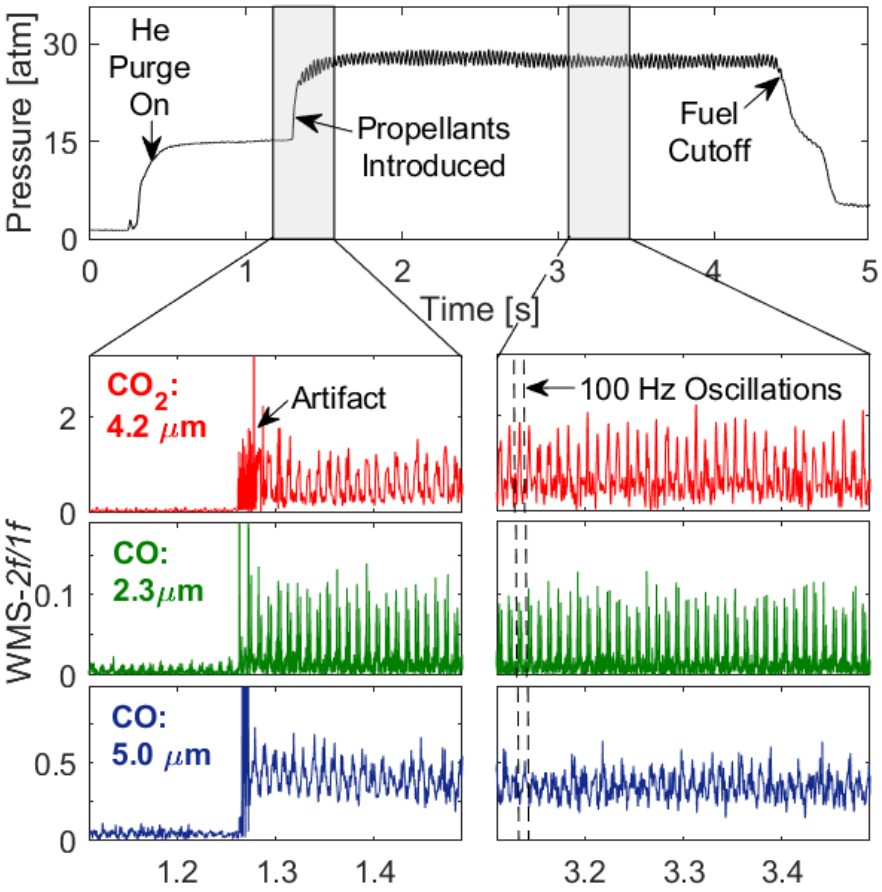

Figure 4.5: Time evolution of chamber pressure for a representative test and the corresponding WMS-$2f/1f$ signals (background subtracted) for CO_2 near 4.2 μm and CO near 2.3 μm and 5.0 μm

digital lock-in amplifier to extract the WMS harmonics, from which species and temperature can be inferred. Fig. 4.6 and Fig. 4.7 compare the measured WMS-$2f/1f$ signals targeting the CO and CO_2 bandheads, respectively, to simulated WMS-$2f/1f$ signals with and without the updated line-mixing model discussed in Sec. 4.2.2. Notably, the CO measurements exhibit favorable SNR at pressures up to 104 atm and the CO_2 measurements exhibit similar signal quality up to 82 atm, the highest respective pressures tested for either sensor. Notably, the divergence between the models with and without line-mixing effects increases with pressure.

The best-fit WMS signals using the refined spectral model were used to quantitatively infer mole fraction and temperature. The ratio of peak WMS signals

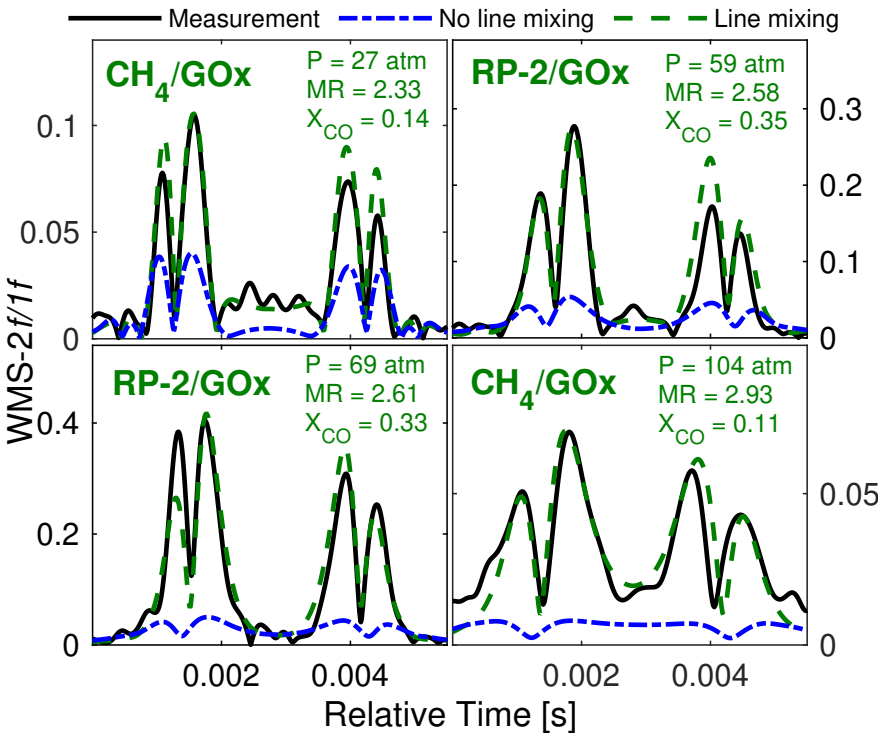

Figure 4.6: Measured WMS-$2f/1f$ signals targeting CO compared to simulated WMS-$2f/1f$ signals with and without the updated line-mixing model over a range of mixture ratios and pressures

from 2.3 μm and 5.0 μm was utilized to first obtain temperature, which was then used to infer CO and CO_2 concentration based on absolute signal magnitude [59, 45]. Figure 4.8 compares the measured temperatures and mole fractions to chemical equilibrium solver (NASA CEA) predictions [75] for RP-2/GOx, which can be used to assess combustion progress. The chemical equilibrium results are bound by the highest and lowest pressures measured, respectively. In order to obtain mole fraction measurements above 70 atm, where the SNR of the CO fundamental band measurements was deemed too low, CEA temperature was assumed. The inferred temperatures from all tests followed the expected trends, but were slightly lower (generally by 100–300 K) than equilibrium temperature, typical of incomplete combustion, poor mixing, heat losses, or a cold boundary layer. Temperature and multi-species measurements can be used to evaluate overall combustor performance/efficiency and anchor to computational models

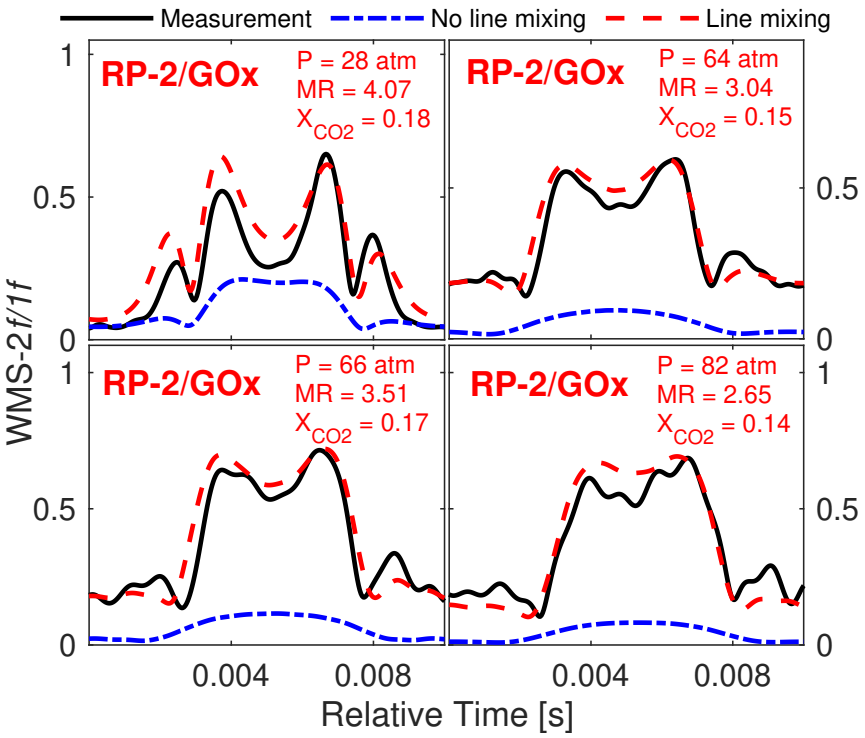

Figure 4.7: Measured WMS-$2f/1f$ signals targeting CO_2 compared to simulated WMS-$2f/1f$ signals with and without the updated line-mixing model over a range of mixture ratios and pressures

that inform engine design.

4.4.2 Measurement Uncertainty

In this paper, we follow the Taylor series method (TSM) of uncertainty propagation [76]. The main factors considered in calculating the uncertainties in the measured temperatures and mole fractions include: (1) uncertainty in pressure measurements, (2) uncertainty in the spectroscopic model related to composition-dependent collisional broadening and mixture ratio (MR), and (3) mechanical noise induced from the harsh combustion environment. For the uncertainty in mole fraction, the temperature uncertainty has been considered in addition to the aforementioned contributors since concentration inference requires a temperature input. The total temperature uncertainty was estimated to be 8–11% for all ex-

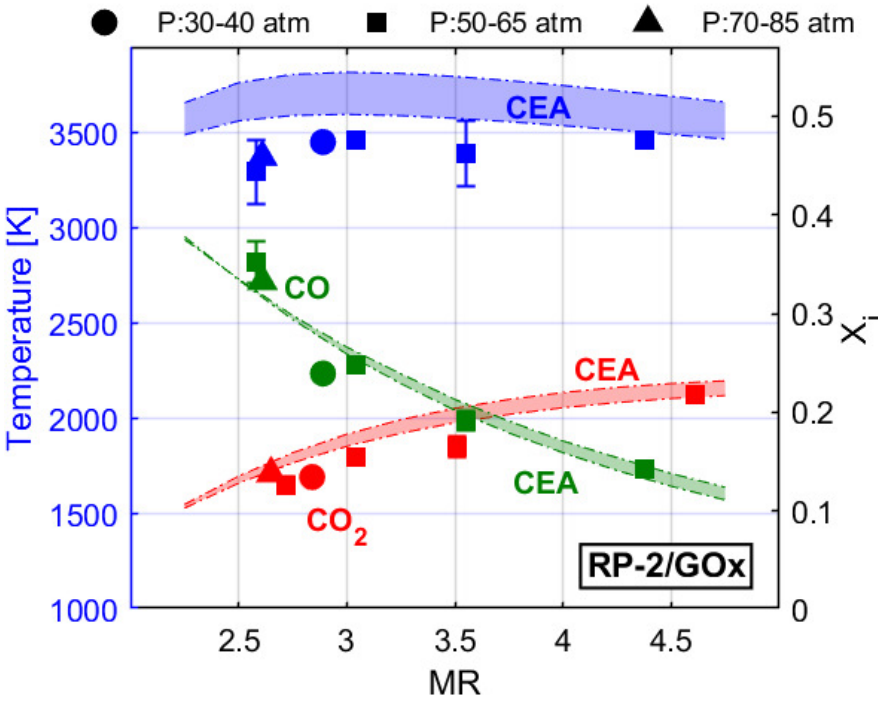

Figure 4.8: Temperature and species measurements with representative error bars at steady-state combustor conditions compared to NASA CEA predictions over a range of mixture ratios and pressures for kerosene and oxygen

periments and both CO and CO_2 mole fraction uncertainties were approximately 10–13%, with the largest uncertainty corresponding to the highest pressure. In order to improve these values for future studies, refinement of the spectroscopic models and further noise mitigation is necessary. Despite this, the mole fraction measurements are consistent with total carbon conservation and both temperature and species trend with the anticipated values from chemical equilibrium over the range of mixture ratios tested. More details regarding uncertainty analysis can be found in Appendix A.

4.5 Conclusion

A novel laser absorption sensing strategy was developed for quantitative measurements of CO and CO_2 at high combustion pressures (P > 50 atm). The technique

exploits the vibrational band narrowing effects of line mixing, which acutely amplify differential absorption at bandheads, and counter the effects of collisional line broadening. In this work, the CO and CO_2 R-branch bandheads near 2.3 μm and 4.2 μm, respectively, are strategically targeted to extend the pressure-range capability of in situ sensing of gas properties in combustion environments using relatively narrow-band light sources. Field measurements were conducted over a range of high pressures in a sub-scale rocket combustor operated with kerosene and supercritical methane. In order to quantitatively interpret the measured WMS-$2f/1f$ signals, spectral line-mixing models were developed for each bandhead utilizing a high-enthalpy shock tube facility. The refined spectroscopic models employ a modified-exponential gap law to thermodynamically scale line-mixing effects, which enabled quantitative inference of temperature, CO, and CO_2 in the liquid-propellant rocket combustor. To the authors' knowledge this work represents significant extensions in demonstrated pressure capability, to 104 atm and 82 atm, respectively, for in situ CO and CO_2 species measurements in practical combustion devices. More importantly, the enhanced pressure capability enabled by the novel spectroscopic strategy provides for a valuable new tool to experimentally investigate and engineer the next generation of high-pressure combustion systems.

4.6 Uncertainty Analysis

The uncertainty analysis presented here largely follows that of Nair et al. [77]. The uncertainties in temperature and mole fraction of species A were calculated using Eq. 4.9 and Eq. 4.10, which account for the uncertainty factors described in Sec. 4.4.2.

$$(\Delta T)^2 = (\Delta T_{\Delta P})^2 + (\Delta T_{\text{Spec.}})^2 + (\Delta T_{\text{SNR}})^2 \tag{4.9}$$

$$(\Delta X_A)^2 = (\Delta X_{A,\Delta P})^2 + (\Delta X_{A,\text{Spec.}})^2 + (\Delta X_{A,\text{SNR}})^2 + (\Delta X_{\text{A},\Delta T})^2 \tag{4.10}$$

Figure 4.9 presents the visual summary of the uncertainties for each variable along with contributions from the various dependent variables. Typically, the uncertainties in the spectroscopic model and the environmental noise were the largest contributors. Mole fraction of CO_2 was most susceptible to the temperature uncertainty. The pressure uncertainty was taken from the difference between the measured pressure variations and the mean pressure during the test. The inverse of the SNR from each test was used to estimate uncertainty due to mechanical noise. In order to estimate the spectroscopic model uncertainty, we define a mixture-weighted broadening coefficient, $\gamma_{\text{A-mix}}(T)$, as:

$$\gamma_{A-\text{mix}}(T) = \sum_B X_B(\gamma_{A-B}(T)) \tag{4.11}$$

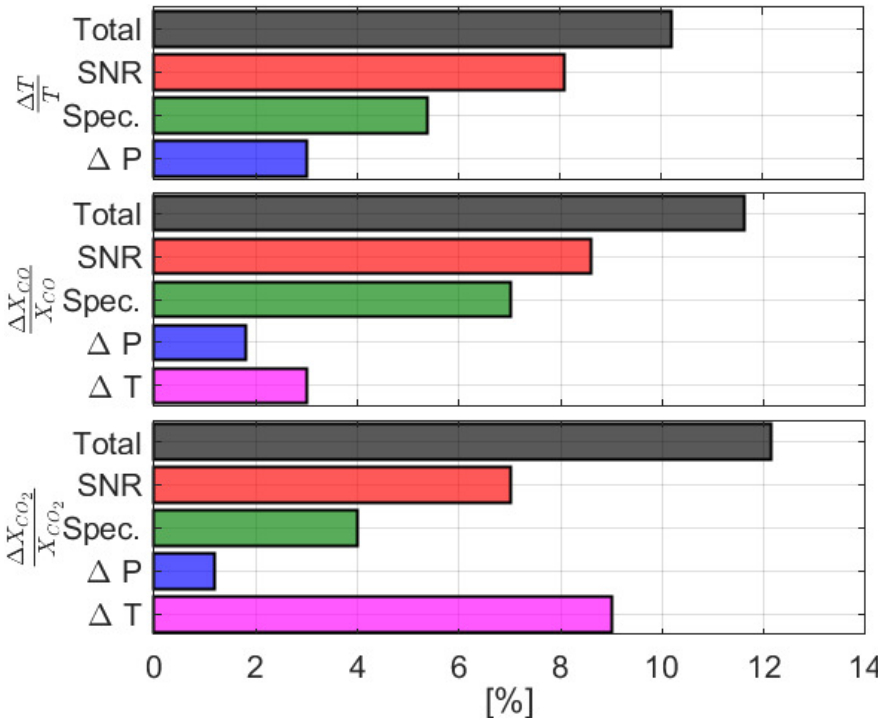

Figure 4.9: Representative uncertainties for temperature, T, CO mole fraction, X_{CO}, and CO_2 mole fraction, X_{CO_2}, for a hot-fire test at P = 56 atm and MR = 3.5

Per Eq. 4.7 and Eq. 4.8, the uncertainty in the spectroscopic model strongly depends on the uncertainty in the scaling factor, which is the ratio between $\gamma_{A-\text{mix}}(T)$ and broadening coefficients, $\gamma_{\text{CO}-\text{CO}}$ and $\gamma_{\text{CO}_2-\text{Ar}}$. The uncertainty of the mixture-weighted broadening coefficient, $\Delta\gamma_{A-\text{mix}}(T)$, is attributed to the uncertainty in the broadening coefficients of individual perturbers, $\Delta\gamma_{A-B}(T)$, and the uncertainty in local equivalence ratio, $\Delta\phi$, (which determines composition) as shown in Eq. 4.12.

$$(\Delta\gamma_{A-\text{mix}}(T))^2 = \sum_B [(\gamma_{A-B}(T)\Delta X_B)^2 + (X_B\Delta\gamma_{A-B}(T))^2] \tag{4.12}$$

The mole fractions of the collision partners, X_B, were calculated from NASA CEA [75] and the uncertainty, ΔX_B, was estimated based on the uncertainty in local equivalence ratio:

$$(\Delta X_B)^2 = \left(\frac{\partial X_B}{\partial\phi}\Delta\phi\right)^2 \tag{4.13}$$

The uncertainty in the temperature-dependent collisional broadening coefficient, $\Delta\gamma_{A-B}(T)$, for species A with collision partner B is calculated as follows:

$$(\frac{\Delta\gamma_{A-B}(T)}{\gamma_{A-B}(T)})^2 = (\frac{\Delta\gamma_{A-B}(T_0)}{\gamma_{A-B}(T_0)})^2 + N_B^2(\frac{\Delta T}{T})^2 + [\ln\left(\frac{T_0}{T}\right)\Delta N_B]^2 \tag{4.14}$$

The uncertainties in collisional broadening coefficient, $\Delta\gamma_{A-B}$, at reference temperature, T_0, and temperature-dependent exponent, ΔN_B, were taken from literature [57, 72, 43]. The uncertainties in $\gamma_{\text{CO}-\text{CO}}$ and $\gamma_{\text{CO}_2-\text{Ar}}$ were determined from prior works by the authors [43, 65].

4.7 Additional related studies

4.7.1 CO_2 measurements vs Chemical equilibrium

More CO_2 measurements were conducted on a coaxial single-element-injector rocket combustor at the Air Force Research Laboratory (Edwards, CA). A series

of measurements were conducted over a range of pressures and mixture ratios (MR) from 28–83 bar and 2.3–4.6, respectively, with RP-2 (kerosene) and gaseous oxygen as propellants. The combustion chamber is comprised of stackable modular sections, with optical access located at the furthest downstream axial location, where chemical equilibrium was most likely to be achieved. In this work, all measurements have been compared to expected chemical equilibrium, calculated using NASA CEA [78].

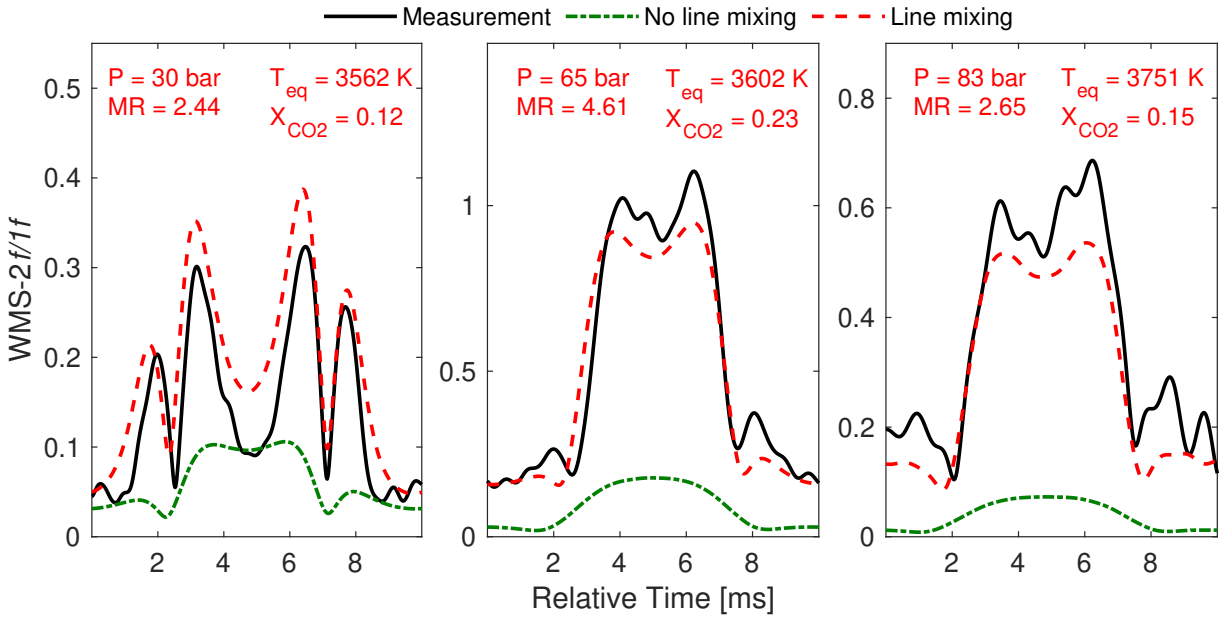

Figure 4.10: Measured WMS-$2f/1f$ signals for an averaged single scan period compared to simulated signals with and without the line mixing model for three test conditions of RP-2/GOx

In order to improve SNR, the raw optical signal was averaged over the steady-state region of approximately 1 second and post-processed though a digital lock-in amplifier to extract WMS harmonics. Figure 4.10 compares the averaged WMS-$2f/1f$ measurements to simulated WMS-$2f/1f$ signals with and without the developed line-mixing model at different pressures and mixture ratios. Notably, the CO_2 measurements exhibit high SNR at pressures up to 83 bar, indicating a potential to conduct measurements at even higher pressures. The line-mixing model shows reasonable agreement with the measurements regarding the spec-

tral structure for all three test conditions shown. In contrast, simulations not accounting for line-mixing effects demonstrate large disagreement with the measurement data in both magnitude and spectral shape. The updated model enables quantitative inference of species concentration from the measured WMS signals

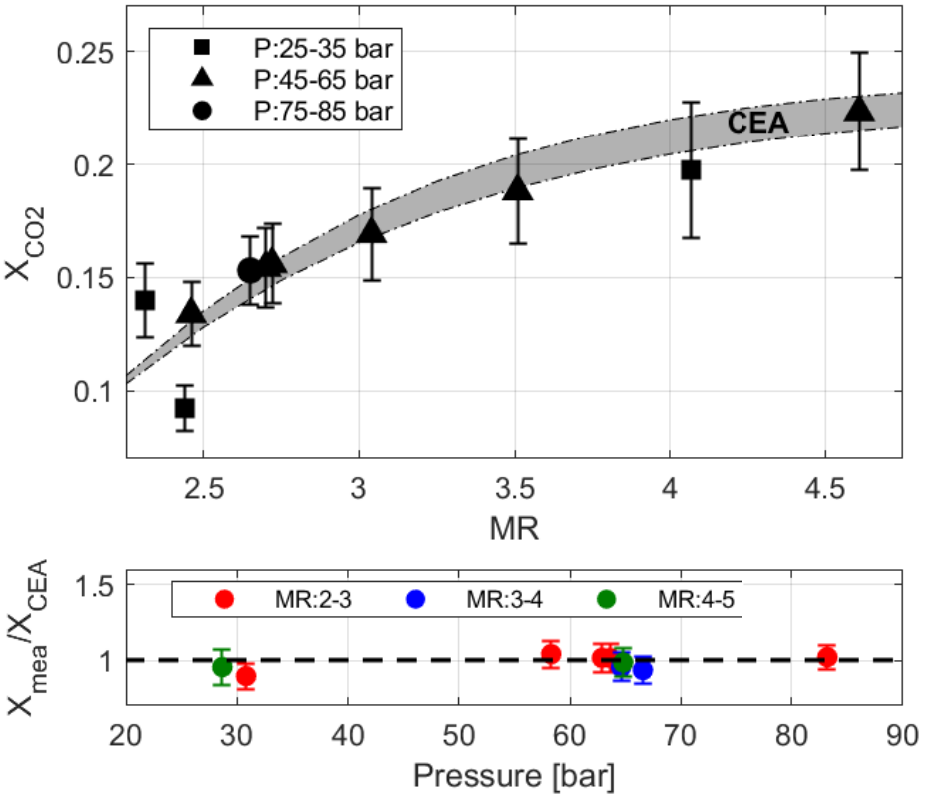

Figure 4.11: CO_2 mole fraction measurements with representative error bars at steady-state combustor conditions compared to CEA over a range of mixture ratios and pressures for RP-2/GOx

Figure 4.11 compares inferred mole fraction to chemical equilibrium expectations for RP-2/GOx. The CEA results are bounded by the highest and lowest pressures measured, 83 bar and 28 bar, respectively, and shown for reference. Previous measurements on the rocket combustor with RP-2/GOx demonstrated generally 100–300 K lower temperature than equilibrium temperature, potentially due to poor mixing, heat losses, or a cold boundary layer [43]. Species uncertainties (as shown by error bars) were calculated with an assumed temperature uncertainty of 200 K, yielding a typical uncertainty of 9%. Notably, the inferred

CO_2 mole fraction from all tests followed the expected trends and agreed well with equilibrium expectations.

4.7.2 Measurements exploiting line mixing effects in the $(01^10 \rightarrow 01^11)$ fundamental bandhead of CO_2 near 4.2 μm

Additional CO_2 vibrational bandhead near 4.2 μm have been selected for species measurements by considering the following criteria: (1) strong differential absorption, and (2) minimal interference with other combustion species. Figure 4.12 illustrates the absorption simulation (neglecting line mixing) of the vibrational bandhead with other combustion species over a range of pressures. The features present minimal interference and strong differential absorption, which is expected to further amplify at high-pressure rocket combustion conditions due to the band narrowing effects induced from line mixing.

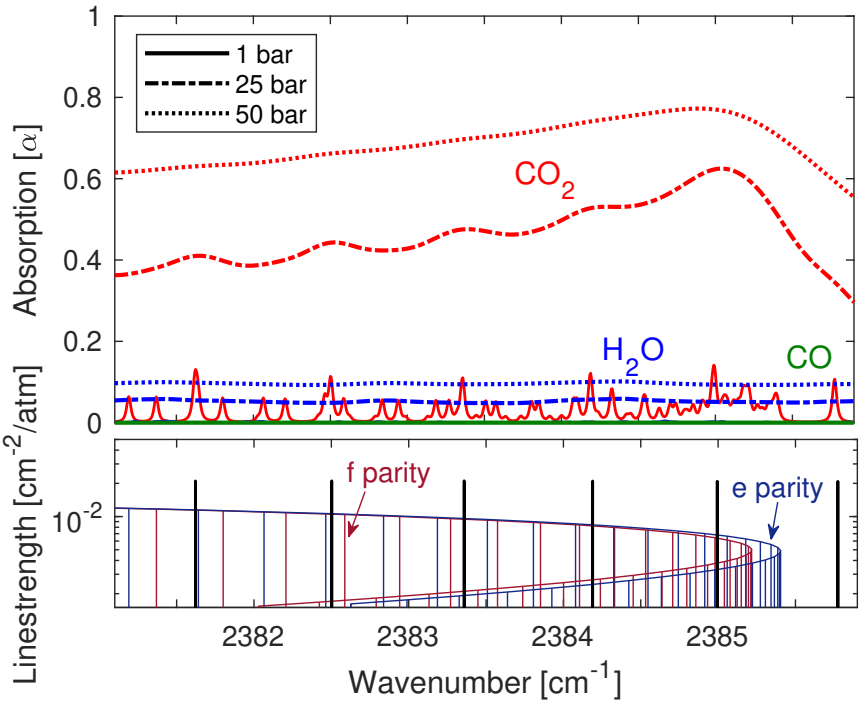

Figure 4.12: Absorption spectra of the $(01^10 \rightarrow 01^11)$ fundamental bandhead of CO_2 with pressure dependence and absorption line-strength (HITEMP: T = 3500 K, X_{CO} = 0.30, X_{CO_2} = 0.10, X_{H_2O} = 0.30)

In order to model the collisional population transfers between neighboring transitions near the bandhead, a modified-exponential gap rate law was adopted, which is discussed in early part of the chapter. This allowed the line mixing effect to be captured within the absorption modeling framework. Notable distinctions for this targeted vibrational bandheads is that the CO_2 bandhead in the $(01^10 \rightarrow 01^11)$ is composed of two subbands with different parities (e and f). In order to successfully construct the relaxation matrix, the Fitting-M method has been implemented where population transfer between different parities is neglected [79]. In other words, MEG law coefficients for each parity were distinctly inferred through least-squares fitting routines to the shock tube data. Figure 4.13 demonstrates that the simulated spectra using the MEG law can accurately reproduce the CO_2 bandhead obtained by shock tube measurements. In addition, Fig. 4.13 illustrates the effect of varying magnitude of population transfer rates which relates to the degree of line mixing.

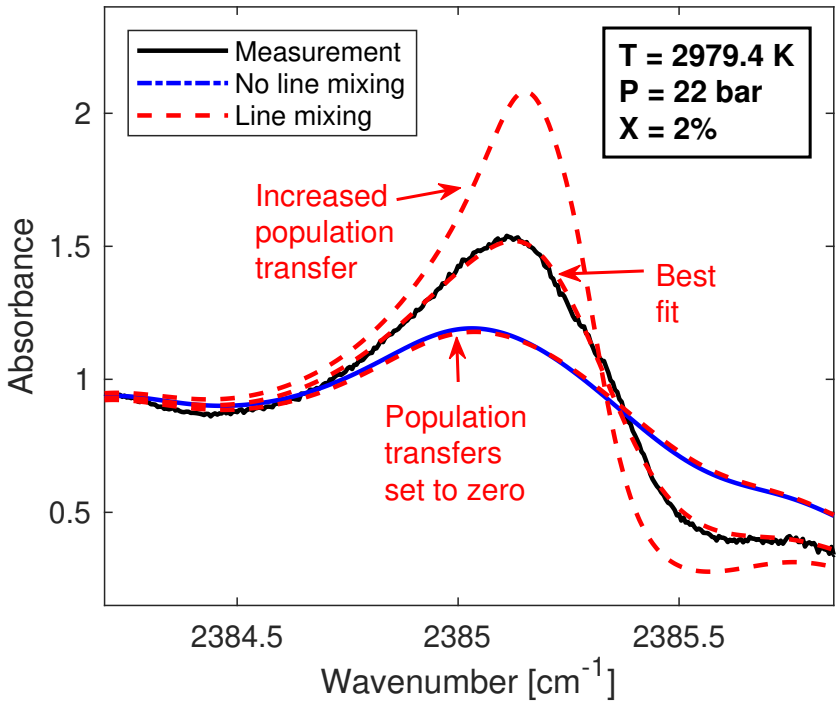

Figure 4.13: Absorbance measurement of the $(01^10 \rightarrow 01^11)$ fundamental bandhead of CO_2 behind a reflected shock wave illustrating line mixing effects with varying magnitude of population transfer rates, including no population transfers

A series of measurements over a range of pressures and mixture ratios (MR) from 25–105 bar and 2.2–4, respectively, have been conducted on a single-element-injector rocket combustor with CH_4/GOx as propellants. The same rocket combustor, located at the Air Force Research Laboratory on Edwards Air Force Base, was used for testing.

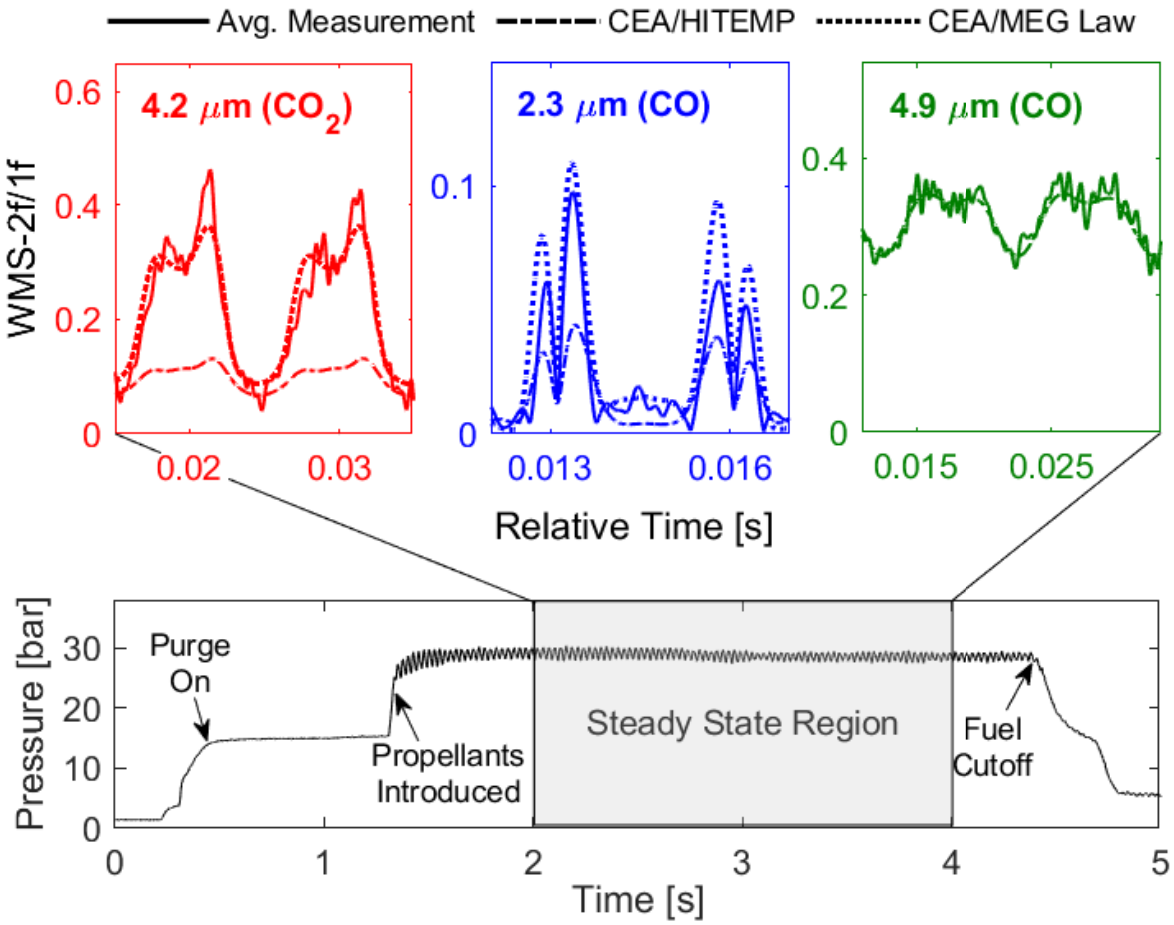

Figure 4.14: (*bottom*) Time evolution of chamber pressure for a representative test and (*top*) averaged WMS-2f/1f signals (background subtracted) shown with simulated WMS signals at: P = 403.7 psi, T = 3099 K, L = 2.54 cm, and X_{CO} = 0.27

Figure 4.14 shows the pressure evolution in time for an example test with corresponding averaged WMS-2f/1f signals at 4.2 μm, 2.3 μm, and 4.9 μm for a steady-state chamber condition of 29 bar and MR ~ 2.9. Raw optical signals at three wavelengths have been averaged over the steady-state region to improve signal-to-noise ratio (SNR) and were processed through a digital lock-in amplifier

to extract the WMS harmonics, from which species and temperature can be inferred. The measured WMS signals were compared to simulated WMS signals using chemical equilibrium (CEA) for mixture composition/temperature and the HITEMP database for spectral parameters. Measurements at the two rovibrational bandheads near 4.2 μm and 2.3 μm have been also compared to an updated model that incorporates line mixing. The measurement at the CO fundamental band demonstrated relatively close agreement with the simulated HITMEP model while the measurements at the two bandheads showed substantial disagreement in both magnitude and spectral shape when not accounting for line mixing. However, once updating the model to account for line mixing, reasonable agreement with both bandhead measurements were observed.

Using the updated line mixing model, the WMS signals were interpreted to

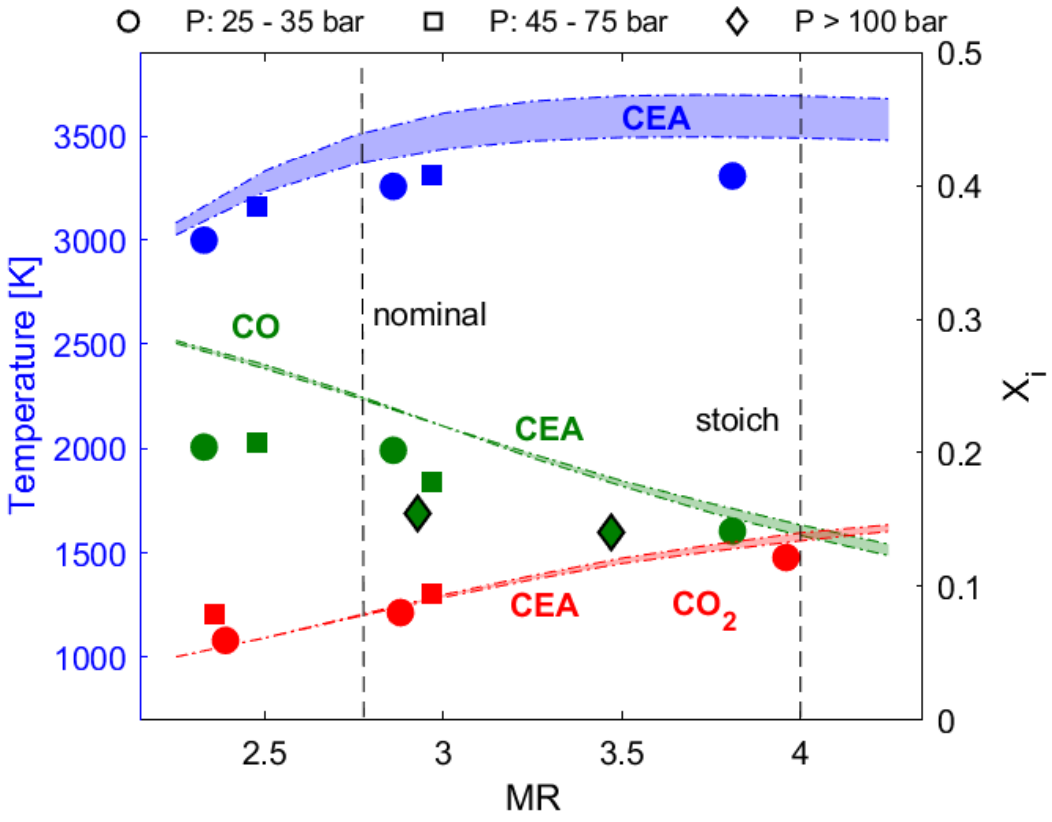

Figure 4.15: Temperature and species measurements at steady-state combustor conditions compared to CEA over a range of mixture ratios and pressures

quantitatively measure temperature and species concentration. The ratio of peak WMS signals from the 2.3 μm and 4.9 μm was utilized to first obtain temperature, which was then used to infer CO and CO_2 concentration based on absolute signal magnitude [45][59].

Figure 4.15 compares measured temperature and mole fraction to chemical equilibrium calculations. The CEA results are bounded by the highest and lowest pressures measured, 105 bar and 28 bar, respectively. In order to obtain mole fraction measurements above 100 bar, where the SNR of the CO fundamental band measurements was deemed too low, the CEA temperature was assumed. Notably, at these conditions the CO overtone bandhead measurement, which exploited line mixing, retained high signal quality (SNR > 10) even at the highest pressures (> 100 bar) and was used to infer mole fraction. The inferred temperatures from all tests followed the expected trends but were slightly lower (generally by 100 - 300 K) than equilibrium temperature, typical of incomplete combustion and possibly related to thermal boundary layers. CO concentration measurements were moderately less than CEA, while CO_2 concentration measurements were slightly higher at lower mixture ratios. The relative values are consistent with total carbon conservation. Generally, mole fraction measurements for both species trended with mixture ratio as anticipated from chemical equilibrium analysis.

CHAPTER 5

Line mixing and broadening of CO_2 at high temperatures and high pressures

The contents of this chapter have been published in the ***Journal of Quantitative Spectroscopy and Radiative Transfer*** *under the full title 'Line mixing and broadening of carbon dioxide by argon in the ν_3 bandhead near 4.2 μm at high temperatures and high pressures' [65].*

5.1 Introduction

Carbon dioxide (CO_2) is an important molecule in climatology, biology, planetary astronomy, and combustion chemistry. High-temperature spectroscopy of CO_2 is relevant for remote sensing of extraterrestrial atmospheres [80, 81], combustion diagnostics [82], and thermal radiation modeling in the development of planetary entry systems [83, 84]. In these applications, quantitative simulation and analysis is enabled by accurate spectroscopic data with appropriate thermodynamic scaling across relevant conditions. This work experimentally investigates the CO_2 spectra near 4.2 μm at high-temperature conditions relevant to combustion and propulsion over a broad range of pressures (up to 58.3 atm), with the goal of developing an accurate model of the target spectral domain that accurately captures relevant collisional effects.

The far-wing R-branch transitions of the CO_2 asymmetric stretch (ν_3) fundamental bands near 4.2 μm have been extensively used for quantitative thermochemical

sensing in combustion flows, owing to the high absorptivity and spectral isolation from other combustion species. Researchers have targeted several rovibrational transitions in these bands for CO_2 measurements to characterize scramjet combustor performance [74] (T = 1500–2500 K, P < 2 atm) and spatially-resolve thermochemistry in flames [85, 86, 87, 88, 89, 90] (T = 1000–2200 K, P ≤ 1 atm). Several shock tube kinetics studies of combustion chemistry have been aided by sensitive time-resolved CO_2 species measurements probing this infrared region [56, 91, 92, 93] (T = 500–2000 K, P ≤ 6 atm). More recently, this spectral domain comprising the bandhead was targeted for in-chamber rocket combus-

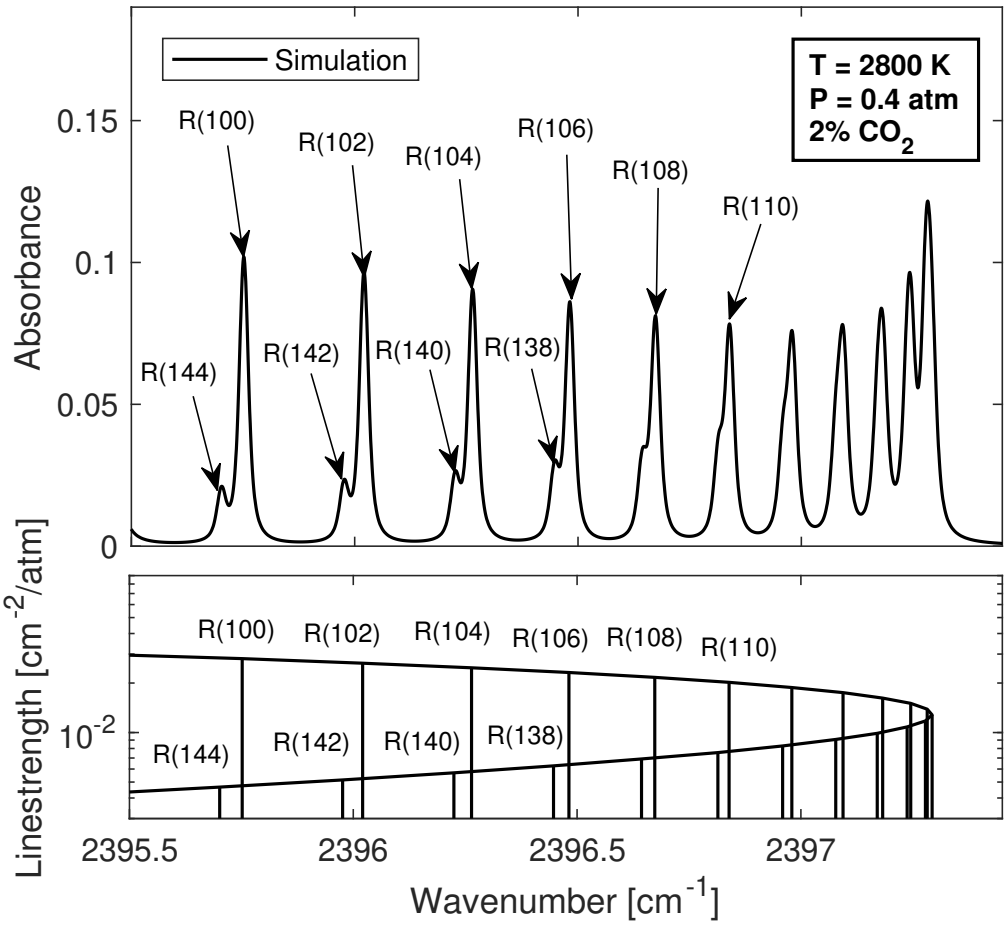

Figure 5.1: (top) Spectral absorbance simulation of the $v_1 v_2{}^{l2} v_3(00^00 \rightarrow 00^01)$ fundamental bandhead of CO_2 at 2800 K and 0.4 atm for 2% CO_2 in air. (bottom) Line positions and magnitudes of the spectral transitions relevant to this work.

tion gas sensing at much higher temperatures and pressures (T > 3000 K, P > 50 atm) [63]. At high gas densities, spectrally dense bandhead regions are susceptible to collisional line mixing in addition to broadening [94]. Here we examine line broadening and mixing of CO_2 in argon (Ar) for a group of high-energy transitions belonging to the $v_1 v_2^{l_2} v_3 (00^0 0 \rightarrow 00^0 1)$ and $(01^1 0 \rightarrow 01^1 1)$ bandheads of CO_2 near 4.17 μm. The target domain of interest for line-mixing studies is shown in Fig. 5.1. The remainder of the manuscript will refer to these regions collectively using a shorthand notation, $v_3(0 \rightarrow 1)$.

Many researchers have quantified and modeled CO_2 line broadening for transitions in the $v_3(0 \rightarrow 1)$ bands, with some reporting broadening effects in Ar [95, 96,

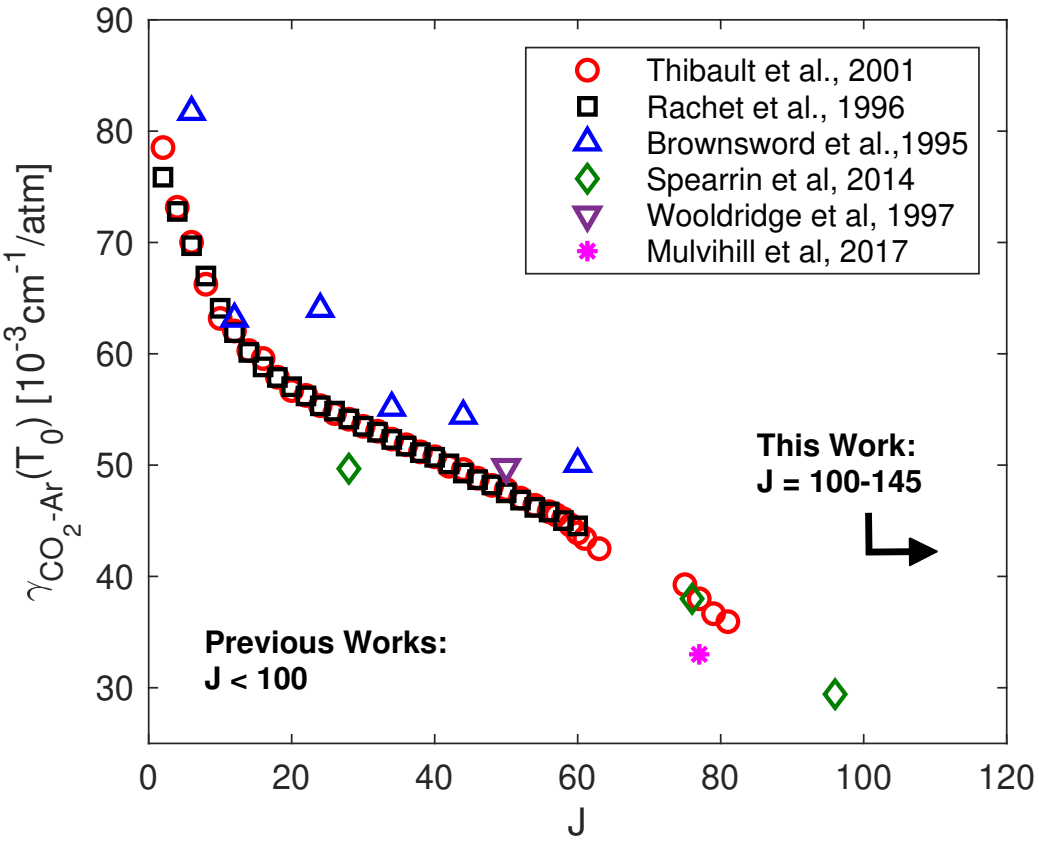

Figure 5.2: Experimental Ar-broadening coefficients for CO_2 transitions obtained by previous works for T_0 = 296 K. The current study focuses on higher rotational quantum number transitions (J = 99–145) to extend diagnostic capabilities at extreme temperatures and pressures.

97, 98, 99, 100, 56, 101], which is often used as a bath gas for chemical kinetics studies in shock tubes. However, to the authors' knowledge no experimentally-measured Ar-broadening parameters are reported for rotational quantum number transitions larger than $J = 100$, as indicated in Fig. 5.2. This is due to most experimental measurements of line broadening coefficients for CO_2 having been conducted below 1000 K, wherein such lines are weakly active. We focus this experimental study to 1200–3000 K and evaluate lines with higher rotational energies (E'' = 3920–8090 cm^{-1}).

Line mixing is a band narrowing effect that occurs at high gas densities, resulting from collision-induced changes in rotational energy and is most evident when collisional linewidths are on the order of line spacing [61]. Line mixing within and in the wings of the ν_3 band of CO_2 has been investigated previously [102, 103, 104, 105, 98, 106, 107], owing in part to its relevance in sensing of the Cytherean[1] atmosphere [80], where pressures at the planet surface can exceed 90 atm. Here we study line mixing in the bandhead of the $\nu_3(0 \rightarrow 1)$ fundamental band of CO_2 at elevated pressures and very high temperatures (up to 2850 K) relevant to hydrocarbon-fueled combustion conditions, wherein (similar to broadening) higher rotational energy states are more populated and prior work is absent.

This paper describes the experimental measurements and modeling of the aforementioned line broadening and mixing effects in the $\nu_3(0 \rightarrow 1)$ fundamental bandhead region of CO_2 at high temperatures and high pressures, with Ar as the collision partner. After establishing the theoretical framework, we present the experimental methods, including the optical setup, shock tube apparatus, and data processing techniques required to obtain broadening and mixing parameters from laser absorption measurements. Broadening parameters are determined at moderate pressures (P < 0.8 atm), where many individual lines can be distinguished. An exponential gap model is then developed to capture line-mixing

[1]The word *Venusian* is also occasionally used to describe properties or behavior pertaining to the planet Venus [108].

effects by fitting multi-line absorption spectra at high-pressure conditions (up to 58.3 atm) generated in a shock tube. The broadening and mixing models are shown to enable accurate spectral simulation of CO_2 near 4.2 μm over a broad range of temperatures and pressures.

5.2 Theory

The theory of laser absorption spectroscopy is described thoroughly in the literature [16]. A previous work by our group on line mixing in CO bandhead spectra [43] provides an analogous and more detailed review on the theoretical framework employed for this study. However, since varying definitions and symbols are present in the literature, we provide a brief overview to assist the reader with context and nomenclature definitions.

5.2.1 Absorption spectroscopy and line broadening

The transmission, τ_ν, of monochromatic light at frequency, ν, through a uniform absorbing gas medium is expressed by the Beer-Lambert law in Eq. (5.1):

$$\tau_\nu = \left(\frac{I}{I_o}\right)_\nu = \exp(-\alpha_\nu) \tag{5.1}$$

where I_o and I are the incident and transmitted light intensities, respectively, and α_ν is the spectral absorbance. In the spectral vicinity of *a single transition*, the spectral absorbance relates to thermophysical gas properties through Eq. (5.2):

$$\alpha_\nu = S(T)NL\phi(\nu) \tag{5.2}$$

where $S(T)$ [$\mathrm{cm}^{-1}/(\mathrm{molec}\cdot\mathrm{cm}^{-2})$] is the line strength of the transition, L [cm] is the path length, $\phi(\nu)$ [cm] is the line shape function, and N [$\mathrm{molec}\cdot\mathrm{cm}^{-3}$] is the total

number density of the absorbing species, given by:

$$N = \frac{PX}{k_B T} \cdot 10^{-6} \tag{5.3}$$

Here, P is the pressure with units of [Pa], X is the mole fraction of the absorber, k_B [J/K] is the Boltzmann constant, and T [K] is the temperature. Based on the compressibility factors for CO_2 and Ar, deviations from the ideal gas assumption implied in Eq. (5.3) are not expected to exceed 0.4% for any condition in this study [109]. We model the spectral line shape, $\phi(\nu)$, using a Voigt profile [61], a convolution of a Lorentzian and a Gaussian profile accounting for collisional and Doppler broadening, respectively. For the Voigt lineshape, both collisional and Doppler broadening are characterized by full width at half maximum (FWHM) parameter; $\Delta\nu_C$ [cm^{-1}] for collisional broadening and $\Delta\nu_D$ [cm^{-1}] for Doppler broadening. Doppler linewidth is given by Eq. (5.4) [16]:

$$\Delta\nu_D = \nu_0 (7.1623 \cdot 10^{-7}) \sqrt{\frac{T}{M}} \tag{5.4}$$

where ν_0 [cm^{-1}] is the transition linecenter and M [g·mol^{-1}] is the molecular weight of the absorbing species. Collisional width scales with the collision frequency of the absorbing molecule A (adjusted for quantum state), and is modeled as the product of pressure and the sum of mole fraction weighted collisional broadening coefficients of each perturbing species B:

$$\Delta\nu_C = P \sum_B X_B 2\gamma_{A-B}(T) \tag{5.5}$$

where $\gamma_{A-B}(T)$ [$cm^{-1}atm^{-1}$] is the transition-dependent collisional broadening coefficient at temperature, T. Note that in Eq. (5.5), total pressure, P, has units of [atm].

As shown in Eq. (5.5), collisional broadening scales with pressure linearly. The

temperature dependence of $\gamma_{A-B}(T)$ is modeled as a power law expression:

$$\gamma_{A-B}(T) = \gamma_{A-B}(T_0)\left(\frac{T_0}{T}\right)^{n_{A-B}} \tag{5.6}$$

where $\gamma_{A-B}(T_0)$ [$\mathrm{cm^{-1}atm^{-1}}$] is the broadening coefficient at a reference temperature, T_0, and n_{A-B} is the line-specific temperature exponent of the absorbing species. As lines become more closely spaced together or pressure increases, the spectral absorbance, α_ν, at a given wavenumber, ν, is no longer a function of just one spectral transition, but is rather a summation of all neighboring transitions as demonstrated in the bandhead shown in Fig. 5.1. In this work, we measure values of γ_{CO_2-Ar} over a range of temperatures (1200–3000 K) and sub-atmospheric pressures to distinguish 17 transitions within the range of J = 99–145. Transitions are probed in both the $(00^00 \rightarrow 00^01)$ and $(01^10 \rightarrow 01^11)$ fundamental bands, recognizing weak vibrational dependence. For each transition, a power law fit with temperature is used to infer n_{CO_2-Ar} and we report $\gamma_{CO_2-Ar}(T_0)$ at a reference temperature of $T_0 = 1200$ K. The parameters for inaccessible (overly blended) lines are determined via interpolation.

5.2.2 Line mixing

Line mixing is a phenomena in which molecular collisions induce a change in rotational energy, typically within a given vibrational energy level. These collision-induced transfers between rotational energy states result in an intensity exchange between neighboring transitions and often leads to a vibrational band narrowing effect [61], which enhances high-absorbing regions. This effect scales with collision frequency (or pressure) and is pronounced in spectrally dense regions, such as bandheads, where line spacing is small. An illustration of the line mixing process for two rovibrational transitions is depicted in Fig. 5.3.

In modeling line-mixing effects, we utilize the relaxation matrix formalism [64], which accounts for aggregate collisional effects (broadening and mixing) on the

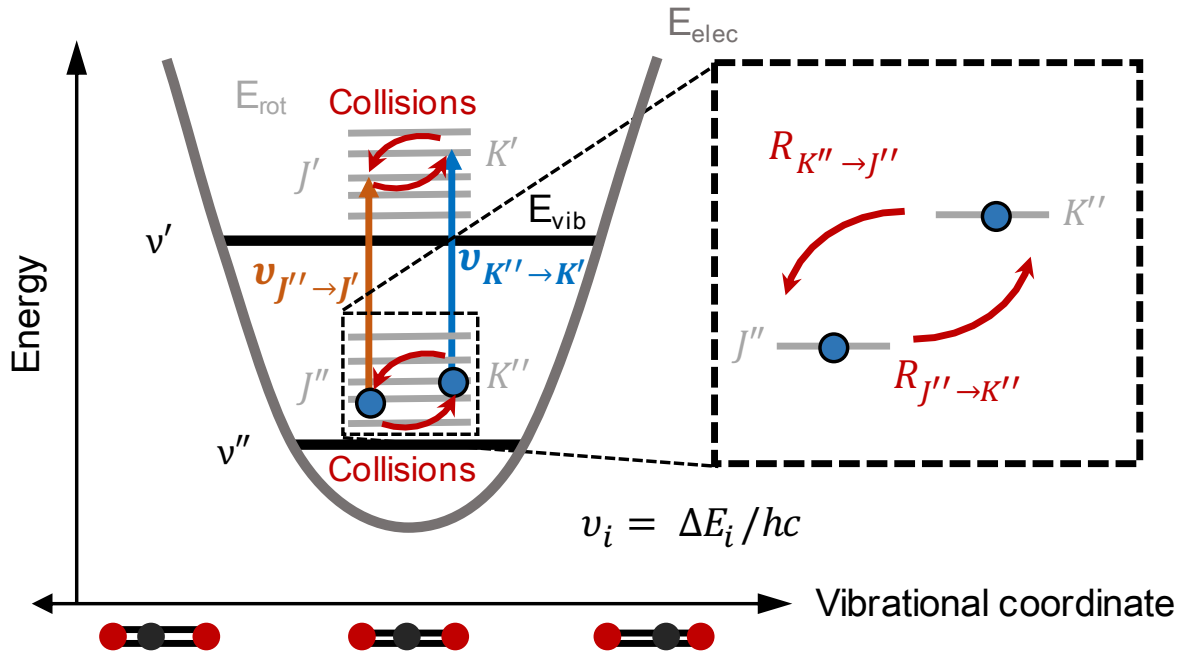

Figure 5.3: Collisional line mixing of rovibrational transitions in a fundamental asymmetric stretch band of a linear polyatomic molecule, adapted from Hartmann [61].

molecular spectra. In the following equations and figures, J and K refer to transitions between lower and upper states $J'' \rightarrow J'$ and $K'' \rightarrow K'$, wherein the state space is generally distinguished from the line space here with the use of prime ($'$) and double prime ($''$) symbols. We express the absorbance, α_ν, for overlapping transitions, within the impact approximation [110], in the following form:

$$\alpha_\nu = \frac{NL}{\pi} \mathrm{Im}(\mathbf{d} \cdot \mathbf{G}^{-1} \cdot \boldsymbol{\rho} \cdot \mathbf{d}) \tag{5.7}$$

where $\boldsymbol{\rho}$ is a diagonal matrix with nonzero elements defined by the lower state Boltzmann population fraction and $\mathbf{d}$ $[\mathrm{cm}^{-1}/(\mathrm{molec} \cdot \mathrm{cm}^{-2})]^{\frac{1}{2}}$ is a vector describing transition amplitudes. Another equivalent form of Eq. (5.7) is shown in the Appendix of Bendana et al [43].

The dependence on wavenumber, ν $[\mathrm{cm}^{-1}]$, in Eq. (5.7) is within $\mathbf{G}$ $[\mathrm{cm}^{-1}]$, a

complex matrix defined as:

$$\mathbf{G} = \nu\mathbf{I} - \boldsymbol{\nu}_0 - iP\mathbf{W} = \nu\mathbf{I} - \mathbf{H} \tag{5.8}$$

where $\mathbf{I}$ is the identity matrix, $\boldsymbol{\nu}_0$ [cm^{-1}] is a diagonal matrix of transition frequencies, and $\mathbf{W}$ [cm^{-1}/atm] is the relaxation matrix [64]. In Eq. (5.8), total pressure, P, is in units of [atm]. The frequency-independent matrix, $\mathbf{H}$, can be diagonalized by a matrix $\mathbf{A}$ using a similarity transform [111] to obtain a diagonal eigenvalue matrix with diagonal elements, ω_J [cm^{-1}]. Since $\mathbf{G}$ differs from $\mathbf{H}$ only by a constant diagonal matrix, $\mathbf{G}^{-1}$ is also diagonalized by $\mathbf{A}$. Eq. (5.7) can now be written as a function of ν summing over all equivalent lines, J:

$$\alpha_\nu = \frac{NL}{\pi} \mathrm{Im}\left[\sum_J \frac{(\mathbf{d}\cdot\mathbf{A})_J(\mathbf{A}^{-1}\cdot\boldsymbol{\rho}\cdot\mathbf{d})_J}{(\nu-\omega_J)}\right] \tag{5.9}$$

We capture line-mixing effects with a relaxation matrix, which is given by:

$$\mathbf{W}_{JK} = \begin{cases} \gamma_J - i\Delta\nu_{0,J} & \text{if } J = K \\ -A_{RR}R_{J''\to K''} & \text{if } J \neq K \end{cases} \tag{5.10}$$

where the real diagonal elements of $\mathbf{W}$ are the broadening coefficients, γ_J, discussed previously (Sec. 5.2.1) and the imaginary diagonal elements are the pressure shifts, $\Delta\nu_{0,J}$ [cm^{-1}/atm]. The imaginary off-diagonal components of $\mathbf{W}$ represent contributions from rovibrational dephasing [68], which can be approximated as zero, and the real off-diagonal elements are approximated by elements proportional to state-specific population transfer rates $R_{J''\to K''}$ [cm^{-1}/atm] multiplied by a scaling factor A_{RR} [61].

Since collisions generally promote the Boltzmann distribution of population, the reciprocal population transfer rates, $R_{J''\to K''}$ and $R_{K''\to J''}$, respectively, are related through the detailed-balance principle [71]. If the off-diagonal elements of the relaxation matrix, W_{JK}, are set to zero, Eq. (5.7) simplifies to the sum of

the Lorentzian lines with no line-mixing effects. Invoking the random phase approximation [100], broadening coefficients can be related to the state-to-state population transfer rates (R) between lower and upper states [61]:

$$\gamma_J = \frac{1}{2}\left[\sum_{J''\neq K''} R_{J''\to K''} + \sum_{J'\neq K'} R_{J'\to K'}\right] \tag{5.11}$$

This equation assumes negligible dephasing contributions from elastic collisions [112].

For multiple collision partners, the full relaxation matrix is expressed as a summation of the individual perturber contributions:

$$\mathbf{W} = \sum_B X_B \mathbf{W}_{A-B} \tag{5.12}$$

We model the real off-diagonal elements of $\mathbf{W}$ with a modified-exponential-gap (MEG) law [69, 70] with the form:

$$W_{JK} = a_1(T)\left[\frac{1 + a_4\left(\frac{E''_J}{a_2 k_B T}\right)}{1 + a_4\left(\frac{E''_J}{k_B T}\right)}\right]^2 \times \exp\left[\frac{-a_3\left(E''_K - E''_J\right)}{k_B T}\right] \tag{5.13}$$

where $a_1(T)$ [cm^{-1}/atm], a_2, and a_3 are species-specific MEG law coefficients obtained by fitting measured absorbance data to the model using a nonlinear least-squares fitting routine. a_4 describes the collision duration [69] based on distance of closest approach [113] and for this study is set to $a_4 = 2$ as an estimate for collisions of linear molecules [43]. The MEG law formulation described here has been successfully implemented for several linear molecules [114, 115, 43], including CO_2 [116, 117]. Though some of these studies have used different a_4 values, the sensitivity of a_4 has been tested using $a_4 = 1$ and $a_4 = 1.5$ and found to have negligible influence on the results [116, 114].

The species-specific MEG law coefficients at a given temperature can be ob-

tained by fitting absorbance spectra [118]. $a_1(T)$ can be modeled as a power law expression to determine the temperature dependence of the relaxation matrix components:

$$a_1(T) = a_1(T_0)\left(\frac{T_0}{T}\right)^m \tag{5.14}$$

where $a_1(T_0)$ is the MEG law coefficient at a reference temperature, T_0, and m is defined as the temperature exponent, obtained by fitting multiple sets of absorbance data over a range of temperatures.

Similar to the reported broadening coefficients, $\gamma_{CO_2\text{–Ar}}$, we report measured values of MEG law coefficients for a_i and the associated temperature exponent, m, at a reference temperature of $T_0 =$ 1200 K. We show that these parameters can be used to accurately model line-mixing effects in the $(00^00 \rightarrow 00^01)$ bandhead of CO_2 near 4.17 μm at high pressures (10–60 atm) over a temperature range of 1200–3000 K.

5.3 Experimental methods

The experiments in this work were conducted using a high-enthalpy shock tube facility [43, 119]. We provide a brief description here for context and reader clarity. The shock tube and corresponding optical setup are illustrated in Fig. 5.4. All laser absorption measurements are attained behind reflected shock waves that near-instantaneously heat a prescribed gas mixture to target conditions for a short test time (milliseconds). Initial reflected shock conditions are determined by measurements of the incident shock speed and normal shock relations, yielding a typical uncertainty of ~1% in temperature when properly accounting for vibrational relaxation of the gas mixture [120]. Prior to each experiment, a roughing pump (Alcatel Adixen 2021i) was used to vacuum down the shock tube to $< 1 \times 10^{-3}$ Torr. Test gas mixtures were barometrically prepared in a 12.5 L agitated mixing tank using a heated capacitance manometer (MKS 627D Baratron) with a full-scale

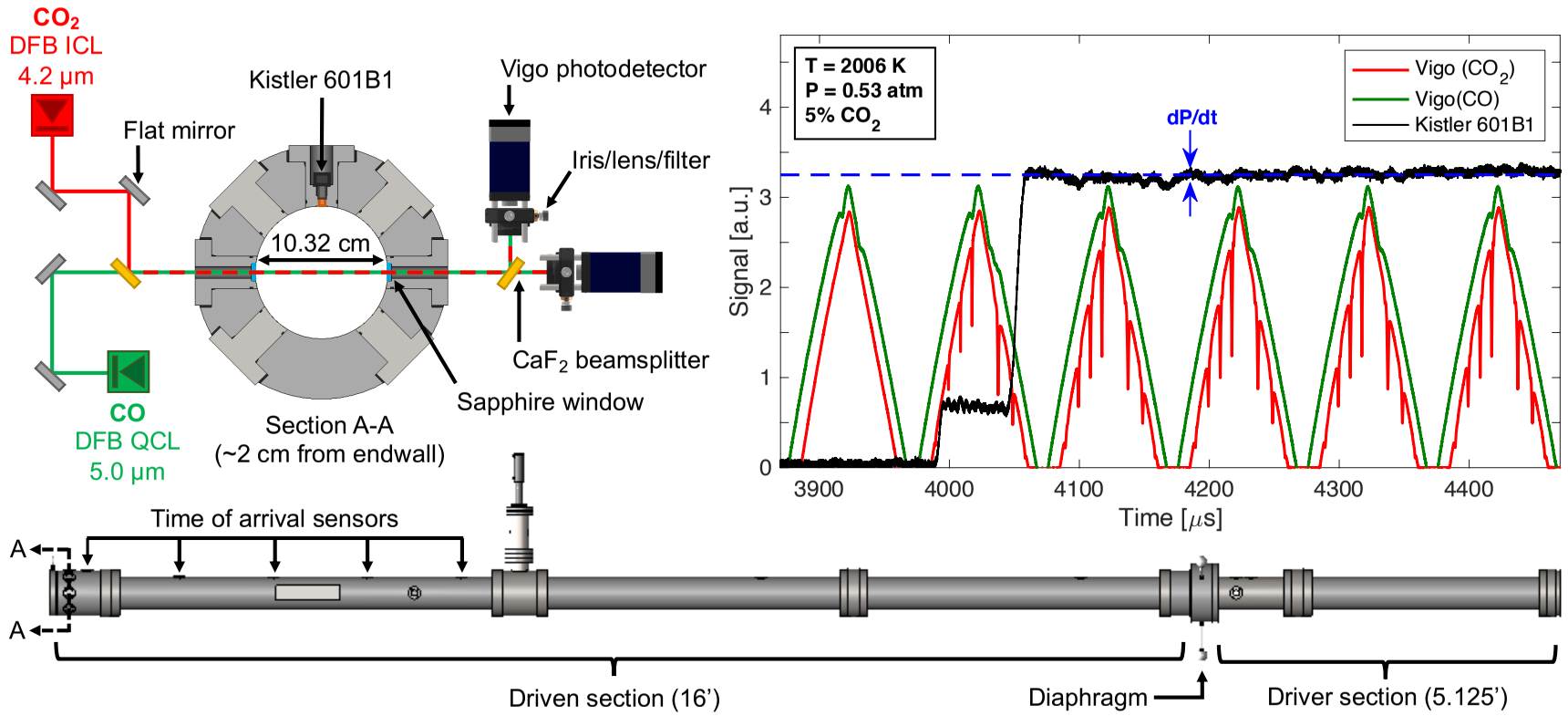

Figure 5.4: (*top left*) Cross-section of the shock tube test section showing windows for optical access and laser/detector setup. *(top right)* Example raw detector and pressure transducer signals during non-reactive shock heating of 5% CO_2 in Ar. *(bottom)* Side view of the shock tube showing lengths of the driven and driver sections of the tube as well as the locations of the time-of-arrival sensors.

pressure range of 1000 Torr and an uncertainty of 0.12% of the reading. At higher pressures, an additional pressure transducer (Setra GCT-225) with an accuracy of 0.25% of the full scale (1000 psi) was used to prepare mixtures. All gases were supplied by Airgas, Inc. with purity levels of 99.999% for CO_2, 99.999% for Ar, and 99.995% for N_2 and He. Different mixtures were prepared for collisional broadening and line mixing investigations (2%–5% CO_2/Ar) depending on the expected intensity of the transitions being measured; higher concentrations of CO_2 were used for the higher J lines to increase absorbance and measurement signal-to-noise. Different driver gases (either N_2 or He) and diaphragm thicknesses were used depending on the reflected shock conditions desired.

Two continuous-wave (CW) distributed feedback (DFB) interband cascade lasers (Nanoplus) were utilized to spectrally-resolve the mid-infrared CO_2 spectra. Each ICL has approximately ~3 mW output power, and is rapidly tunable via injection current. One ICL targeted the primary domain of interest near 4.17 μm (2395–2398 cm^{-1}) to study lines near the $(00^00 \rightarrow 00^01)$ bandhead. As seen in Fig. 5.1, this spectral region consists of even J = 100–144. As is common in bandheads, many of these lines are blended together even at moderate pressures (< 0.5 atm), precluding distinct broadening measurements for several lines. To build a more comprehensive broadening dataset and establish a J-dependence, additional CO_2 transitions from the neighboring $(01^10 \rightarrow 01^11)$ band with similar J (99–145) were also evaluated using an ICL near 4.19 μm (2383–2385 cm^{-1}). It should be noted that vibrational dependence of broadening is expected to be less than 2% [121, 122] and, as a result, was considered negligible. While the two aforementioned bands were targeted for broadening measurements of similar high J lines, only the $(00^00 \rightarrow 00^01)$ bandhead near 2398 cm^{-1} was investigated for line mixing. To confirm that CO_2 did not dissociate into CO during the shock-heated experiments, we also used a quantum cascade laser (QCL, ALPES) centered at 4.98 μm targeting the P(0,31) and P(2,20) transitions in the CO fundamental bands ($\Delta v = 1$).

The interband cascade lasers were injection current tuned with 10 kHz triangle

waveforms, shown in Fig. 5.4, over a wavenumber range of ~1.6 cm^{-1} at various intervals between 2382–2400 cm^{-1}. Similarly, the QCL targeting CO was tuned over a wavenumber range of ~1.2 cm^{-1} between 2008–2009 cm^{-1} at a similar frequency. For all lasers, the injection current was scanned below the lasing threshold to account for transient thermal emission during the measurements. The relative frequency of the laser light during the scan was determined using a germanium etalon with a free spectral range of 0.0231 cm^{-1}. During the experiments, the incident light was pitched through a CaF_2 beamsplitter and across the shock tube through two 0.5° wedged sapphire windows with a 9.5 mm aperture, as shown in Fig. 5.4. The transmitted light was again passed through a beamsplitter, followed by a bandpass spectral filter (Electro Optical Components, 4210±42 nm or Spectrogon, 4960±148 nm) to separate the two light sources. After the spectral filters, the light from each respective wavelength passed through an iris to mitigate thermal emission, and was focused onto a thermo-electrically cooled photodetector (Vigo PVI-4TE-5) using a CaF_2 plano-convex lens. Incident and reflected shock pressures were measured by a dynamic pressure transducer (Kistler 601B1) mounted in one of the test section ports and connected to a charge amplifier (Kistler 5018A). Pressure and detector data were collected on a PicoScope 4000 series data acquisition module at 80 MHz while detector data were sampled at the maximum detector bandwidth of 10 MHz, yielding an equivalent measurement rate of 5 MHz.

Representative raw time-resolved signals from a shock tube experiment are shown in Fig. 5.4. Following the passage of the incident and reflected shocks, the target lines appear as the high temperatures more densely populate the high J'' rotational energy levels. During the experiment, a non-ideal pressure rise was occasionally observed and accounted for by assuming isentropic compression of the test gas [43]. This assumption has been validated as an accurate method for correcting thermodynamic conditions behind reflected shock waves [123]. For a single scan interval, the change in temperature and pressure are less than 0.75%

and 0.5%, respectively; thus, the thermodynamic properties were assigned at the scan mid-point and assumed to be constant during each scan.

Shock tube experiments for Ar line broadening parameters of CO_2 were conducted over a temperature range of 1200–3000 K and a pressure range of 0.352–0.804 atm. Moderate pressures were targeted for line-broadening experiments to minimize spectral blending amongst neighboring transitions and resolve the line-specific broadening and temperature coefficients discussed in Section 5.2.1. Shock tube experiments for line-mixing parameters covered a temperature and pressure range of 2000–3000 K and 16.5–58.3 atm, respectively. Higher pressures were targeted for line-mixing experiments in order to determine MEG law coefficients and prove pressure scalability. A complete test matrix of all the experimental conditions for these measurements can be found in the Supplementary Material.

For each experiment, absorbance, α_ν, was determined through Eq. (5.1) via measurements of incident and transmitted intensity, I_0 and I. The incident laser light intensity through the shock tube was measured without a mixture present prior to each shock experiment to provide a baseline I_0 for calculation of α_ν. Each scan of the transmitted laser intensity, I, was corrected for detector offset from both emission and dark current noise by tuning below the lasing threshold. Minimal emission was observed throughout the tests, as seen in the representative data from Fig. 5.4. To obtain line-broadening coefficients, the measured absorbance spectra for a group of transitions (regions identified in Fig. 5.5) was least-squares fit with Voigt lineshape functions with broadening coefficient, $\gamma(T)$, and line position, ν_0, set as the free parameters. It should be noted that since the fit was performed on a group of transitions, the relative line position is critical; therefore, the bounds for ν_0 were determined by uncertainties in the etalon measurement. X, T, P, and L were held constant and determined from the barometric mixture preparation, reflected shock conditions, and shock tube geometry. The minor self-broadening from CO_2 was also included in the simulation, effectively correcting for this contribution. For higher-pressure line-

mixing experiments, the MEG law coefficients were set as free parameters with the diagonals of the relaxation matrix assigned with the pre-determined broadening coefficients.

5.4 Results and discussion

Temperature dependent line-broadening coefficients of CO_2 with Ar are reported for transitions in the range of J = 99–145, suitable for spectral modeling over a temperature range of 1200–3000 K. Seventeen transitions are measured directly through line fitting, while the remainder are inferred via interpolation (and compared with measured spectra). Line mixing coefficients are also reported for the $(00^00 \rightarrow 00^01)$ bandhead region near 2395–2398 cm^{-1} to capture the spectral distortion effects at pressures up to 58 atm and similarly high temperatures. The following two subsections detail the line-broadening and line-mixing results, respectively.

5.4.1 Line broadening

As described in Sec. 3, scanned-wavelength laser absorption measurements were made behind reflected shocks to gather CO_2 spectral data from 1200–3000 K. Representative single-scan absorbance measurements from shock tube experiments with corresponding Voigt line fits are shown in Fig. 5.5 for the spectral regions (A, B, and C) evaluated in this work. As indicated and aforementioned, measurements were conducted in two different bands to empirically-determine Ar-broadening parameters for rovibrational transitions in the range of J= 99–145. The primary motivation of this work was to accurately model the $(00^00 \rightarrow 00^01)$ bandhead region near 2395–2398 cm^{-1} over a wide range of temperatures and pressures. However, fitting individual lines in this domain proved difficult due to severe overlap near the bandhead. As such, distinct line fits in the $(00^00 \rightarrow 00^01)$ band were restricted

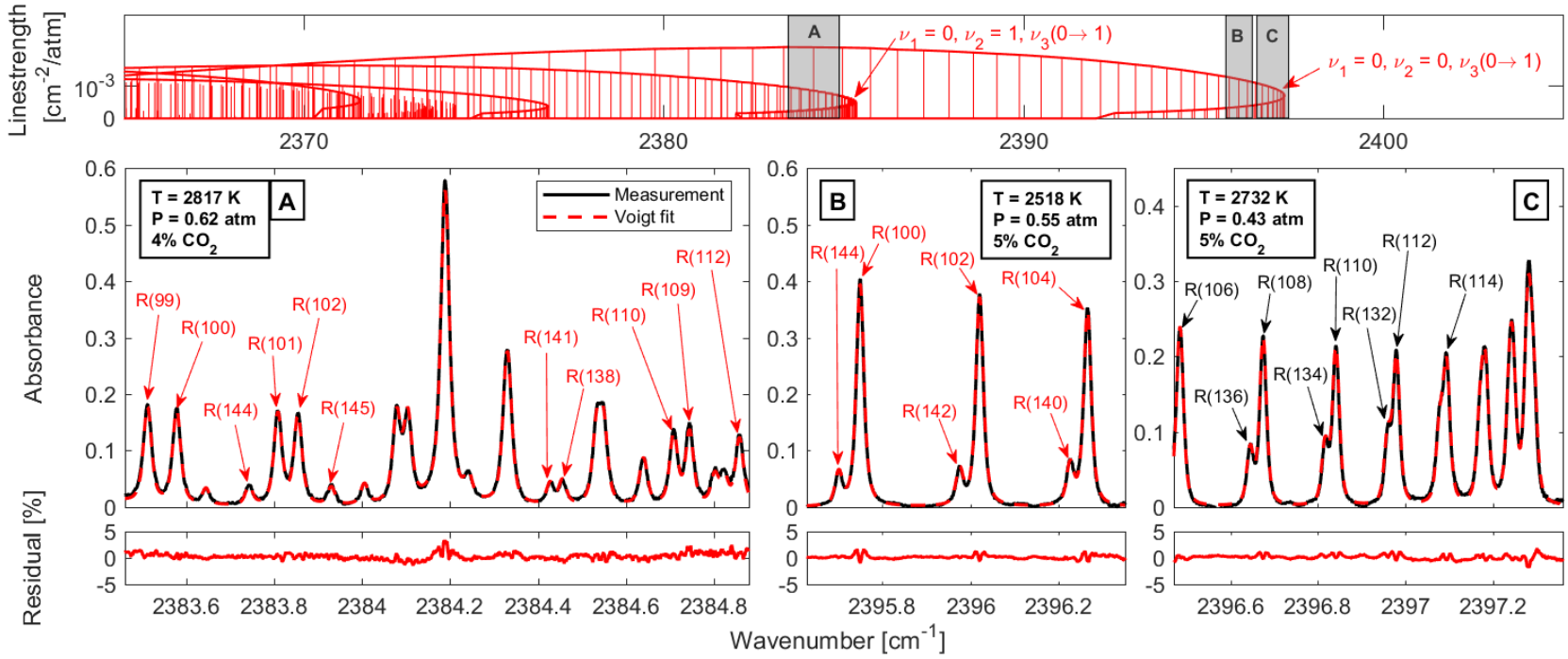

Figure 5.5: (*top*) Linestrengths for transitions of the $\nu_3(0 \rightarrow 1)$ bands of CO_2 near 4.2 μm, with bands of interest noted. *(bottom)* Measured absorbance and corresponding Voigt fits for the transitions shown, using the broadening parameters reported in **Table 5.1**. Transitions with broadening parameters directly measured in this work noted in red, while those with inferred parameters are noted in black.

to Region B, near 4.17 μm, which included only 6 of the 22 lines of interest (note only even J are allowed in this band). Despite the dataset including transitions before and after the bandhead (higher and lower J), the sparse number of lines was deemed insufficient to infer the parameters of the intermediate J. Accordingly, an additional 11 transitions near 4.19 μm were distinctly measured from the $(01^10 \rightarrow 01^11)$ band, shown in Fig. 5.5 Region A. This region similarly includes a number of other lines that could not be fit reliably due to severe overlap or weak absorbance and are excluded in subsequent data analysis. The 17 lines from which fitting parameters were used are labeled in red by their lower state rotational quantum number in Fig. 5.5.

Region C in Fig. 5.5 shows a comparison between a low-pressure measurement of the blended $(00^00 \rightarrow 00^01)$ bandhead and a simulation using the line broadening parameters which were interpolated based on the measurements from Regions A and B. Details regarding the data analysis process to obtain these results are discussed here. Generally, the Voigt fits of lines in Regions A and B produced low peak residuals (1–2%). At high temperatures and moderate pressures the Ar-broadened spectra exhibited some evidence of collisional narrowing (gull-wing residual) [124], but the signal-to-noise ratio was deemed insufficient to rigorously evaluate more advanced lineshapes than the Voigt (which performed quite well). In order to accurately determine Ar-broadened line parameters from the Voigt fits, the contribution from self-broadening, calculated from the line parameters reported in the HITEMP database [44], have been subtracted from the measured collision widths.

Figure 5.6 shows the CO_2–Ar broadening coefficient versus temperature for a subset of transitions before and after the bandhead, representing all relevant temperature conditions. The measured broadening coefficients were fit with a power law to obtain a temperature dependence, $\gamma(T)$, for each transition. It can be noted that at the lower temperatures, the highest J lines could not be reliably discerned, reducing the number of data points available to the power law fit. To

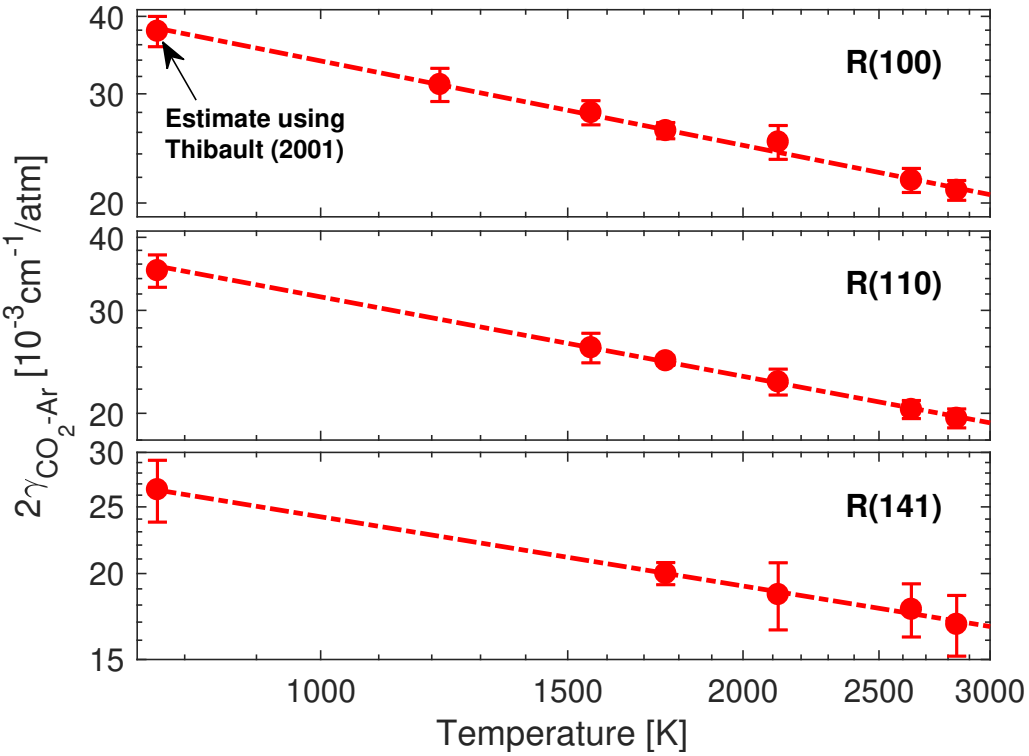

Figure 5.6: Ar-broadening coefficients for the transitions of interest with power law fits for 765–3000 K.

help reduce uncertainty in the temperature dependence for the lines measured in this work and constrain the power law fits, we incorporate estimates of $\gamma_{CO_2\text{–Ar}}$ at 765 K by performing a linear regression of data reported by Thibault [100] measured for lower J transitions [125]. More detail on the calculation of these estimates and their associated uncertainties is provided in 5.6. Subsequently, the $\gamma(T)$ values for each measured transition were used in a linear regression to estimate the relationship between $\gamma(T)$ vs J, shown as dash-dotted lines in Fig. 5.7, for different temperatures.

As discussed previously, line-broadening experiments targeted lower pressures (<0.8 atm) to minimize spectral blending from neighboring transitions, which become more significant near the bandhead and complicates the spectral fitting. Despite utilizing multiple bandheads and the low pressures of the experiments, the R(113)–R(137) transitions are too closely spaced and blended to reliably fit

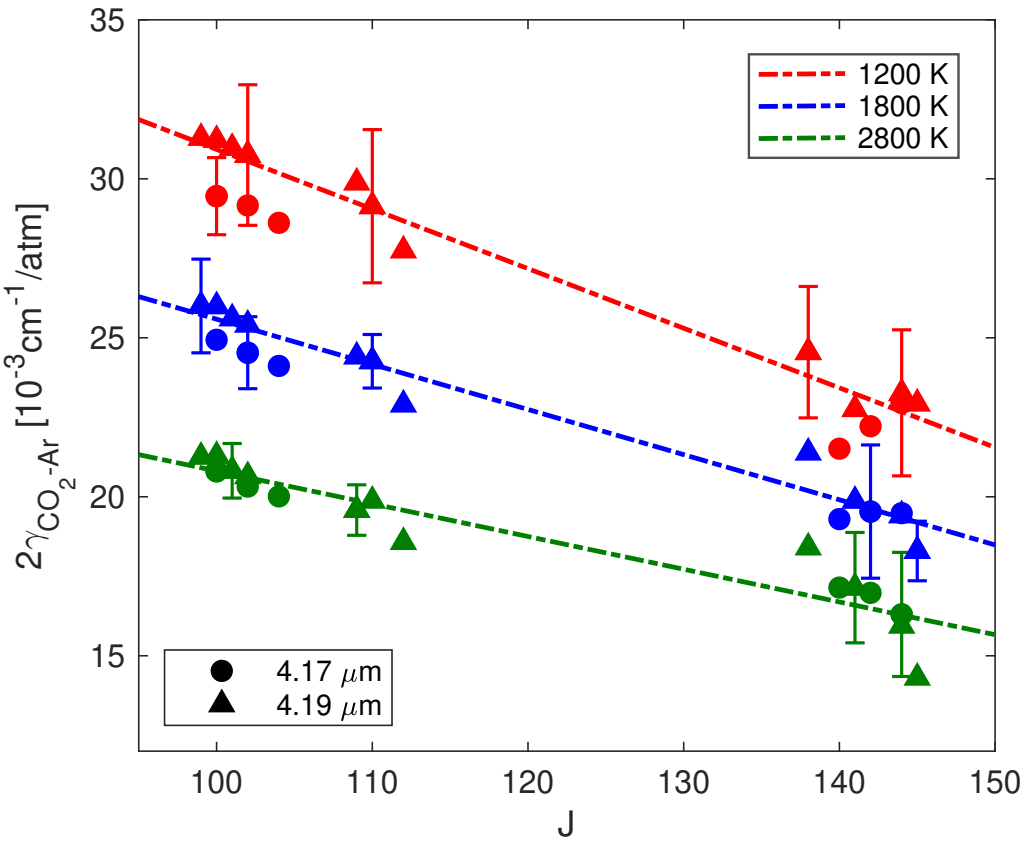

Figure 5.7: Measured broadening coefficients $2\gamma_{CO_2-Ar}$ (markers) for $J = 99$–145 for 1200 K (red), 1800 K (blue), and 2800 K (green). Least-squares exponential fits (lines) of the measured (filled markers) are used to estimate $2\gamma_{CO_2-Ar}$ for J too interfered to measure directly. Representative error bars shown for plot clarity.

and extract broadening information. Accordingly, we infer broadening coefficients for these lines via the linear interpolation, as indicated in Fig. 5.7. The linear relationship between γ_{CO_2-Ar} [cm^{-1}/atm] and J at temperature 1200 K can be expressed with the following equation:

$$\gamma_{CO_2-Ar}(1200\ K) = 0.025 - 9.205 \times 10^{-5}(J) \tag{5.15}$$

Temperature-dependent exponents n_{CO_2-Ar} for all measured and interpolated transitions are determined by similarly fitting the inferred broadening coefficients $\gamma_{CO_2-Ar}(T)$ over the range of test temperatures. The resulting values of n_{CO_2-Ar} can

be modeled as a function of J using the following equation:

$$n_{CO_2-Ar} = 0.708 - 2.417 \times 10^{-3}(J) \tag{5.16}$$

Note this expression is only considered suitable for J = 99–145. The corresponding broadening parameters for select transitions and their uncertainties are listed in Table 5.1 with a reference temperature of T_0 = 1200 K. Superscripts in the table indicate if the reported parameter is from an interpolated transition. Power-law fits of all measured broadening coefficients versus temperature (similar to the subset shown in Fig. 5.6) are provided in the Supplementary Material to support these summary results. The values in Table 5.1 and predicted by Eq. (5.16) are considered most appropriate for a temperature range T = 1200–3000 K.

Revisiting Fig. 5.5, it can be noted that the interpolated broadening parameters in Region C, when coupled with a Voigt lineshape simulation, yield excellent agreement with measured spectra. The spectra in Region C exhibits very low residuals (< 2%) despite the indirect inference using data from Regions A and B. The slightly more pronounced discrepancy at the bandhead near 2397.3 cm^{-1} provides evidence of line-mixing effects even at these lower pressures [85, 87].

5.4.2 Line mixing

As discussed in Sec. 5.2.2, the relaxation matrix, **W**, accounts for the collision-induced population transfer rates that determine line mixing and narrowing effects in the molecular spectra. The real diagonal elements of **W** are the broadening coefficients, γ_J, the imaginary diagonal elements are the pressure shifts, $\Delta\nu_{0,J}$, the real off-diagonal elements are proportional to the state-specific population transfer rates, $R_{J''\rightarrow K''}$, and the imaginary off-diagonal components are approximated as zero. The reported broadening coefficients in Table 5.1 and pressure shift coefficients from the HITEMP database [44] are used to complete the real and imaginary diagonal elements of **W**, respectively. Though the HITEMP database only provides

Table 5.1: Ar-broadened line parameters for the CO_2 $v_3(0 \rightarrow 1)$ bands

Transition (v_3'', J'')	$\gamma_{CO_2\text{–Ar}}$(1200 K) [10^{-3} $cm^{-1}atm^{-1}$]	$n_{CO_2\text{–Ar}}$
R(0,100)	15.26 ± 0.63	0.466 ± 0.012
R(0,105)	14.80 ± 0.55[a]	0.454 ± 0.014[a]
R(0,110)	14.34 ± 1.18	0.442 ± 0.024
R(0,115)	13.88 ± 1.38[a]	0.430 ± 0.023[a]
R(0,120)	13.42 ± 1.23[a]	0.418 ± 0.040[a]
R(0,125)	12.96 ± 1.19[a]	0.406 ± 0.039[a]
R(0,130)	12.50 ± 1.15[a]	0.394 ± 0.038[a]
R(0,135)	12.04 ± 1.01[a]	0.382 ± 0.053[a]
R(0,140)	11.58 ± 0.92	0.370 ± 0.053
R(0,145)	11.12 ± 0.68	0.357 ± 0.024

[a] Interpolation based on J-dependence (reference Fig. 5.7)

CO_2-air pressure shift coefficients, deviations from this assumption were found to negligibly affect the fitting results. The real off-diagonal elements were obtained through the MEG law, described by Eq. (5.13), and the detailed balance principle for a grouping of 34 transitions from J = 88–154. To find the MEG law coefficients, a_i, high pressure absorbance data measured using the shock tube facility are least-squares fit with the absorbance model given by Eq. (5.7), with a_1, a_2, and a_3 set as the free parameters. This procedure was carried out with test gas mixtures of 2% CO_2/Ar to obtain the appropriate rates for CO_2-Ar collisions using Eq. (5.12).

A comparison of representative high-pressure absorbance data collected in the shock tube at 36 atm and 2493 K is shown in Fig. 5.8 with various simulations. The measured data is compared to simulated results using the line-mixing model developed in the present work and a model developed by Lamouroux et al [107] for CO_2 line mixing in air based on the HITRAN 2016 database [125]. Notably, the air-broadened line-mixing model based on HITRAN 2016 poorly represents the measured spectra at all wavenumbers of interest; the disagreement is largely due to several missing high J transitions, which are included in the HITEMP database [44]. Using the HITEMP database with the updated Ar-broadening

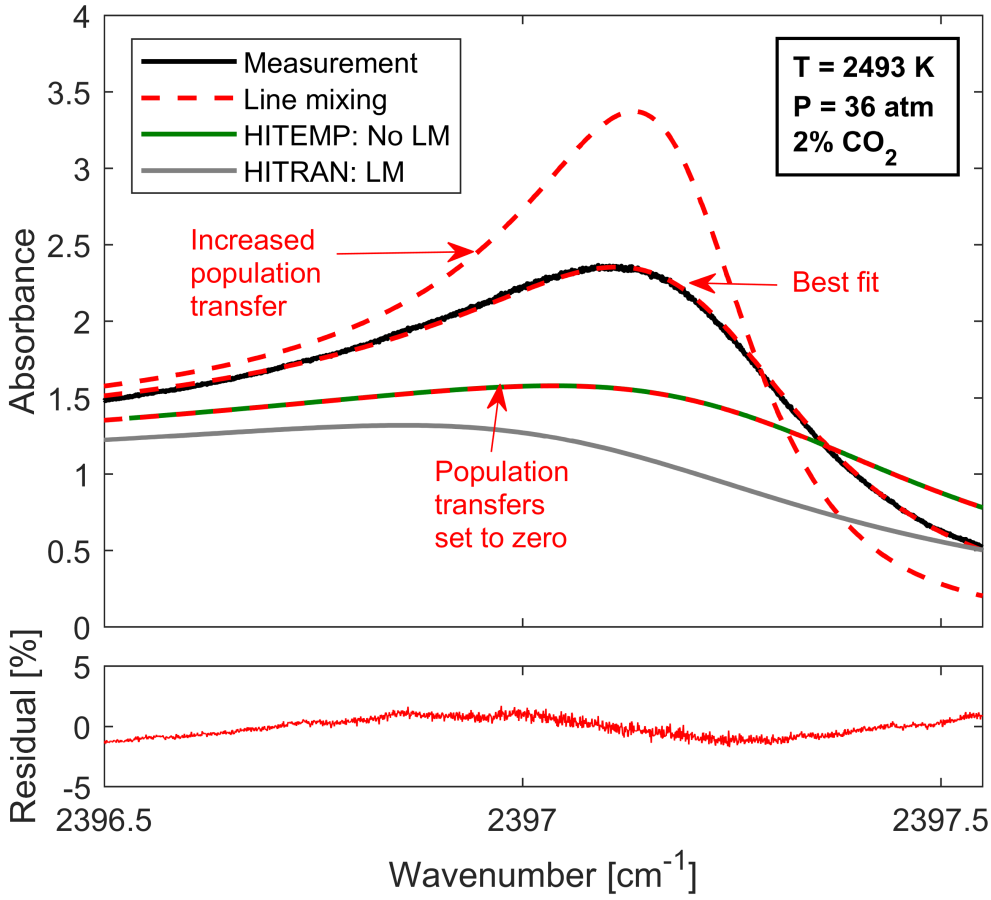

Figure 5.8: Absorbance measurement of the $(00^00 \rightarrow 00^01)$ fundamental bandhead of CO_2 at 2493 K and 36 atm with spectral simulations using Eq. (5.2) (green), Eq. (5.7) (red) with varying magnitude of population transfer rates, including no population transfers ($a_1 = 0$), and the line mixing model developed by Lamouroux et al [107] available in the HITRAN database [125] (grey).

parameters reported in Table 5.1 yields a prediction closer to the measurement; however, without considering line mixing, the simulated spectra significantly underpredicts absorbance near the bandhead, where pronounced narrowing occurs. Implementing the aforementioned MEG law fitting routine enables a highly accurate reconstruction of the spectra with residual $< 3\%$. This compares to a disagreement of nearly 30% at the bandhead peak without accounting for line mixing. Notably, away from the bandhead, the line mixing model still agrees well with both the measured absorbance and converges to simulated spectra that ignores line mixing. To illustrate the sensitivity to the MEG law coefficients, we

adjust the a_1 parameter (+45%) to vary the degree of line mixing and visualize the associated changes in the spectra. As population transfer rates increase, line mixing favors intensity transfers from weak absorption regions to strong absorption regions, consequently narrowing the spectral structure and increasing the differential absorption near the bandhead.

It is informative to compare the transfer rates of different transitions as a function of ΔJ. Figure 5.9 shows the real off-diagonal elements of the relaxation matrix, W_{JK}, which are proportional to the state-to-state transfer rates, $R_{J''\to K''}$, for select transitions given by the line mixing model at two conditions. In this bandhead, similar to others [43, 67], we observe that $R_{J''\to K''}$ decays as ΔJ increases, which may be interpreted as collision-induced transfers across larger differences

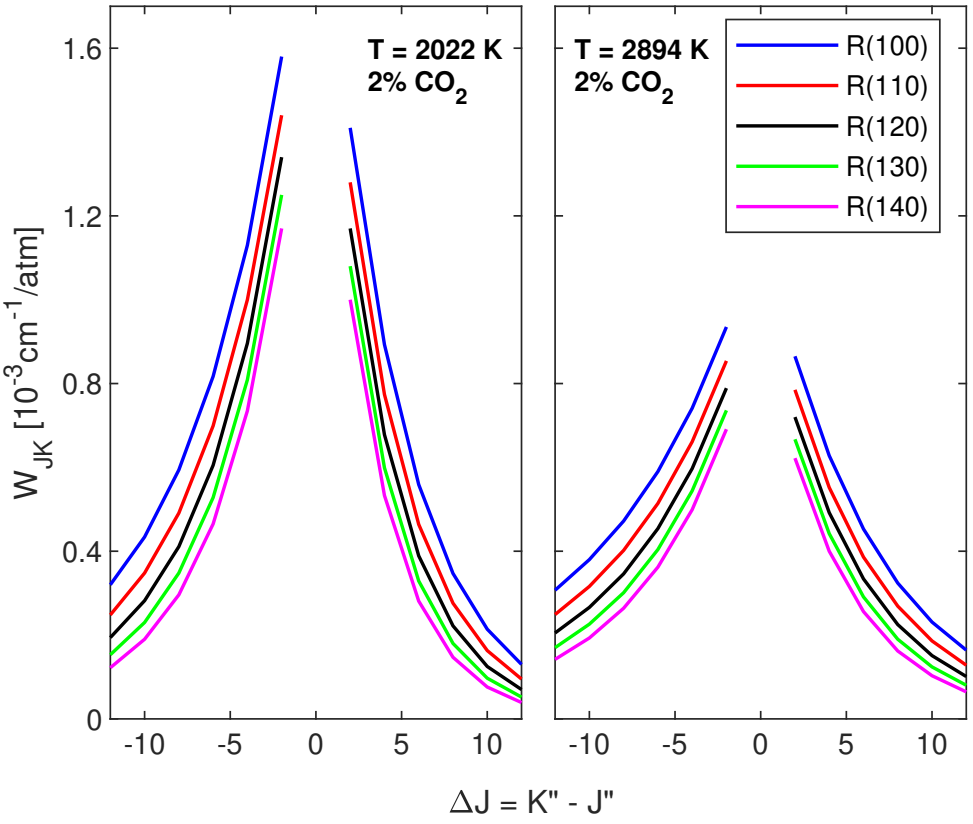

Figure 5.9: W_{JK} given by the MEG model, from selected initial states J''= 100, 110, 120, 130, and 140 to final K'' states, plotted as $\Delta J = K'' - J''$.

in rotational levels requiring more energy. Fig. 5.9 illustrates that at higher temperatures, the population transfers from larger ΔJ become more significant. This can be described through Eq. (5.13). Notably, the relaxation matrix scales linearly with pressure, but the relative probability of collision-induced transfers between a given ΔJ is only dependent on temperature. As shown here and similar to our previous line-mixing study [43], at very high temperatures (> 2500 K), population transfers with $\Delta J > \pm 1$ significantly contribute to the population redistribution in the bandhead.

With the MEG law coefficients inferred empirically at various conditions, the temperature dependence of $a_1(T)$ was found through Eq. (5.14) by fitting experimental data at different temperatures, while holding a_2 and a_3 constant. The temperature dependence of the relaxation matrix is captured in Fig. 5.10 for CO_2-

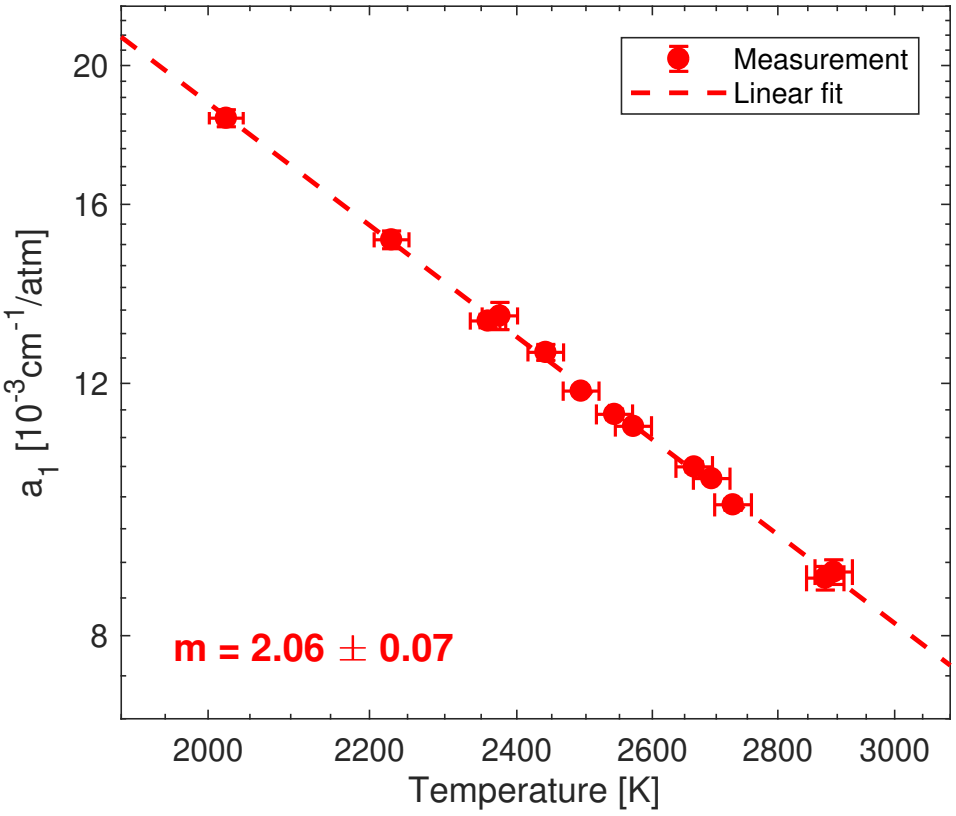

Figure 5.10: Best-fit determinations of a_1 for different temperatures (markers) with power law fits (dashed line) for CO_2-Ar collisional line mixing.

Table 5.2: Temperature-dependent MEG law parameters determined in this work

	a_1(1200 K) [10^{-3} $cm^{-1}atm^{-1}$]	a_2	a_3	a_4	m
CO_2-Ar	53.94 ± 2.49	4.98 ± 0.25	3.19 ± 0.13	2	2.06 ± 0.07

Ar collisions. Notably, the temperature exponents for the off-diagonal components of the relaxation matrix are larger than those of the corresponding broadening coefficients. For CO_2-Ar collisions, a_2 and a_3 were obtained at 2571 K and 58.3 atm with a_1 reported at a reference temperature of T_0 = 1200 K. The reported MEG law coefficients can be found in Table 5.2. Importantly, the W_{JK} elements proportional to the specific transfer rates obtained by the reported MEG law coefficients do not completely sum up to the broadening coefficient (as shown in Eq. (5.11)) due to either the A_{RR} factor being less than unity or other state-changing collisions outside of the domain considered. For a given rovibrational line, the proxy transfer rates for the grouping of lines considered here summed to a typical value of approximately 70% of the corresponding broadening coefficient. As such, caution should be exercised in using this relaxation matrix beyond modeling the target absorption spectra, as the real off-diagonal absolute values have not been normalized.

With an established temperature dependence for W_{JK} and γ_J, the target bandhead spectra can be simulated over a wide range of temperatures and pressures. To validate the pressure scalability and accuracy of the line mixing model, a series of shock tube experiments were conducted from 16.5–58.3 atm for 2% CO_2/Ar at similar temperatures, respectively, as shown in Fig. 5.11. At all conditions, the line mixing model exhibits excellent agreement with the measured absorbance spectra.

5.5 Conclusion

Ar-broadening coefficients and temperature-dependent exponents have been reported for mid-wave infrared CO_2 transitions (J = 99–145) in the $\nu_3(0 \rightarrow 1)$ fun-

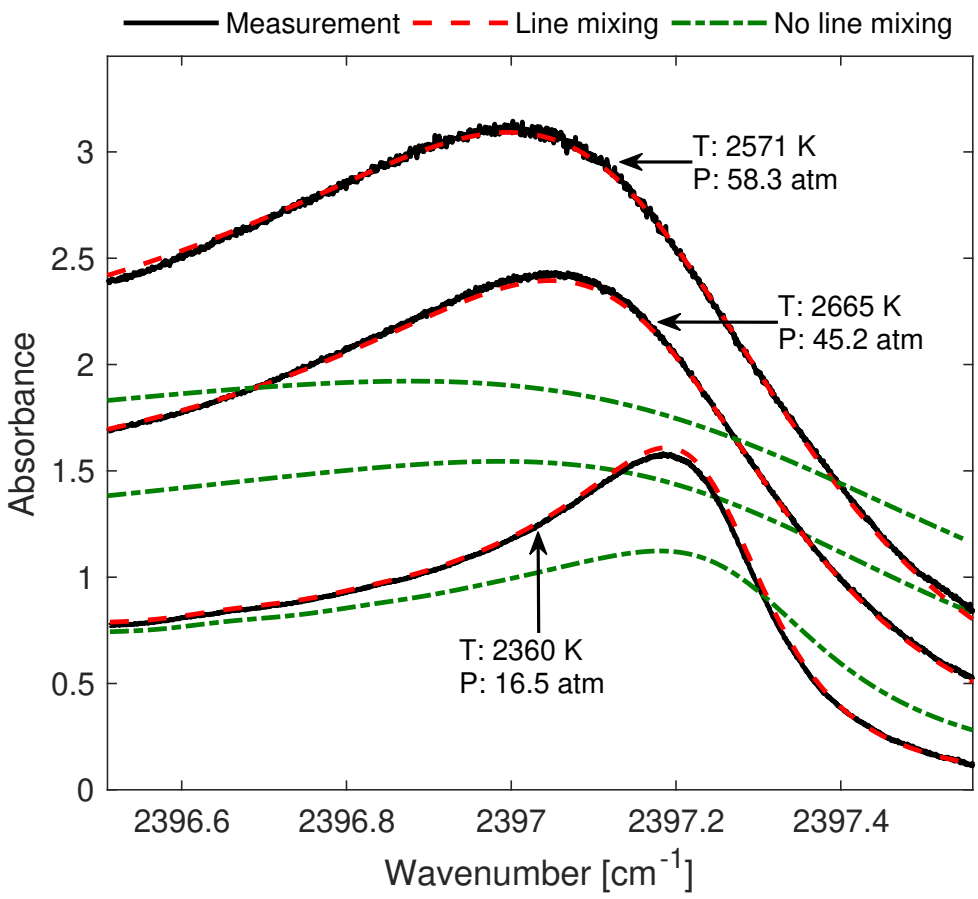

Figure 5.11: CO_2-Ar: measured spectral absorbance compared to the developed MEG model used capture line-mixing effects over a range of pressures. The simulated spectral absorbance with no line mixing is illustrated for reference.

damental bands near 4.2 μm. Experiments were conducted over a wide range of temperatures, 1200–3000 K, utilizing a shock tube facility. To the authors' knowledge, this work represents the first experimental study of these very high rotational energy transitions (E'' = 3920–8090 cm^{-1}), extending the spectroscopic knowledge base of temperature-dependent broadening for CO_2. With broadening parameters established, a modified exponential gap model was developed to capture the thermodynamic scaling of the relaxation matrix, proportional to state-specific collisional transfer rates associated with line mixing. The line-mixing model developed in this work is shown to accurately simulate the bandhead spectral domain (2395–2398 cm^{-1}) over a wide range of temperatures and pressures,

1200–3000 K and 16.5–58.3 atm, relevant to combustion and planetary entry.

5.6 Uncertainty analysis

The uncertainty analysis presented here follows the analysis presented in the Appendix of Bendana et al [43], with added discussion for inferring the properties for the lines other than those which were directly measured. The broadening parameters reported in Table 5.1 and the MEG law coefficients reported in Table 5.2 are provided with uncertainty estimates, the calculations of which are detailed in this Appendix. Unless otherwise noted, we follow the Taylor series method (TSM) of uncertainty propagation [76], in which the uncertainty of a variable r, Δr, is given by:

$$(\Delta r)^2 = \left(\frac{\partial r}{\partial x_1}\Delta x_1\right)^2 + \left(\frac{\partial r}{\partial x_2}\Delta x_2\right)^2 + \cdots \tag{5.17}$$

where x_i are dependent variables and Δx_i are their respective uncertainties.

5.6.1 Thermodynamic state variables

The parameters we report are determined from measurements made at various thermodynamic conditions, uncertainties of which ultimately affect the temperature- and pressure-dependence of the associated models.

In this study, uncertainty in pressure is dominated by uncertainty in the reflected shock pressure ΔP_5 due to uncertainties in the inputs to the normal shock relations. Likewise, there is uncertainty in the reflected shock temperature, ΔT_5. For the sake of brevity, the uncertainties ΔP_5 and ΔT_5 will not be discussed here in further detail; however, we note that significant contributors include uncertainties in the composition of the driven gas (from the barometric mixture preparation), uncertainties in the time-of-arrival measurements that determine shock velocity, and small uncertainties in the initial pressure P_1 and temperature T_1. Further information regarding uncertainties in reflected shock conditions can

be found in the work by Campbell et al [120].

5.6.2 Broadening coefficient

The uncertainties in collisional broadening coefficient $\gamma_{A-B}(T_0)$ (for absorber A by perturber B), $\Delta\gamma_{A-B}(T_0)$, and temperature-dependent exponent, Δn_{A-B}, are determined by applying a linear regression to the natural logarithm of Eq. (5.6). In this case, the standard errors of the slopes and intercepts of the fitted lines are Δn_{A-B} and $\Delta\gamma_{A-B}(T_0)$, respectively. In our linear regressions, we follow the approach of York et al [126], incorporating variable uncertainties in both x and y to provide slope and intercept standard errors more reflective of variable measurement quality amongst the data. This allows us to utilize measurements from both the shock tube described in this manuscript as well as values estimated from the work of Thibault [100] in the same regression (as shown in Fig. 5.6), despite that each of the experiments utilized a different facility and has different measurement uncertainties.

As mentioned in Section 5.4.1, we estimated γ for high J transitions at 765 K by performing a linear regression on values of γ reported by Thibault [100] validated for lower J transitions (J = 51–100). This estimate assumes a linear dependence of γ on J for $J \geq 51$. The regression, which is weighted according to the reported measurement uncertainty, is shown in Fig. 5.12. Since the data are extrapolated, uncertainties in estimated γ, $\Delta\gamma$, are conservatively calculated by summing in quadrature the nearest reported measurement uncertainty ($\Delta\gamma_{meas}$ for J = 100) and the variation resulting from uncertainty in the linear regression, $\Delta\gamma_{reg}$:

$$\Delta\gamma_{J\geq 100} = \sqrt{(\Delta\gamma_{meas})^2 + (\Delta\gamma_{reg})^2} \tag{5.18}$$

Values of $\Delta\gamma_{reg}$ at 765 K for J = 101–145 (examples shown in Fig. 5.6) are determined by varying the possible regressions to determine a variation in possible γ which still reproduce measured γ for J = 51–100 constrained to within the 2σ reported

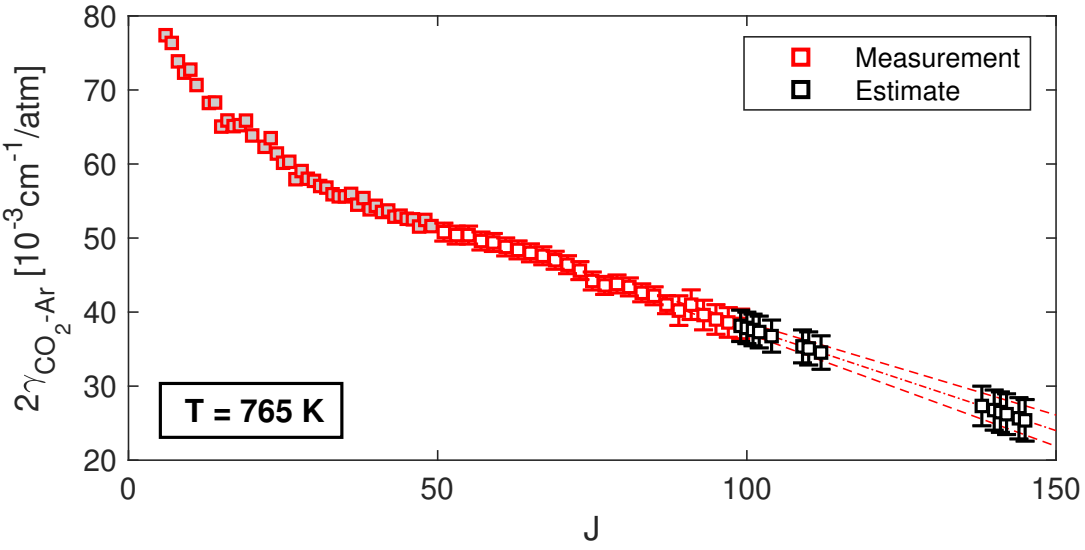

Figure 5.12: Estimation of γ and $\Delta\gamma$ at 765 K for high J transitions with measurements of Thibault [100]. Measured values (open red markers with error bars) used in regression (dashed-dot line) shown with regression uncertainty (dashed lines) and estimated values (open black markers with error bars).

measurement uncertainty. This span is noted by dashed lines in Fig. 5.12.

$\Delta\gamma_{A-B}(T_0)$ and Δn_{A-B} have uncertainty dependence on ΔT (discussed previously) and $\Delta\gamma_{A-B}(T)$. We can determine $\Delta\gamma_{A-B}(T)$ by applying Eq. (5.17) to Eq. (5.5) after rearranging to solve for $\gamma_{A-B}(T)$:

$$\begin{aligned}\left(\frac{\Delta\gamma_{A-B}(T)}{\gamma_{A-B}(T)}\right)^2 = &\left(\frac{\Delta(\Delta\upsilon_C)}{2PX_B}\right)^2 + \left(\frac{\Delta\upsilon_C\Delta P}{2P^2X_B}\right)^2 \\ &+ \left(\frac{\Delta\upsilon_C\Delta X_B}{2PX_B^2} - \frac{\Delta X_B}{X_B}\sum_C X_C\gamma_{A-C}(T)\right)^2 \\ &+ \left(\frac{1}{X_B}\sum_C \Delta X_C\gamma_{A-C}(T)\right)^2 + \left(\frac{1}{X_B}\sum_C X_C\Delta\gamma_{A-C}(T)\right)^2\end{aligned} \tag{5.19}$$

Eq. (5.19) describes the uncertainty dependence of the broadening coefficient of absorber A by perturber B, $\gamma_{A-B}(T)$, on the uncertainties in collisional width $\Delta\upsilon_C$, total pressure P, mole fraction of perturber B, X_B, and broadening influences of any other perturbers C (which includes self-broadening by A). When considering only a single perturber B, as in this study, $C = A$ to account for the influence

of self-broadening. ΔP is determined from ΔP_5, and mole fraction uncertainties ΔX_i are determined based on the barometric mixture preparation uncertainties. Collisional width $\Delta\nu_C$ is determined from a Voigt fit of the measured absorbance spectra, and so $\Delta(\Delta\nu_C)$ is estimated by multiplying the maximum residual of the Voigt fit by $\Delta\nu_C$, typically less than 3%.

Thus, the uncertainty dependencies of $\Delta\gamma_{A-B}(T_0)$ and Δn_{A-B} are all accounted for. For interpolated values of $\gamma_{A-B}(T)$ between J of 113–137 which were not directly measured (noted with superscript [a] in Table 5.1), $\Delta\gamma_{A-B}(T)/\gamma_{A-B}(T)$ was assumed to be the same as the largest $\Delta\gamma_{A-B}(T)/\gamma_{A-B}(T)$ calculated for directly measured transitions; in this study, approximately 9%.

5.6.3 MEG law coefficients

The MEG coefficients $a_1(T)$, a_2, and a_3 for each experiment are empirically determined by a nonlinear least-squares fit so their uncertainties cannot be interpreted as meaningfully through physical relationships as described by Eq. (5.17). Therefore, we estimate uncertainties for these coefficients in a manner consistent with how the model will be used; i.e., to accurately simulate absorption spectra in the range of thermodynamic conditions described in this work. The uncertainties in $a_1(T)$, a_2 and a_3 for each high-pressure shock tube experiment were inferred by varying the wavenumber range over which the least-squares fit described in Section 5.4.2 was implemented. The differences between the values of a_i determined from simulating the wavelength range of the measured experiment (2396–2398 cm^{-1}) and the values of a_i determined from simulating the wavelength range of the $(00^00 \rightarrow 00^01)$ band before overlapping with the other band (2385–2398 cm^{-1}) were taken to conservatively estimate Δa_i. This represents the uncertainty associated with using experimental data gathered from a limited spectral range to model the line mixing behavior of the entire band.

The uncertainties for $a_1(T)$, $\Delta a_1(T)$, are shown as error bars in Fig. 5.10. To-

gether with ΔT, these are used in the linear regression determination of $a_1(T_0)$ and m to obtain their respective uncertainties $\Delta a_1(T_0)$ and Δm using the same approach of York et al [126] as described for $\Delta\gamma_{A-B}(T_0)$ and Δn_{A-B}.

5.7 Supplementary Material

Table 5.3: Shock tube experimental conditions for Ar-broadening and line-mixing measurements for the CO_2 $\nu_3(0 \rightarrow 1)$ bands

ν [μm]	Temperature [K]	Pressure [atm]
4.17[a]	1370.32	0.42
4.17[a]	1559.14	0.35
4.17[a]	1740.59	0.50
4.17[a]	2007.02	0.53
4.17[a]	2198.26	0.44
4.17[a]	2518.39	0.55
4.17[a]	2744.43	0.53
4.17[a]	2859.77	0.36
4.19[a]	1248.85	0.62
4.19[a]	1558.19	0.80
4.19[a]	1787.65	0.80
4.19[a]	2118.88	0.76
4.19[a]	2482.74	0.60
4.19[a]	2636.52	0.65
4.19[a]	2840.02	0.52
4.17[b]	2021.64	22.36
4.17[b]	2228.93	33.77
4.17[b]	2359.57	16.52
4.17[b]	2376.15	23.46
4.17[b]	2441.44	32.50
4.17[b]	2492.94	36.43
4.17[b]	2542.57	18.97
4.17[b]	2571.17	58.25
4.17[b]	2665.14	45.19
4.17[b]	2692.79	35.28
4.17[b]	2726.98	37.77
4.17[b]	2879.59	35.21
4.17[b]	2893.98	25.80

[a] Low-pressure shocks for broadening measurements
[b] High-pressure shocks for line mixing

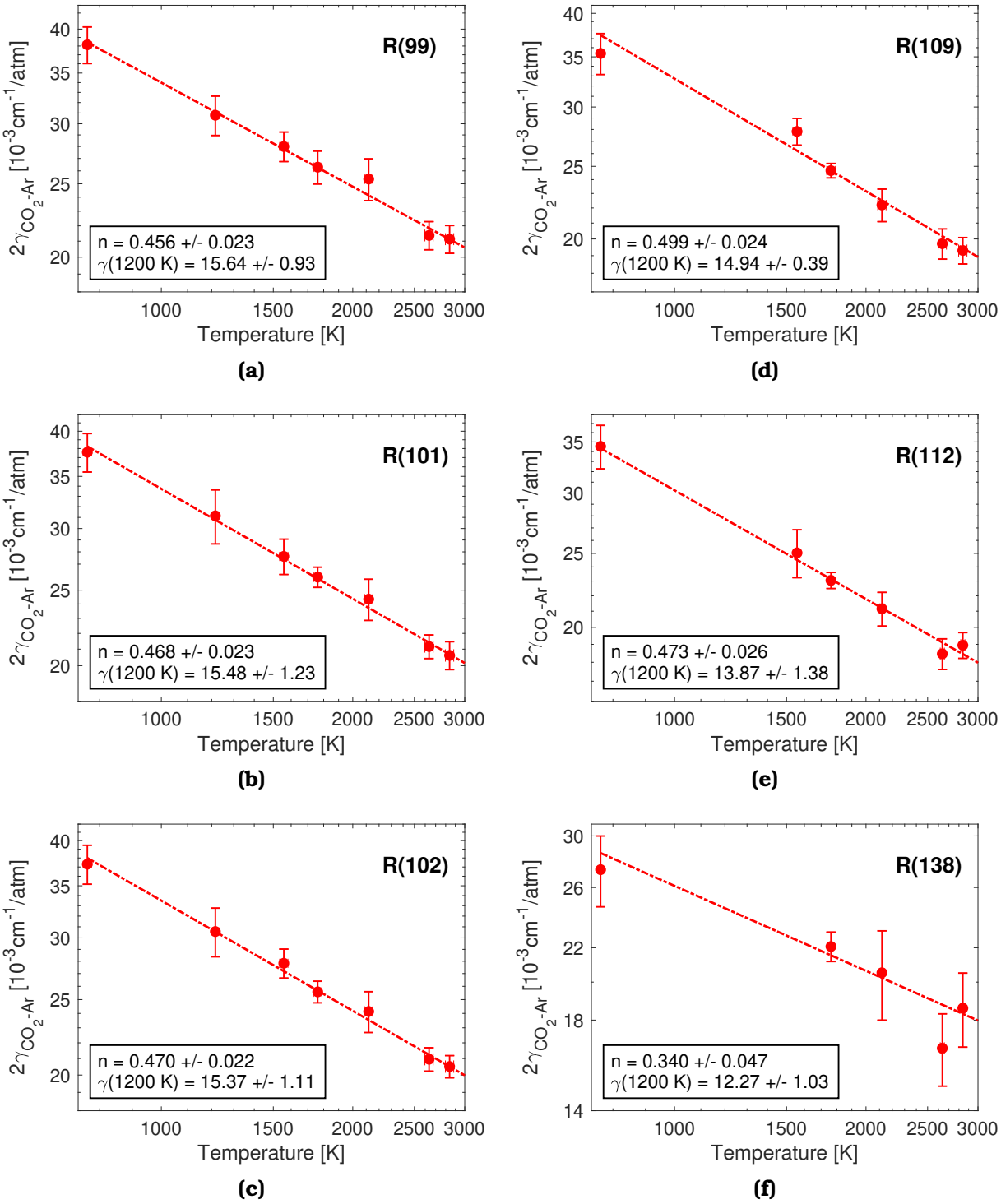

Figure 5.13: CO_2-Ar broadening coefficients and temperature exponents for $\nu(010 \rightarrow 011)$ bandhead (a) R(99), (b) R(101), (c) R(102), (d) R(109), (e) R(112), and (f) R(138) with power-law fits for 765–3000 K. Units of $\gamma(1200\ \mathrm{K})$ given in [10^{-3} $\mathrm{cm^{-1}atm^{-1}}$].

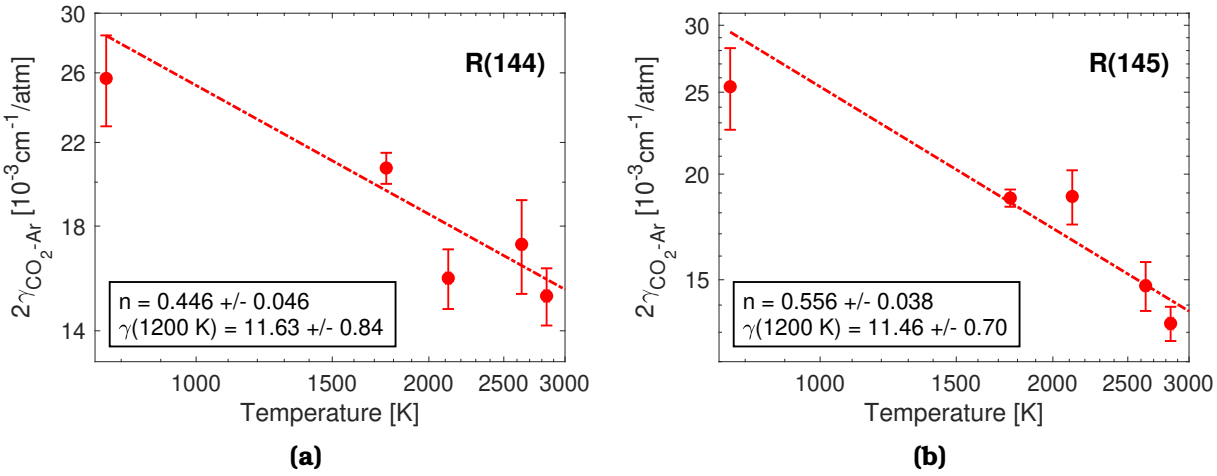

Figure 5.14: CO_2-Ar broadening coefficients and temperature exponents for $\nu(010 \rightarrow 011)$ bandhead (a) R(144) and (b) R(145) with power-law fits for 765–3000 K. Units of γ(1200 K) given in [10^{-3} $cm^{-1}atm^{-1}$].

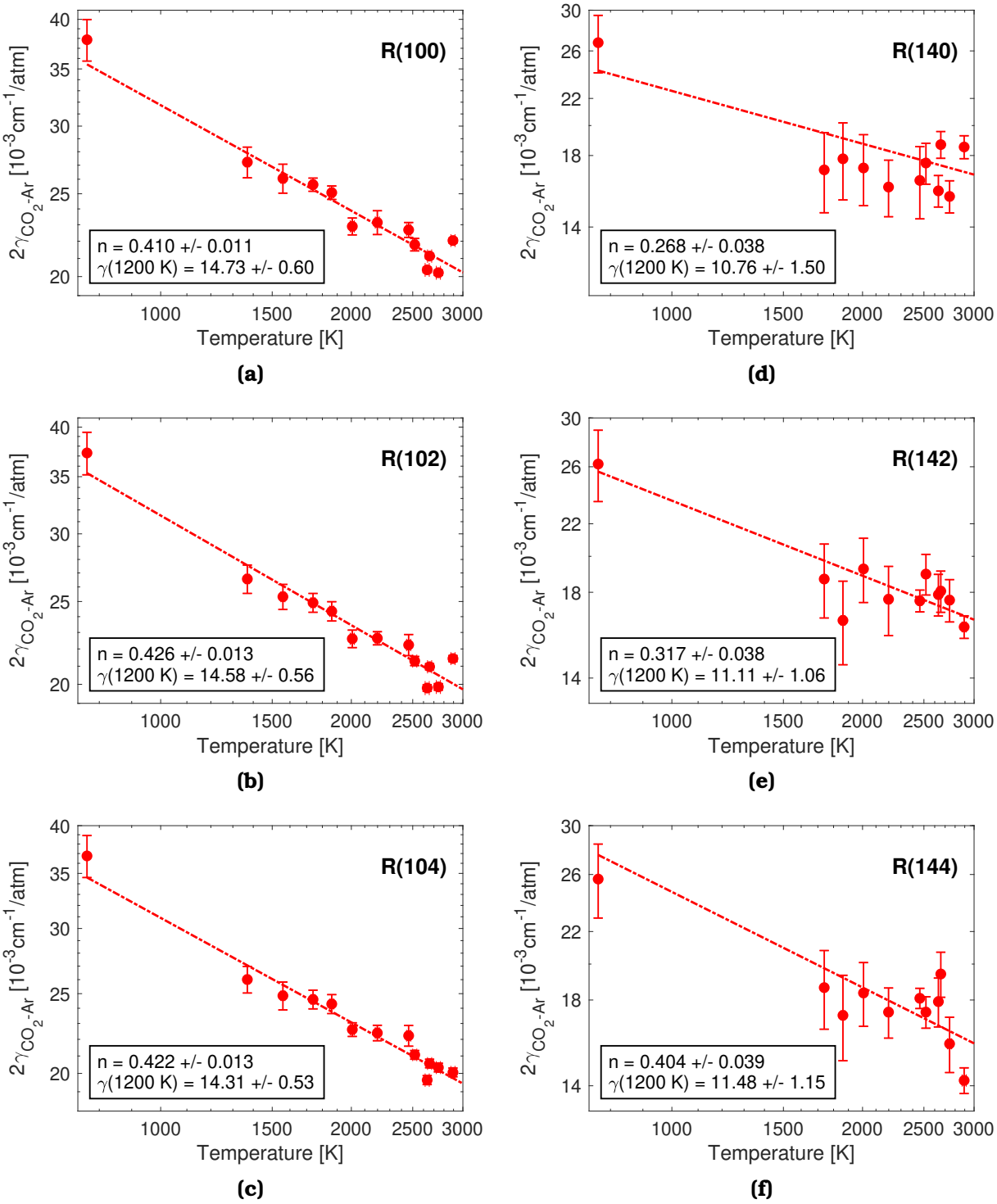

Figure 5.15: CO_2-Ar broadening coefficients and temperature exponents for $\nu(000 \rightarrow 001)$ bandhead (a) R(100), (b) R(102), (c) R(104), (d) R(140), (e) R(142), and (f) R(144) with power-law fits for 765–3000 K. Units of γ(1200 K) given in [10^{-3} $cm^{-1}atm^{-1}$].

5.8 Line mixing and broadening of carbon monoxide at high temperatures and high pressures

In addition to CO_2, line mixing and broadening of carbon monoxide has been studied in depth as a part of developing a novel sensing strategy, which exploits spectral narrowing effects of line mixing to extend pressure capability of LAS. Temperature-dependent line mixing and line broadening parameters of CO were empirically-determined for 17 rovibrational transitions, R(42)–R(58), in the $v(1 \rightarrow 3)$

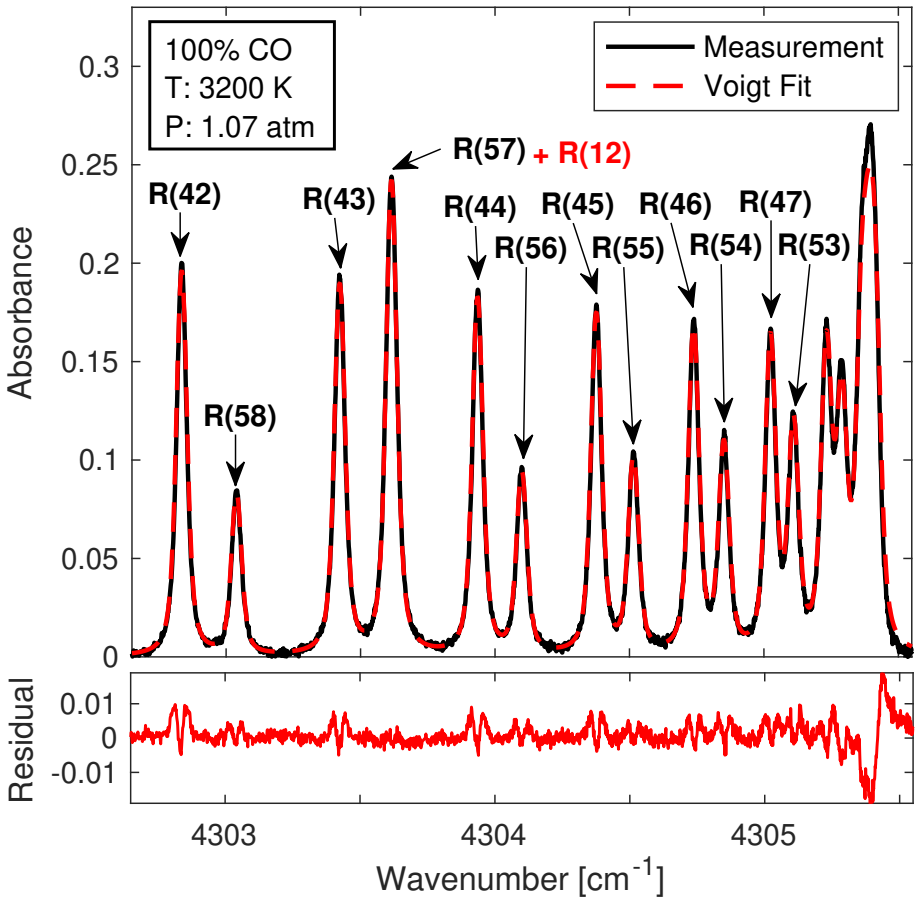

Figure 5.16: *(top)* Absorbance of the first overtone bandhead of CO at 3200 K and 1.07 atm with corresponding Voigt fits. *(bottom)* Residuals of the Voigt fit, showing larger disagreement at the bandhead.

bandhead of carbon monoxide near 2.3 μm. Collisional effects on the high rotational energy lines (E'' = 5500–8600 cm^{-1}) in the R-branch were studied over a range of temperatures from 1200–3750 K in a shock tube and heated gas cell. Measured spectra comprising the target lines in Ar and CO bath gases were fit with Voigt profiles at near-atmospheric pressures to determine line-broadening coefficients, with temperature dependence accounted by a power law. A representative single-scan absorbance measurement from a shock tube experiment with corresponding Voigt line fits is presented in Fig. 5.16. The broadening coefficient, $\gamma_{CO-B}(T)$, for each transition, was set as the free parameter and determined by using a least squares fitting routine. At high temperatures and low pressures

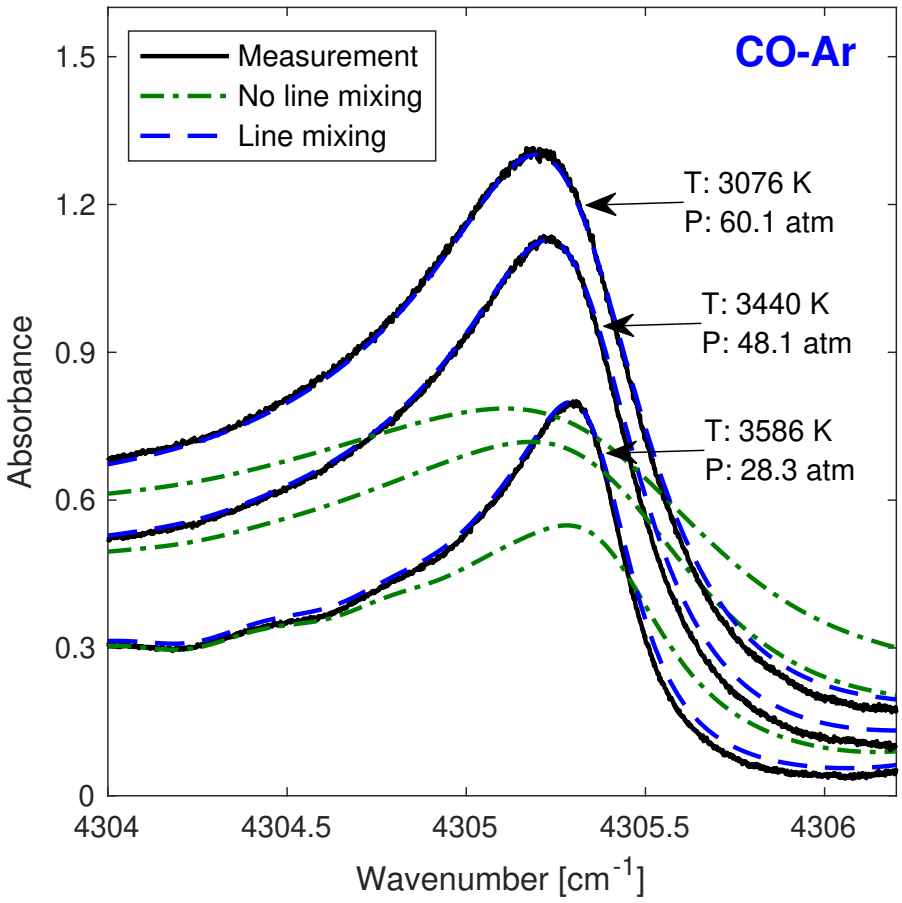

Figure 5.17: CO-Ar: measured spectral absorbance compared to the developed MEG model used capture line-mixing effects over a range of pressures. The simulated spectral absorbance with no line mixing is illustrated for reference.

both CO-broadening and Ar-broadening experiments exhibited some evidence of collisional narrowing (gull-wing residual) likely due to a reduction in Doppler broadening from velocity-changing collisions [124]. Evidence of line mixing effects can also be observed where the Voigt lineshape summation is unable to properly fit the measured absorbance near the bandhead.

With line broadening established, line-mixing effects were examined at elevated pressures up to 60 atm at similar temperatures, reflecting conditions in high-pressure combustion environments. A modified exponential gap model for line mixing was developed to capture the pressure and temperature dependence of collisional transfer rates for the bandhead region using the relaxation matrix formalism. The thermodynamic scaling of the developed line-mixing model is shown in Fig. 5.17. The line-mixing model developed in this work quantitatively resolves the spectral domain over a range of extreme temperatures and pressures, 2000–3600 K and 5–60 atm, relevant to rocket combustion. Greater details on this synergistic effort can be found in the pending dissertation of Fabio Bendana (UCLA).

CHAPTER 6

Conclusion and future research direction

The research presented here demonstrates advancements in mid-infrared laser absorption spectroscopy for sensing temperature and carbon oxide (CO and CO_2) in harsh high-pressure and high-temperature environments, with specific applications to rocket combustion devices. First, a new mid-infrared wavelength of carbon monoxide was selected and probed to enhance pressure capability and enable a first application of mid-IR LAS to rocket systems. To further extend the pressure capability, a novel sensing strategy which exploits the band narrowing effects of line mixing at the bandheads of carbon oxide (CO and CO_2), has been developed in a shock tube and translated to field measurements. This sensing strategy was deployed to high-pressure liquid rocket combustor with CH_4/GOx and RP-2/GOx propellant combinations and demonstrated temperature measurement up to 70 bar, CO mole fraction measurement up to 105 bar and CO_2 mole fraction measurement up to 83 bar. In addition to the sensor development process, an extensive efforts were devoted to overcome challenges associated with harsh environments of the rocket combustor. A purge system was integrated into the engine to clear the optical path obstructed by soots and supplementary structures were manufactured to secure and protect fiber, collimation optics, and detector assembly from the environmental noise. In total, primary contributions from the author to the field of laser absorption diagnostics include fundamental study in line mixing effect, additions to CO_2 high-temperature spectroscopic databases, and significant extensions in pressure capability of laser absorption spectroscopy by developing a novel sensing strategy, exploiting the line mixing effects. The

rocket combustion sensing applications were also novel and proved the theoretical capability of the new sensing techniques in practical systems.

6.1 Future research directions

This section briefly describes future potential work associated with the over-arching research endeavor.

6.1.1 Coarse spatially-resolved measurements

All field measurements in this research were conducted at the furthest downstream location of the rocket combustion chamber, shown in Figure 6.1. The rocket engine utilized in the experiments is composed of multiple modular sections, in which the last section allows for optical access. This section can be swapped with engine blocks at three different locations along the chamber. A future research goal involves conducting measurements at these locations to spatially resolve CO, CO_2, and temperature throughout the length of the chamber. These measurements will enable studies of direct chemical-to-thermal energy conversion during combustion, providing a basis to assess performance in the rocket combustor. Other researchers have conducted computational studies for the rocket combustor, and

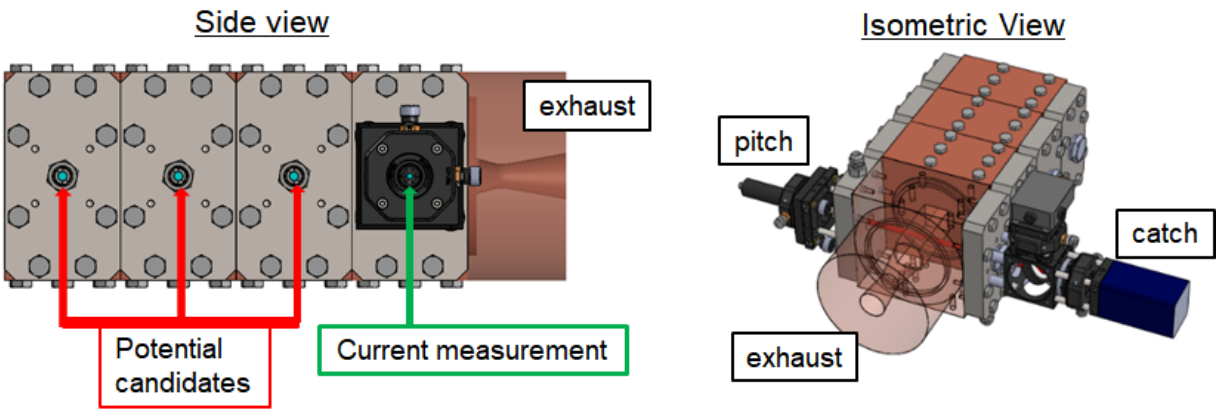

Figure 6.1: Test hardware schematic for single-injector-element rocket combustor at AFRL Edwards with integrated laser absorption sensor for CO

these measurements would allow them to anchor and improve computational model.

6.1.2 Multi-bandhead temperature sensing strategy

Temperature measurements from previous studies have been limited to 70 bar due to extreme pressure broadening in rovibrational transitions near 4.9 μm. Differential absorption of targeted regions decreased, causing the WMS signal to eventually diminish. In contrast, measurements targeting two bandheads near 2.3 μm and 4.2 μm showed promising results, where spectral narrowing effects from the line-mixing amplified the signal. The next goal will be to target additional bandhead regions rather than the fundamental vibrational lines near 4.9 μm in order to successfully implement two color thermometry. There are a few potential candidates shown in 6.2.

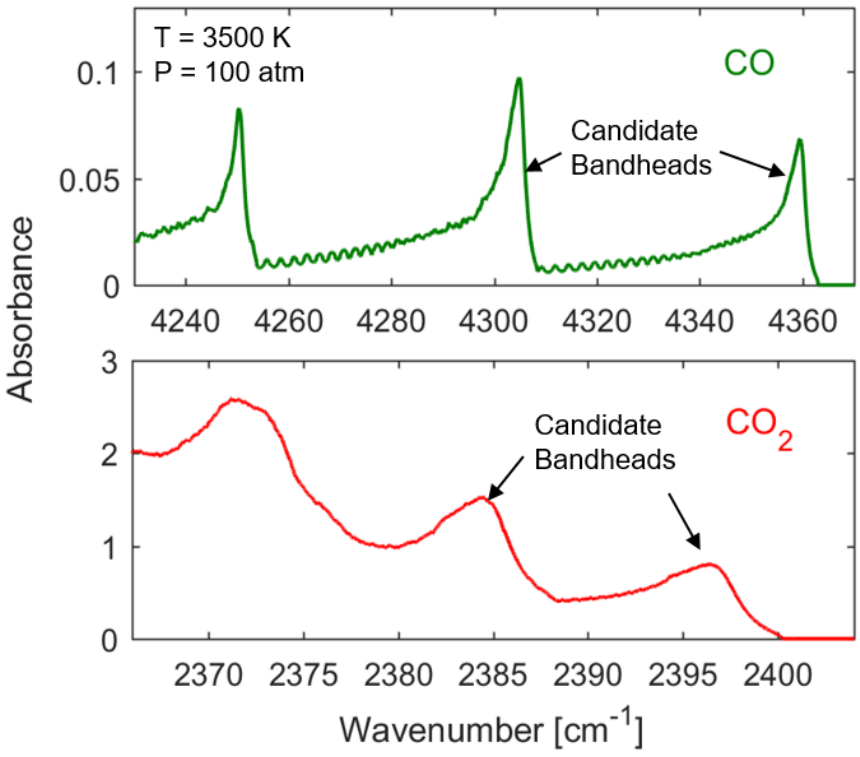

Figure 6.2: Absorbance simulations of CO and CO_2 at high temperature (3500K) and high pressure (100 atm) indicating the distinct bandhead features at rocket conditions

To ensure temperature measurement capability of the proposed novel sensing strategy, bandheads of CO have been investigated in greater details. In addition to previously utilized bandhead near 4305 cm^{-1} ($\nu(1 \rightarrow 3)$), bandhead near 4360 cm^{-1} ($\nu(0 \rightarrow 2)$) can be selected as the second targeted absorption region. The temperature sensitivity of the local peak absorbance ratio, R = $\alpha(\lambda_1)/\alpha(\lambda_2)$, were evaluated as a function of temperature, presented in fig. 6.3. The temperature sensitivity was evaluated at two pressure conditions and demonstrated not only high sensitivity for both conditions but also a surprising trend, where sensitivity increases with pressure. According to this simulation, a novel multi-bandhead sensing strategy of exploiting line-mixing effects on two bandheads is expected to extend pressure capability of temperature measurement in rocket combustion chambers.

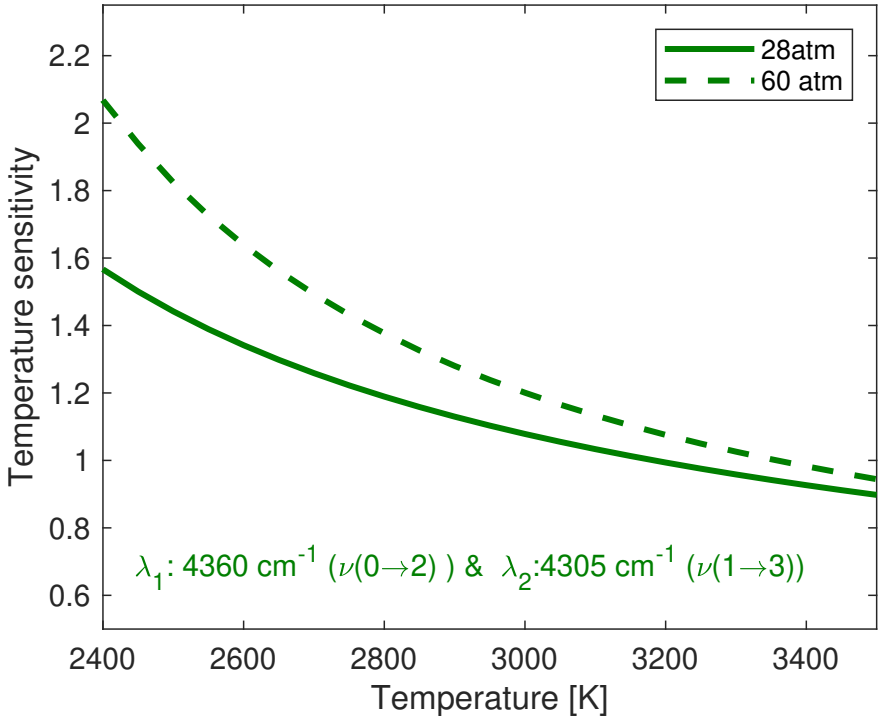

Figure 6.3: Temperature sensitivity (dR/R)/(dT/T) of the multi-bandhead sensing strategy at elevated pressures

Bibliography

[1] C. S. Goldenstein, R. M. Spearrin, J. B. Jeffries, and R. K. Hanson, "Infrared laser absorption sensors for multiple performance parameters in a detonation combustor," *Proceedings of the Combustion Institute*, vol. 35, no. 3, pp. 3739–3747, 2015.

[2] D. Mattison, J. Jeffries, R. Hanson, R. Steeper, S. De Zilwa, J. Dec, M. Sjoberg, and W. Hwang, "In-cylinder gas temperature and water concentration measurements in HCCI engines using a multiplexed-wavelength diode-laser system: Sensor development and initial demonstration," *Proceedings of the Combustion Institute*, vol. 31, pp. 791–798, 1 2007.

[3] A. McIlroy, G. McRae, V. Sick, D. L. Siebers, C. K. Westbrook, P. J. Smith, C. Taatjes, A. Trouve, A. F. Wagner, E. Rohlfing, D. Manley, F. Tully, R. Hilderbrandt, W. Green, D. Marceau, J. O'Neal, M. Lyday, F. Cebulski, T. R. Garcia, and D. Strong, "Basic Research Needs for Clean and Efficient Combustion of 21st Century Transportation Fuels," tech. rep., USDOE Office of Science (SC) (United States), 11 2006.

[4] Y. Ju, *Recent progress and challenges in fundamental combustion research*, vol. 44. 2014.

[5] A. M. Taylor, "Science review of internal combustion engines," *Energy Policy*, vol. 36, pp. 4657–4667, 12 2008.

[6] D. K. Srivastava, A. K. Agarwal, A. Datta, and R. K. Maurya, *Advances in Internal Combustion Engine Research*. Energy, Environment, and Sustainability, Singapore: Springer Singapore, 2018.

[7] F. Wåhlin, "Experimental Investigation of Impinging Diesel Sprays for HCCI Combustion," *Combustion*, no. February, 2006.

[8] H. M. Tobib, A. A. Hairuddin, N. A. Aziz, M. M. Noor, J. Zulkiple, and M. A. A. Mossa, "An experimental investigation on the combustion and performance of an HCCI-DI engine," in *AIP Conference Proceedings*, vol. 2059, p. 020010, 2019.

[9] S. Gowthaman and A. Sathiyagnanam, "Effects of charge temperature and fuel injection pressure on HCCI engine," *Alexandria Engineering Journal*, vol. 55, pp. 119–125, 3 2016.

[10] R. D. Reitz and G. Duraisamy, "Review of high efficiency and clean reactivity controlled compression ignition (RCCI) combustion in internal combustion engines," *Progress in Energy and Combustion Science*, vol. 46, pp. 12–71, 2 2015.

[11] M. N. Svrcek, S. L. Miller, and C. F. Edwards, "DIESEL SPRAY BEHAVIOR AT COMPRESSION RATIOS UP TO 100:1," *Atomization and Sprays*, vol. 20, no. 5, pp. 453–465, 2010.

[12] B. Gunston, *Jane's AERO-ENGINES*. Jane's Information Goup, 1998.

[13] T. K. Ibrahim and M. Rahman, "Effect of Compression Ratio on the Performance of Different Strategies for the Gas Turbine," *International Journal of Automotive and Mechanical Engineering*, vol. 9, pp. 1747–1757, 6 2014.

[14] T. K. Ibrahim and M. M. Rahman, "Effect of Compression Ratio on Performance of Combined Cycle Gas Turbine," *International Journal of Energy Engineering*, vol. 2, pp. 9–14, 8 2012.

[15] O. J. Haidn, "Advanced rocket engines," *Advances on propulsion technology for high-speed ...*, pp. 6–1, 2008.

[16] R. K. Hanson, R. M. Spearrin, and C. S. Goldenstein, *Spectroscopy and Optical Diagnostics for Gases*. Cham, Switzerland: Springer International Publishing, 2016.

[17] G. Kychakoff, R. D. Howe, and R. K. Hanson, "Quantitative flow visualization technique for measurements in combustion gases," *Applied Optics*, vol. 23, p. 704, 3 1984.

[18] &NA;, "Rapid Communications," *Journal of Acquired Immune Deficiency Syndromes*, vol. 21, p. 433, 12 2000.

[19] M. J. Dyer and D. R. Crosley, "Rapidly sequenced pair of two-dimensional images of OH laser-induced fluorescence in a flame," *Optics Letters*, vol. 9, p. 217, 6 1984.

[20] C. Schulz, V. Sick, J. Wolfrum, V. Drewes, M. Zahn, and R. Maly, "Quantitative 2D single-shot imaging of no concentrations and temperatures in a transparent SI engine," *Symposium (International) on Combustion*, vol. 26, no. 2, pp. 2597–2604, 1996.

[21] S. Einecke, C. Schulz, and V. Sick, "Measurement of temperature, fuel concentration and equivalence ratio fields using tracer LIF in IC engine combustion," *Applied Physics B*, vol. 71, pp. 717–723, 11 2000.

[22] D. A. Rothamer, J. A. Snyder, R. K. Hanson, and R. R. Steeper, "Optimization of a tracer-based PLIF diagnostic for simultaneous imaging of EGR and temperature in IC engines," *Applied Physics B*, vol. 99, pp. 371–384, 4 2010.

[23] F. Grisch, P. Bouchardy, and W. Clauss, "CARS thermometry in high pressure rocket combustors," *Aerospace Science and Technology*, vol. 7, pp. 317–330, 6 2003.

[24] I. A. Stenhouse, D. R. Williams, J. B. Cole, and M. D. Swords, "CARS measurements in an internal combustion engine," *Applied Optics*, vol. 18, p. 3819, 11 1979.

[25] J. Smith, D. Klimenko, W. Clauss, and W. Mayer, "Supercritical LOX/Hydrogen Rocket Combustion Investigations Using Optical Diagnos-

tics," in *38th AIAA/ASME/SAE/ASEE Joint Propulsion Conference & Exhibit*, no. July, (Reston, Virigina), American Institute of Aeronautics and Astronautics, 7 2002.

[26] F. Grisch, E. Bertseva, M. Habiballah, E. Jourdanneau, F. Chaussard, R. Saint-Loup, T. Gabard, and H. Berger, "CARS spectroscopy of CH4 for implication of temperature measurements in supercritical LOX/CH4 combustion," *Aerospace Science and Technology*, vol. 11, pp. 48–54, 1 2007.

[27] M. P. Thariyan, A. H. Bhuiyan, S. E. Meyer, S. V. Naik, J. P. Gore, and R. P. Lucht, "Dual-pump coherent anti-Stokes Raman scattering system for temperature and species measurements in an optically accessible high-pressure gas turbine combustor facility," *Measurement Science and Technology*, vol. 22, p. 015301, 1 2011.

[28] E. Schlosser, T. Fernholz, H. Teichert, and V. Ebert, "In situ detection of potassium atoms in high-temperature coal-combustion systems using near-infrared-diode lasers," *Spectrochimica Acta - Part A Molecular and Biomolecular Spectroscopy*, vol. 58, no. 11, pp. 2347–2359, 2002.

[29] K. Sun, R. Sur, X. Chao, J. B. Jeffries, R. K. Hanson, R. J. Pummill, and K. J. Whitty, "TDL absorption sensors for gas temperature and concentrations in a high-pressure entrained-flow coal gasifier," *Proceedings of the Combustion Institute*, vol. 34, pp. 3593–3601, 1 2013.

[30] R. Sur, K. Sun, J. B. Jeffries, R. K. Hanson, R. J. Pummill, T. Waind, D. R. Wagner, and K. J. Whitty, "TDLAS-based sensors for in situ measurement of syngas composition in a pressurized, oxygen-blown, entrained flow coal gasifier," *Applied Physics B: Lasers and Optics*, vol. 116, no. 1, pp. 33–42, 2014.

[31] G. Rieker, H. Li, X. Liu, J. Liu, J. Jeffries, R. Hanson, M. Allen, S. Wehe, P. Mulhall, H. Kindle, A. Kakuho, K. Sholes, T. Matsuura, and S. Takatani,

"Rapid measurements of temperature and H2O concentration in IC engines with a spark plug-mounted diode laser sensor," *Proceedings of the Combustion Institute*, vol. 31, pp. 3041–3049, 1 2007.

[32] O. Witzel, A. Klein, C. Meffert, S. Wagner, S. Kaiser, C. Schulz, and V. Ebert, "VCSEL-based, high-speed, in situ TDLAS for in-cylinder water vapor measurements in IC engines," *Optics Express*, vol. 21, p. 19951, 8 2013.

[33] S. Bürkle, L. Biondo, C.-P. Ding, R. Honza, V. Ebert, B. Böhm, and S. Wagner, "In-Cylinder Temperature Measurements in a Motored IC Engine using TDLAS," *Flow, Turbulence and Combustion*, vol. 101, pp. 139–159, 7 2018.

[34] L. A. Kranendonk, J. W. Walewski, T. Kim, and S. T. Sanders, "Wavelength-agile sensor applied for HCCI engine measurements," *Proceedings of the Combustion Institute*, vol. 30, pp. 1619–1627, 1 2005.

[35] S. T. Sanders, J. A. Baldwin, T. P. Jenkins, D. S. Baer, and R. K. Hanson, "Diode-laser sensor for monitoring multiple combustion parameters in pulse detonation engines," *Proceedings of the Combustion Institute*, vol. 28, no. 1, pp. 587–594, 2000.

[36] D. Mattison, M. Oehlschlaeger, C. Morris, Z. Owens, E. Barbour, J. Jeffries, and R. Hanson, "Evaluation of pulse detonation engine modeling using laser-based temperature and OH concentration measurements," *Proceedings of the Combustion Institute*, vol. 30, pp. 2799–2807, 1 2005.

[37] R. M. Spearrin, C. S. Goldenstein, J. B. Jeffries, and R. K. Hanson, "Quantum cascade laser absorption sensor for carbon monoxide in high-pressure gases using wavelength modulation spectroscopy," *Applied Optics*, vol. 53, pp. 1938–1946, 3 2014.

[38] S. T. Sanders, D. W. Mattison, L. Ma, J. B. Jeffries, and R. K. Hanson, "Wavelength-agile diode-laser sensing strategies for monitoring gas properties

in optically harsh flows: application in cesium-seeded pulse detonation engine," *Optics Express*, vol. 10, p. 505, 6 2002.

[39] L. A. Kranendonk, X. An, A. W. Caswell, R. E. Herold, S. T. Sanders, R. Huber, J. G. Fujimoto, Y. Okura, and Y. Urata, "High speed engine gas thermometry by Fourier-domain mode-locked laser absorption spectroscopy," *Optics Express*, vol. 15, p. 15115, 11 2007.

[40] A. W. Caswell, T. Kraetschmer, K. Rein, S. T. Sanders, S. Roy, D. T. Shouse, and J. R. Gord, "Application of time-division-multiplexed lasers for measurements of gas temperature and CH4 and H2O concentrations at 30 kHz in a high-pressure combustor," *Applied Optics*, vol. 49, p. 4963, 9 2010.

[41] L. Wehr, W. Meier, P. Kutne, and C. Hassa, "Single-pulse 1D laser Raman scattering applied in a gas turbine model combustor at elevated pressure," *Proceedings of the Combustion Institute*, vol. 31, pp. 3099–3106, 1 2007.

[42] C. S. Goldenstein, R. M. Spearrin, J. B. Jeffries, and R. K. Hanson, "Infrared laser-absorption sensing for combustion gases," *Progress in Energy and Combustion Science*, vol. 60, pp. 132–176, 5 2017.

[43] F. A. Bendana, D. D. Lee, C. Wei, D. I. Pineda, and R. M. Spearrin, "Line mixing and broadening in the v(1→3) first overtone bandhead of carbon monoxide at high temperatures and high pressures," *Journal of Quantitative Spectroscopy and Radiative Transfer*, vol. 239, p. 106636, 12 2019.

[44] L. Rothman, I. Gordon, R. Barber, H. Dothe, R. Gamache, A. Goldman, V. Perevalov, S. Tashkun, and J. Tennyson, "HITEMP, the High-Temperature Molecular Spectroscopic Database," *Journal of Quantitative Spectroscopy and Radiative Transfer*, vol. 111, pp. 2139–2150, 10 2010.

[45] D. D. Lee, F. A. Bendana, S. A. Schumaker, and R. M. Spearrin, "Wavelength modulation spectroscopy near 5 μ m for carbon monoxide sensing in a

high-pressure kerosene-fueled liquid rocket combustor," *Applied Physics B: Lasers and Optics*, vol. 124, p. 77, 5 2018.

[46] D. D. Lee, F. A. Bendana, and M. Spearrin, "Laser Absorption Spectroscopy of Carbon Monoxide near 4.97 μm for Temperature and Species Measurements in Hydrocarbon-Fueled Rockets," in *2018 AIAA Aerospace Sciences Meeting*, no. 210059, (Reston, Virginia), pp. 1–10, American Institute of Aeronautics and Astronautics, 1 2018.

[47] P. G. Hill and C. R. Peterson, *Mechanics and Thermodynamics of Propulsion*. Reading, MA: Addison-Wesley Publishing Co, 2nd ed., 1992.

[48] A. W. Caswell, S. T. Sanders, and M. J. Chiaverini, "Swept-Wavelength Laser Absorption Tomography for Imaging Rocket Plume Gas Properties," in *41st AIAA/ASME/SAE/ASEE Joint Propulsion Conference & Exhibit*, 2005.

[49] A. S. Makowiecki, T. R. Hayden, M. R. Nakles, N. H. Pilgram, N. A. MacDonald, W. A. Hargus, and G. B. Rieker, "Wavelength modulation spectroscopy for measurements of temperature and species concentration downstream from a supersonic nozzle," in *53rd AIAA/SAE/ASEE Joint Propulsion Conference*, (Reston, Virginia), American Institute of Aeronautics and Astronautics, 7 2017.

[50] J. Locke, S. Pal, R. Woodward, and R. Santoro, "Diode Laser Absorption Spectroscopy Measurements in a Gaseous Hydrogen / Oxygen Rocket," *49th AIAA Aerospace Sciences Meeting including the New Horizons Forum and Aerospace Exposition*, 1 2011.

[51] H. Zeng, F. Li, X. Yu, D. Ou, and L. Chen, "Measurement of multispecies concentration and gas temperature in an ammonium-dinitramide-based thruster by tunable diode lasers," *Applied Optics*, vol. 57, pp. 1321–1330, 2 2018.

[52] E. B. Coy, "A Method for Eliminating Beam Steering Error for the Modulated Absorption-Emission Thermometry Technique," *53rd AIAA Aerospace Sciences Meeting*, pp. 1–12, 1 2015.

[53] C. S. Goldenstein, V. A. Miller, R. Mitchell Spearrin, and C. L. Strand, "SpectraPlot.com: Integrated spectroscopic modeling of atomic and molecular gases," *Journal of Quantitative Spectroscopy and Radiative Transfer*, vol. 200, pp. 249–257, 10 2017.

[54] M. G. Allen, "Diode laser absorption sensors for gas-dynamic and combustion flows," *Measurement Science and Technology*, vol. 9, pp. 545–562, 4 1998.

[55] G. B. Rieker, J. B. Jeffries, and R. K. Hanson, "Calibration-free wavelength-modulation spectroscopy for measurements of gas temperature and concentration in harsh environments," *Applied Optics*, vol. 48, pp. 5546–5560, 10 2009.

[56] R. M. Spearrin, W. Ren, J. B. Jeffries, and R. K. Hanson, "Multi-band infrared CO2 absorption sensor for sensitive temperature and species measurements in high-temperature gases," *Applied Physics B*, vol. 116, pp. 855–865, 9 2014.

[57] J. M. Hartmann, L. Rosenmann, M. Y. Perrin, and J. Taine, "Accurate calculated tabulations of CO line broadening by H2O, N2, O2, and CO2 in the 200–3000-K temperature range," *Applied Optics*, vol. 27, p. 3063, 8 1988.

[58] H. Li, G. B. Rieker, X. Liu, J. B. Jeffries, and R. K. Hanson, "Extension of wavelength-modulation spectroscopy to large modulation depth for diode laser absorption measurements in high-pressure gases," *Applied Optics*, vol. 45, no. 5, pp. 1052–1061, 2006.

[59] K. Sun, X. Chao, R. Sur, C. S. Goldenstein, J. B. Jeffries, and R. K. Hanson, "Analysis of calibration-free wavelength-scanned wavelength modulation

spectroscopy for practical gas sensing using tunable diode lasers," *Measurement Science and Technology*, vol. 24, no. 12, p. 125203, 2013.

[60] J. M. Kriesel, N. Gat, B. E. Bernacki, R. L. Erikson, B. D. Cannon, T. L. Myers, C. M. Bledt, and J. A. Harrington, "Hollow core fiber optics for mid-wave and long-wave infrared spectroscopy," in *Proceedings of SPIE - The International Society for Optical Engineering*, vol. 8018, p. 80180V, 5 2011.

[61] J. M. Hartmann, C. Boulet, and D. Robert, *Collisional Effects on Molecular Spectra*. Elsevier, 2008.

[62] D. D. Lee, F. A. Bendana, and R. M. Spearrin, "Exploiting line mixing effects for laser absorption spectroscopy at extreme combustion conditions," in *11th U.S. National Combustion Meeting*, (Pasadena, CA), The Combustion Institute, 2019.

[63] D. D. Lee, F. A. Bendana, A. P. Nair, R. M. Spearrin, S. A. Danczyk, and W. A. Hargus, "Laser absorption of carbon dioxide at the vibrational bandhead near 4.2 μm in high-pressure rocket combustion environments," in *AIAA Scitech 2020 Forum*, no. January, (Reston, Virginia), American Institute of Aeronautics and Astronautics, 1 2020.

[64] U. Fano, "Pressure Broadening as a Prototype of Relaxation," *Physical Review*, vol. 131, pp. 259–268, 7 1963.

[65] D. D. Lee, F. A. Bendana, A. P. Nair, D. I. Pineda, and R. M. Spearrin, "Line mixing and broadening of carbon dioxide by argon in the v3 bandhead near 4.2 μm at high temperatures and high pressures," *Journal of Quantitative Spectroscopy and Radiative Transfer*, p. 107135, 6 2020.

[66] L. L. Strow and D. Reuter, "Effect of line mixing on atmospheric brightness temperatures near 15 μm," *Applied Optics*, vol. 27, p. 872, 3 1988.

[67] D. Romanini and K. K. Lehmann, "Line-mixing in the 106←000 overtone transition of HCN," *The Journal of Chemical Physics*, vol. 105, pp. 81–88, 7 1996.

[68] R. G. Gordon, "Semiclassical Theory of Spectra and Relaxation in Molecular Gases," *The Journal of Chemical Physics*, vol. 45, pp. 1649–1655, 9 1966.

[69] M. L. Koszykowski, L. A. Rahn, R. E. Palmer, and M. E. Coltrin, "Theoretical and experimental studies of high-resolution inverse Raman spectra of N2 at 1-10 atm," *Journal of Physical Chemistry*, vol. 91, pp. 41–46, 1 1987.

[70] L. Rahn, R. Palmer, M. Koszykowski, and D. Greenhalgh, "Comparison of rotationally inelastic collision models for Q-branch Raman spectra of N2," *Chemical Physics Letters*, vol. 133, pp. 513–516, 2 1987.

[71] A. Ben-Reuven, "Impact Broadening of Microwave Spectra," *Physical Review*, vol. 145, pp. 7–22, 5 1966.

[72] L. Rosenmann, J. M. Hartmann, M. Y. Perrin, and J. Taine, "Accurate calculated tabulations of IR and Raman CO2 line broadening by CO2, H2O, N2, O2 in the 300–2400-K temperature range," *Applied Optics*, vol. 27, p. 3902, 9 1988.

[73] F. A. Bendana, D. D. Lee, S. A. Schumaker, S. A. Danczyk, and R. M. Spearrin, "Cross-band infrared laser absorption of carbon monoxide for thermometry and species sensing in high-pressure rocket flows," *Applied Physics B*, vol. 125, p. 204, 11 2019.

[74] R. M. Spearrin, C. S. Goldenstein, I. A. Schultz, J. B. Jeffries, and R. K. Hanson, "Simultaneous sensing of temperature, CO, and CO2 in a scramjet combustor using quantum cascade laser absorption spectroscopy," *Applied Physics B*, vol. 117, pp. 689–698, 11 2014.

[75] B. J. McBride and S. Gordon, *Computer Program for Calculation of Complex Chemical Equilibrium Compositions and Applications*. No. January, NASA, 1996.

[76] H. W. Coleman and W. G. Steele, *Experimentation, Validation, and Uncertainty Analysis for Engineers*. Hoboken, NJ, USA: John Wiley & Sons, Inc., 3rd ed., 2009.

[77] A. P. Nair, D. D. Lee, D. I. Pineda, J. Kriesel, W. A. Hargus, J. W. Bennewitz, S. A. Danczyk, and R. M. Spearrin, "MHz Laser Absorption Spectroscopy via Diplexed RF Modulation for Pressure, Temperature, and Species in Rotating Detonation Rocket Flows," *Applied Physics B*, vol. 126, p. 138, 8 2020.

[78] B. J. McBride and S. Gordon, *Computer Program for Calculation of Complex Chemical Equilibrium Compositions and Applications*. No. January, NASA, 1996.

[79] M. Margottin-Maclou, A. Henry, and A. Valentin, "Line mixing in the Q branches of the v 1 +v 2 band of nitrous oxide and of the (11 1 0) I ←(02 2 0) band of carbon dioxide," *The Journal of Chemical Physics*, vol. 96, pp. 1715–1723, 2 1992.

[80] M. Snels, S. Stefani, D. Grassi, G. Piccioni, and A. Adriani, "Carbon dioxide opacity of the Venus atmosphere," *Planetary and Space Science*, vol. 103, pp. 347–354, 2014.

[81] T. L. Barbu, I. Vinogradov, G. Durry, O. Korablev, E. Chassefière, and J.-L. Bertaux, "TDLAS a laser diode sensor for the in situ monitoring of H2O, CO2 and their isotopes in the Martian atmosphere," *Advances in Space Research*, vol. 38, pp. 718–725, 1 2006.

[82] R. M. Spearrin, C. S. Goldenstein, J. B. Jeffries, and R. K. Hanson, "Fiber-coupled 2.7 μm laser absorption sensor for CO2 in harsh combustion

environments," *Measurement Science and Technology*, vol. 24, p. 055107, 5 2013.

[83] C. Park, J. T. Howe, R. L. Jaffe, and G. V. Candler, "Review of chemical-kinetic problems of future NASA missions, II: Mars entries," *Journal of Thermophysics and Heat Transfer*, vol. 8, no. 1, pp. 9–23, 1994.

[84] H. Takayanagi, A. Lemal, S. Nomura, and K. Fujita, "Measurements of Carbon Dioxide Nonequilibrium Infrared Radiation in Shocked and Expanded Flows," *Journal of Thermophysics and Heat Transfer*, vol. 32, pp. 483–494, 4 2018.

[85] R. Villarreal and P. L. Varghese, "Frequency-resolved absorption tomography with tunable diode lasers," *Applied Optics*, vol. 44, no. 31, pp. 6786–6795, 2005.

[86] J. J. Girard, R. M. Spearrin, C. S. Goldenstein, and R. K. Hanson, "Compact optical probe for flame temperature and carbon dioxide using interband cascade laser absorption near 4.2 μm," *Combustion and Flame*, vol. 178, pp. 158–167, 2017.

[87] X. Liu, G. Zhang, Y. Huang, Y. Wang, and F. Qi, "Two-dimensional temperature and carbon dioxide concentration profiles in atmospheric laminar diffusion flames measured by mid-infrared direct absorption spectroscopy at 4.2 μm," *Applied Physics B*, vol. 124, p. 61, 4 2018.

[88] C. Wei, D. I. Pineda, L. Paxton, F. N. Egolfopoulos, and R. M. Spearrin, "Mid-Infrared Laser Absorption Tomography for Quantitative 2D Thermochemistry Measurements in Premixed Jet Flames," *Applied Physics B*, vol. 124, p. 123, 6 2018.

[89] C. Wei, D. I. Pineda, C. S. Goldenstein, and R. M. Spearrin, "Tomographic Laser Absorption Imaging of Combustion Species and Temperature in the Mid-wave Infrared," *Optics Express*, vol. 26, p. 20944, 8 2018.

[90] R. J. Tancin, Z. Chang, V. Radhakrishna, M. Gu, R. P. Lucht, and C. S. Goldenstein, "Ultrafast Laser Absorption Spectroscopy in the Mid-Infrared for Measuring Temperature and Species in Combustion Gases," in *AIAA Scitech 2020 Forum*, no. January, (Reston, Virginia), pp. 1–9, American Institute of Aeronautics and Astronautics, 1 2020.

[91] W. Ren, R. Mitchell Spearrin, D. F. Davidson, and R. K. Hanson, "Experimental and Modeling Study of the Thermal Decomposition of C3–C5 Ethyl Esters Behind Reflected Shock Waves," *The Journal of Physical Chemistry A*, vol. 118, pp. 1785–1798, 3 2014.

[92] T. Javed, E. F. Nasir, E. T. Es-Sebbar, and A. Farooq, "A comparative study of the oxidation characteristics of two gasoline fuels and an n-heptane/iso-octane surrogate mixture," *Fuel*, vol. 140, pp. 201–208, 2015.

[93] W. Ren, K. Y. Lam, D. F. Davidson, R. K. Hanson, and X. Yang, "Pyrolysis and oxidation of methyl acetate in a shock tube: A multi-species time-history study," *Proceedings of the Combustion Institute*, vol. 36, no. 1, pp. 255–264, 2017.

[94] J.-M. Hartmann, H. Tran, R. Armante, C. Boulet, A. Campargue, F. Forget, L. Gianfrani, I. Gordon, S. Guerlet, M. Gustafsson, J. T. Hodges, S. Kassi, D. Lisak, F. Thibault, and G. C. Toon, "Recent advances in collisional effects on spectra of molecular gases and their practical consequences," *Journal of Quantitative Spectroscopy and Radiative Transfer*, vol. 213, pp. 178–227, 7 2018.

[95] R. A. Brownsword, J. S. Salh, and I. W. M. Smith, "Collision broadening of CO2 transitions in the region of 4.3 μm. Effects of broadening gas (He, Ar and N2), rovibrational states and temperature," *J. Chem. Soc., Faraday Trans.*, vol. 91, no. 2, pp. 191–195, 1995.

[96] F. Rachet, M. Margottin-Maclou, A. Henry, and A. Valentin, "Q-Branch Line Mixing Effects in the (2000)I← 0110 and (1220)I← 0110 Bands of Carbon Dioxide Perturbed by N2, O2, and Ar and in the 1310 ← 0000 and 1310 ← 0110 Bands of Pure Nitrous Oxide," *Journal of Molecular Spectroscopy*, vol. 175, pp. 315–326, 2 1996.

[97] M. Wooldridge, R. Hanson, and C. Bowman, "Argon broadening of the R(48), R(50) and R(52) lines of CO2 in the (0001) ← (0000) band," *Journal of Quantitative Spectroscopy and Radiative Transfer*, vol. 57, pp. 425–434, 3 1997.

[98] F. Thibault, J. Boissoles, C. Boulet, L. Ozanne, J. P. Bouanich, C. F. Roche, and J. M. Hutson, "Energy corrected sudden calculations of linewidths and line shapes based on coupled states cross sections: The test case of CO2-argon," *Journal of Chemical Physics*, vol. 109, no. 15, pp. 6338–6345, 1998.

[99] B. Khalil, F. Thibault, and J. Boissoles, "Argon-broadened CO2 linewidths at high J values," *Chemical Physics Letters*, vol. 284, pp. 230–234, 2 1998.

[100] F. Thibault, B. Calil, J. Buldyreva, M. Chrysos, J. M. Hartmann, and J. P. Bouanich, "Experimental and theoretical CO2-Ar pressure-broadening cross sections and their temperature dependence," *Physical Chemistry Chemical Physics*, vol. 3, no. 18, pp. 3924–3933, 2001.

[101] C. R. Mulvihill and E. L. Petersen, "High-temperature argon broadening of CO2 near 2190 cm-1 in a shock tube," *Applied Physics B*, vol. 123, p. 255, 10 2017.

[102] C. Cousin, R. Le Doucen, C. Boulet, A. Henry, and D. Robert, "Line coupling in the temperature and frequency dependences of absorption in the microwindows of the 4.3 μm CO2 band," *Journal of Quantitative Spectroscopy and Radiative Transfer*, vol. 36, no. 6, pp. 521–538, 1986.

[103] M. Perrin and J. Hartmann, "Temperature-dependent measurements and modeling of absorption by CO2-N2 mixtures in the far line-wings of the 4.3 μm CO2 band," *Journal of Quantitative Spectroscopy and Radiative Transfer*, vol. 42, pp. 311–317, 10 1989.

[104] J. Boissoles, V. Menoux, R. Le Doucen, C. Boulet, and D. Robert, "Collisionally induced population transfer effect in infrared absorption spectra. II. The wing of the Ar-broadened $\nu 3$ band of CO2," *The Journal of Chemical Physics*, vol. 91, no. 4, pp. 2163–2171, 1989.

[105] L. Ozanne, Q. Ma, Nguyen-Van-Thanh, C. Brodbeck, J. Bouanich, J. Hartmann, C. Boulet, and R. Tipping, "Line-mixing, finite duration of collision, vibrational shift, and non-linear density effects in the $\nu 3$ and $3\nu 3$ bands of CO2 perturbed by Ar up to 1000 bar," *Journal of Quantitative Spectroscopy and Radiative Transfer*, vol. 58, pp. 261–277, 8 1997.

[106] H. Tran, C. Boulet, S. Stefani, M. Snels, and G. Piccioni, "Measurements and modelling of high pressure pure CO2 spectra from 750 to 8500 cm-1. I-central and wing regions of the allowed vibrational bands," *Journal of Quantitative Spectroscopy and Radiative Transfer*, vol. 112, no. 6, pp. 925–936, 2011.

[107] J. Lamouroux, L. Régalia, X. Thomas, J. Vander Auwera, R. R. Gamache, and J. M. Hartmann, "CO2 line-mixing database and software update and its tests in the 2.1 μm and 4.3 μm regions," *Journal of Quantitative Spectroscopy and Radiative Transfer*, vol. 151, pp. 88–96, 2015.

[108] C. Sagan, "The Planet Venus: Recent observations shed light on the atmosphere, surface, and possible biology of the nearest planet," *Science*, vol. 133, no. 3456, pp. 849–858, 1961.

[109] T. L. Hill, *An Introduction to Statistical Thermodynamics*. Addison-Wesley Publishing Co, 1960.

[110] M. Baranger, "Problem of Overlapping Lines in the Theory of Pressure Broadening," *Physical Review*, vol. 111, pp. 494–504, 7 1958.

[111] R. G. Gordon and R. P. McGinnis, "Line Shapes in Molecular Spectra," *The Journal of Chemical Physics*, vol. 49, pp. 2455–2456, 9 1968.

[112] A. Lévy, N. Lacome, and C. Chackerian, "Collisional Line Mixing," in *Spectroscopy of the Earth's Atmosphere and Interstellar Medium*, pp. 261–337, Elsevier, 1992.

[113] J. O. Hirschfelder, C. F. Curtiss, and R. B. Bird, *Molecular Theory of Gases and Liquids*. New York: John Wiley & Sons, Inc., 2nd ed., 1964.

[114] A. S. Pine and J. P. Looney, "Self-broadening and line mixing in HCN Q branches," *The Journal of Chemical Physics*, vol. 96, pp. 1704–1714, 2 1992.

[115] G. J. Rosasco, L. A. Rahn, W. S. Hurst, R. E. Palmer, and S. M. Dohne, "Measurement and prediction of Raman Q -branch line self-broadening coefficients for CO from 400 to 1500 K," *The Journal of Chemical Physics*, vol. 90, pp. 4059–4068, 4 1989.

[116] B. Lavorel, G. Millot, R. Saint-Loup, H. Berger, L. Bonamy, J. Bonamy, and D. Robert, "Study of collisional effects on band shapes of the ν 1 /2ν 2 Fermi dyad in CO 2 gas with stimulated Raman spectroscopy. II. Simultaneous line mixing and Dicke narrowing in the ν 1 band," *The Journal of Chemical Physics*, vol. 93, pp. 2185–2191, 8 1990.

[117] M. Margottin-Maclou, A. Henry, and A. Valentin, "Line mixing in the Q branches of the ν 1 +ν 2 band of nitrous oxide and of the (11 1 0) I ←(02 2 0) band of carbon dioxide," *The Journal of Chemical Physics*, vol. 96, pp. 1715–1723, 2 1992.

[118] J. I. Steinfeld, P. Ruttenberg, G. Millot, G. Fanjoux, and B. Lavorel, "Scaling

laws for inelastic collision processes in diatomic molecules," *The Journal of Physical Chemistry*, vol. 95, pp. 9638–9647, 11 1991.

[119] D. I. Pineda, F. A. Bendana, K. K. Schwarm, and R. M. Spearrin, "Multi-isotopologue laser absorption spectroscopy of carbon monoxide for high-temperature chemical kinetic studies of fuel mixtures," *Combustion and Flame*, vol. 207, pp. 379–390, 9 2019.

[120] M. F. Campbell, K. G. Owen, D. F. Davidson, and R. K. Hanson, "Dependence of Calculated Postshock Thermodynamic Variables on Vibrational Equilibrium and Input Uncertainty," *Journal of Thermophysics and Heat Transfer*, vol. 31, pp. 586–608, 7 2017.

[121] R. R. Gamache and J. Lamouroux, "The vibrational dependence of half-widths of CO2 transitions broadened by N2, O2, air, and CO2," *Journal of Quantitative Spectroscopy and Radiative Transfer*, vol. 117, pp. 93–103, 2013.

[122] R. R. Gamache, J. Lamouroux, V. Blot-Lafon, and E. Lopes, "An intercomparison of measured pressure-broadening, pressure shifting parameters of carbon dioxide and their temperature dependence," *Journal of Quantitative Spectroscopy and Radiative Transfer*, vol. 135, pp. 30–43, 2014.

[123] H. Li, Z. C. Owens, D. F. Davidson, and R. K. Hanson, "A simple reactive gasdynamic model for the computation of gas temperature and species concentrations behind reflected shock waves," *International Journal of Chemical Kinetics*, vol. 40, pp. 189–198, 4 2008.

[124] P. L. Varghese and R. K. Hanson, "Collisional narrowing effects on spectral line shapes measured at high resolution," *Applied Optics*, vol. 23, p. 2376, 7 1984.

[125] I. Gordon, L. Rothman, C. Hill, R. Kochanov, Y. Tan, P. Bernath, M. Birk, V. Boudon, A. Campargue, K. Chance, B. Drouin, J.-M. Flaud, R. Gamache,

J. Hodges, D. Jacquemart, V. Perevalov, A. Perrin, K. Shine, M.-A. Smith, J. Tennyson, G. Toon, H. Tran, V. Tyuterev, A. Barbe, A. Császár, V. Devi, T. Furtenbacher, J. Harrison, J.-M. Hartmann, A. Jolly, T. Johnson, T. Karman, I. Kleiner, A. Kyuberis, J. Loos, O. Lyulin, S. Massie, S. Mikhailenko, N. Moazzen-Ahmadi, H. Müller, O. Naumenko, A. Nikitin, O. Polyansky, M. Rey, M. Rotger, S. Sharpe, K. Sung, E. Starikova, S. Tashkun, J. V. Auwera, G. Wagner, J. Wilzewski, P. Wcisło, S. Yu, and E. Zak, "The HITRAN2016 molecular spectroscopic database," *Journal of Quantitative Spectroscopy and Radiative Transfer*, vol. 203, pp. 3–69, 12 2017.

[126] D. York, N. M. Evensen, M. L. Martinez, and J. De Basabe Delgado, "Unified equations for the slope, intercept, and standard errors of the best straight line," *American Journal of Physics*, vol. 72, pp. 367–375, 3 2004.